

**Crustal Structure of the  
Peruvian Continental Margin:  
Results from Wide-Angle Seismic Studies**

DISSERTATION  
ZUR ERLANGUNG DES DOKTORGRADES  
DER MATHEMATISCH-NATURWISSENSCHAFTLICHEN FAKULTÄT  
DER CHRISTIAN-ALBRECHTS-UNIVERSITÄT  
ZU KIEL

vorgelegt von

**Anne Krabbenhöft**

Kiel, 2004

Referent/in:

Korreferent/in:

Tag der mündlichen Prüfung:

Zum Druck genehmigt:

Prof. Dr. E. R. Flüh

Prof. Dr. W. Rabbel

29.11.2004

29.11.2004

Der Dekan

## Abstract

Active seismic investigations were carried out using ocean bottom hydrophones and seismometers along the Pacific margin off Peru. The structure and the P-wave velocities of the obliquely subducting oceanic Nazca plate and overriding South American plate were determined by modeling the wide-angle seismic data combined with the analysis of reflection seismic data from 8°S to 15°S. Combining these structural models with the earthquake distribution from a regional seismic network complements the deep crustal structure of the subducting Nazca plate from the trench to the Amazon Plain. Three detailed cross-sections of the subduction zone of the Peruvian margin and one strike-line across Lima Basin are presented here.

The oceanic crust of the Nazca plate, with a thin pelagic sediment cover, ranging from 0–200 m, has an average thickness of  $6.4 \pm 0.1$  km. At 8°S it thins to 4 km in the area of Trujillo Trough, a graben-like structure. Across the margin, the plate boundary can be traced to 25 km depth. The presence of a ~50-m-thick subduction channel with a P-wave velocity of 4.5 km/s is revealed by amplitude modeling. As inferred from the velocity models, a frontal prism exists adjacent to the trench axis and is associated with the steep lower slope. Terrigenous sediments are proposed to be transported downslope due to gravitational forces and compose the frontal prism, characterized by low seismic P-wave velocities. The lower slope material accretes against a backstop structure, which is defined by higher seismic P-wave velocities, 3.5–6.0 km/s. The large variations in surface slope along one transect may reflect basal removal of upper plate material, thus steepening the slope surface.

Subduction processes along the Peruvian margin are dominated by tectonic erosion indicated by the large margin taper, the shape and bending of the subducting slab, laterally varying slope angles and the material properties of the overriding continental plate. The erosional mechanisms, frontal and basal erosion, result in the steepening of the slope and consequent slope failure. Comparing the widths of the frontal prisms from the northern to the southern Peruvian margin, representing different stages after the Nazca Ridge passage, indicates, that the margin has returned to equilibrium after 11 Ma.

## Zusammenfassung

Seismische Untersuchungen wurden entlang des peruanischen Kontinentalrandes im östlichen Pazifik durchgeführt. Durch Modellierung der seismischen Weitwinkeldaten konnten die Struktur, sowie die P-Wellen Geschwindigkeiten des Untergrundes der subduzierenden ozeanischen Nazca Platte und der kontinentalen Süd-Amerikanischen Platte von 8°S bis 15°S verifiziert werden. Die Auswertung dieser Daten erfolgte in Kombination mit reflexionsseismischen Daten. Die Einbindung der so erhaltenen Untergrundmodelle in die Verteilung von Erdbeben aus dem peruanischen Erdbebenkatalog, liefert die Untergrundstruktur für den gesamten peruanischen Kontinentalrand von dem Tiefseeegraben, der die Platten abgrenzt, landeinwärts bis zu dem Amazonas Becken. Drei detaillierte Profile entlang der Subduktionszone des peru-anischen Kontinentalrandes und ein Querprofil über das Lima Becken werden in dieser Arbeit vorgestellt.

Die ozeanische Kruste der Nazca Platte ist mit einer dünnen pelagischen Sedimentschicht bedeckt, die von 0 bis 200 m variiert. Die ozeanische Kruste im Meßgebiet hat durchschnittlich eine Mächtigkeit von 6.4 km, die im Bereich des Trujillo Trops bei 8°S, einer Grabenstruktur, auf 4 km ausdünn. Der Tiefseeegraben vor Peru liegt in einer Tiefe von ca. 6 km und die Plattengrenze kann anhand der Daten, bis in eine Tiefe von 25 km beobachtet werden. Ein Subduktionskanal von 50 m Mächtigkeit, und der P-Wellen Geschwindigkeit von 4.5 km/s, wird mit der Methode der Wellenfeld-Modellierung nachgewiesen. Die Geschwindigkeits-Modelle zeigen, daß sich ein Akkretionskeil direkt landeinwärts vom Tiefseeegraben ausgebildet hat, welcher mit dem steilen unteren Kontinentalhang in Verbindung gebracht wird. Es wird angenommen, daß terrigene Sedimente dort abgelagert werden, welche durch niedrige P-Wellen Geschwindigkeiten charakterisiert sind. Die Sedimente des unteren Kontinentalhanges lagern an eine landeinwärts liegende Backstop Struktur, die aus kontinentalem Basement aufgebaut ist, und mit seismischen P-Wellen Geschwindigkeiten von 3.5 bis 6.0 km/s charakterisiert ist. Die stark variierende Meeresbodentopographie entlang des Kontinentalhanges deutet darauf hin, daß Material an der Unterkante der kontinentalen Platte entfernt wird. Dieser Prozess führt zu steilen Neigungswinkeln des Kontinentalhanges.

Die Subduktionsprozesse vor Peru werden von tektonischer Erosion dominiert. Anzeichen dafür sind der große Winkel zwischen Kontinentalhang und subduzierender Platte (Taper), die Struktur und Neigung der subduzierenden Platte, lateral variierende Neigungswinkel entlang des Kontinentalhanges und die Materialeigenschaften der kontinentalen Platte. Die Erosionsmechanismen haben größere Neigungen des Kontinentalhanges zur Folge, was wiederum zu Hangrutschungen führt und zum Aufbau des frontalen Sediment-Keils. Vergleicht man diese Akkretionskeile vor Peru, die von Norden nach Süden verschiedene Alterstufen nach der Nazca-Rücken-Subduktion, mit erhöhten Erosionsraten, darstellen, so stellt sich nach 11 Ma der Gleichgewichtszustand des Peruanischen Kontinentalrandes, mit den für ihn typischen erosiven Subduktionsprozessen, wieder ein.

---

# Contents

<b>1</b>	<b>Introduction</b>	<b>1</b>
1.1	Geologic setting . . . . .	3
1.1.1	Origin of the oceanic Nazca plate . . . . .	3
1.1.2	The aseismic Nazca Ridge . . . . .	3
1.2	Previous investigations and the GEOPECO project . . . . .	5
1.2.1	The migration history of the Nazca Ridge . . . . .	7
1.3	Subduction zones . . . . .	9
1.3.1	Accretionary subduction zones . . . . .	10
1.3.2	Erosive subduction zones . . . . .	10
<b>2</b>	<b>Seismic data</b>	<b>13</b>
2.1	Wide-angle data . . . . .	13
2.1.1	Processing procedure . . . . .	13
2.2	Reflection data . . . . .	16
2.3	Results from reflection data . . . . .	16
<b>3</b>	<b>Determination of seismic velocity models</b>	<b>21</b>
3.1	Forward modeling . . . . .	23
3.2	Tomographic inversion . . . . .	30
3.2.1	Sensitivity of the FAST algorithm . . . . .	33
<b>4</b>	<b>Results and discussion of the refraction data</b>	<b>35</b>
4.1	The oceanic plate . . . . .	35
4.1.1	General seismic velocity-depth distributions . . . . .	36
4.1.2	The crustal structure of the oceanic Nazca plate . . . . .	37
4.2	The trench across the Peruvian margin . . . . .	45
4.2.1	The critical taper - the Coulomb theory - a stable wedge . . . . .	45
4.2.2	The critical taper applied to the toe of the Peruvian margin . . . . .	50
4.3	The continental slope and shelf structure . . . . .	53
4.3.1	The lower slope . . . . .	53
4.3.2	The backstop region . . . . .	58
4.3.3	The forearc region . . . . .	60

<b>5</b>	<b>Amplitude modeling</b>	<b>67</b>
5.1	Is there evidence for a subduction channel? . . . . .	70
5.1.1	Thickness of the subduction channel . . . . .	71
<b>6</b>	<b>Seismicity in subduction zones</b>	<b>79</b>
6.1	Earthquake distribution across the Peruvian continental margin from a regional network . . . . .	80
<b>7</b>	<b>Conclusions and Outlook</b>	<b>87</b>
<b>A</b>	<b>The Coulomb Theory</b>	<b>101</b>
<b>B</b>	<b>The Reflectivity Method</b>	<b>103</b>

## Introduction

Convergent continental margins are destructive plate boundaries where oceanic plates are subducted beneath overriding continental plates. Subduction zone processes are closely linked to natural hazards, such as the generation of earthquakes and volcanic activity along plate margins. There has been great interest in convergent margin settings for their potential (and demonstrated capability) of producing important oil, gas, and hydrocarbons reservoirs and ore deposits [*Bebout et al., 1996*]. Thus, the analysis of dynamic processes along continental margins contributes to a better understanding for locating resources and places of increased danger from natural disasters.

The dynamics of convergent margins are mirrored by complex deformation patterns and material transfer modes. Sediments arriving at the trench on the oceanic plate may be frontally accreted, basally underplated or subducted. Continental material might be removed from the lower part of the upper plate, which is called subduction erosion, and transported into the upper mantle together with the oceanic subducting plate. Depending on these different subduction processes, convergent margins are classified as accretive and erosive margins [*von Huene and Scholl, 1991*].

The Peruvian continental margin (Fig. 1.1) is subject of this thesis. The research area is an 'active' margin and features all the characteristics associated with that tectonic setting: trench topography, large earthquakes [*Savage, 1983*], the Andean volcanic arc [<http://www.volcano.si.edu/world/summinfo.cfm>], gas hydrates [*Pecher et al., 2001*] across the continental slope and the interaction of the subducting Nazca Ridge with the South American continental margin. These features make the Peruvian margin a distinguished target for geophysical investigations, resulting in the main objectives for this study:

- Velocity-depth models are obtained from seismic refraction data along three profiles across the Peruvian forearc. The structures in the velocity-depth models, combined with reflection seismic data, are then related to geological structures.
- The critical taper is applied to the Peruvian margin to gain insight on the stability of the margin and the related subduction processes at different periods after the Nazca Ridge subduction (from north to south).
- Amplitude modeling suggests a low-velocity subduction channel and allows the verification of the subduction-channel thickness.
- The velocity-depth models of the Peruvian forearc are correlated with the deeper structure of the earthquake distribution from the regional Peruvian network.

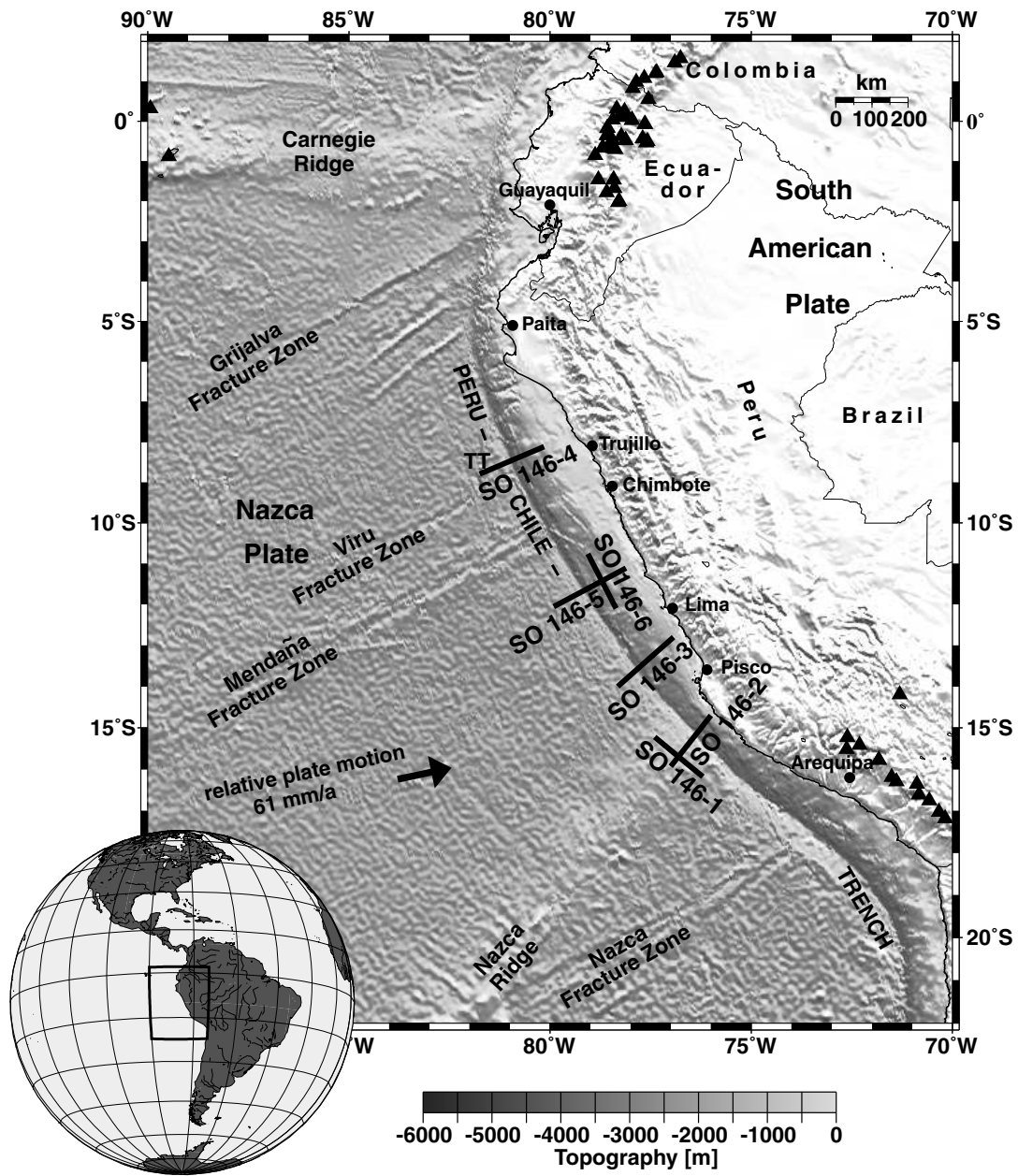


Figure 1.1: Geodynamic setting of the Peruvian continental margin. Bathymetry is from *Sandwell and Smith [1997]*, illumination is from northeast. *Norabuena et al. [1999]* determined the plate motion vector. The active volcanic arc is marked by triangles (Smithsonian Institution catalogue, available at <http://www.volcano.si.edu/world/summinfo.cfm>).



## 1.1 Geologic setting

### 1.1.1 Origin of the oceanic Nazca plate

The oceanic Nazca plate originates from the fast spreading East Pacific Rise (EPR), whose full spreading rate is 150 mm/yr [Purdy *et al.*, 1992]. The plate is moving largely eastwards (N78°E) with a velocity of about 61 mm/y, resulting in convergence oblique to the trench as it bends to the southeast [Norabuena *et al.*, 1999]. The Peru-Chile trench, with water depths of more than 6000 m, is the collision zone of the Nazca plate with the continental South American plate (Fig. 1.1). The Nazca plate is one segment of the former Farallon plate, which was divided into the Nazca and the Cocos plate [Hey *et al.*, 1995] by the Cocos-Nazca spreading center (Fig. 1.2). The Cocos-Nazca spreading center is located north of the Galapagos Hotspot and Carnegie Ridge. The fragmentation of the Farallon plate started ~23 Ma ago at an already existing fracture zone, the Marquesas Fracture Zone [Lonsdale and Klitgord, 1978; Hey *et al.*, 1995; Barckhausen *et al.*, 2001]. It started at the Peru-Chile trench and propagated westward at a rate of 7.1 cm/yr resulting in the Cocos-Nazca spreading center [Hey *et al.*, 1995]. This process coincided with a great change in the spreading velocity in the Atlantic ocean and an elevation of the Andes.

The Nazca plate is segmented by fracture zones leading to different crustal ages along the plate boundary. The Mendaña Fracture Zone trends N65°E and marks a transition zone of crustal age difference of about 10 my, as revealed by magnetic anomalies [Hussong *et al.*, 1984]. Consequently, at the trench, the Nazca plate is about 38 Ma old off central and south Peru and about 28 Ma old north of the Mendaña Fracture Zone [Müller *et al.*, 1997]. The increasing age of the oceanic crust of the southern segment coincides with the increasing water depth from 4500 m in the north to 5000 m south of Mendaña Fracture Zone [Hilde and Warsi, 1982]. The Viru Fracture Zone parallels the Mendaña Fracture Zone 110 km further north and joins the Trujillo Trough, a reverse fault, with a N15°E trend, connecting Viru Fracture Zone with the Peru-Chile trench [Huchon and Bourgois, 1990] (Fig. 1.1). The oceanic plate east of the Trujillo Trough is characterized by a rough fabric trending perpendicular to the Mendaña Fracture Zone [Huchon and Bourgois, 1990].

### 1.1.2 The aseismic Nazca Ridge

The study area is bounded by two aseismic bathymetric highs (Figs. 1.1, 1.2). Carnegie Ridge in the north originates from the Galapagos Hotspot [Collot *et al.*, 2002]. Nazca Ridge in the south, was formed at a melting anomaly in the Pacific-Farallon/Nazca spreading center, which is now the East Pacific Rise, simultaneously with the aseismic Tuamotu Ridge (Fig. 1.2), its mirror image on the Pacific plate to the west [Pilger and Handschumacher, 1981; Ito *et al.*, 1995]. Four forearc basins (extension is indicated by normal faulting [von Huene *et al.*, 1996]) are located in the study area from north to south: Trujillo and Yaquina Basin at 9°S, Lima Basin at 11°S and West Pisco Basin

1.1. GEOLOGIC SETTING

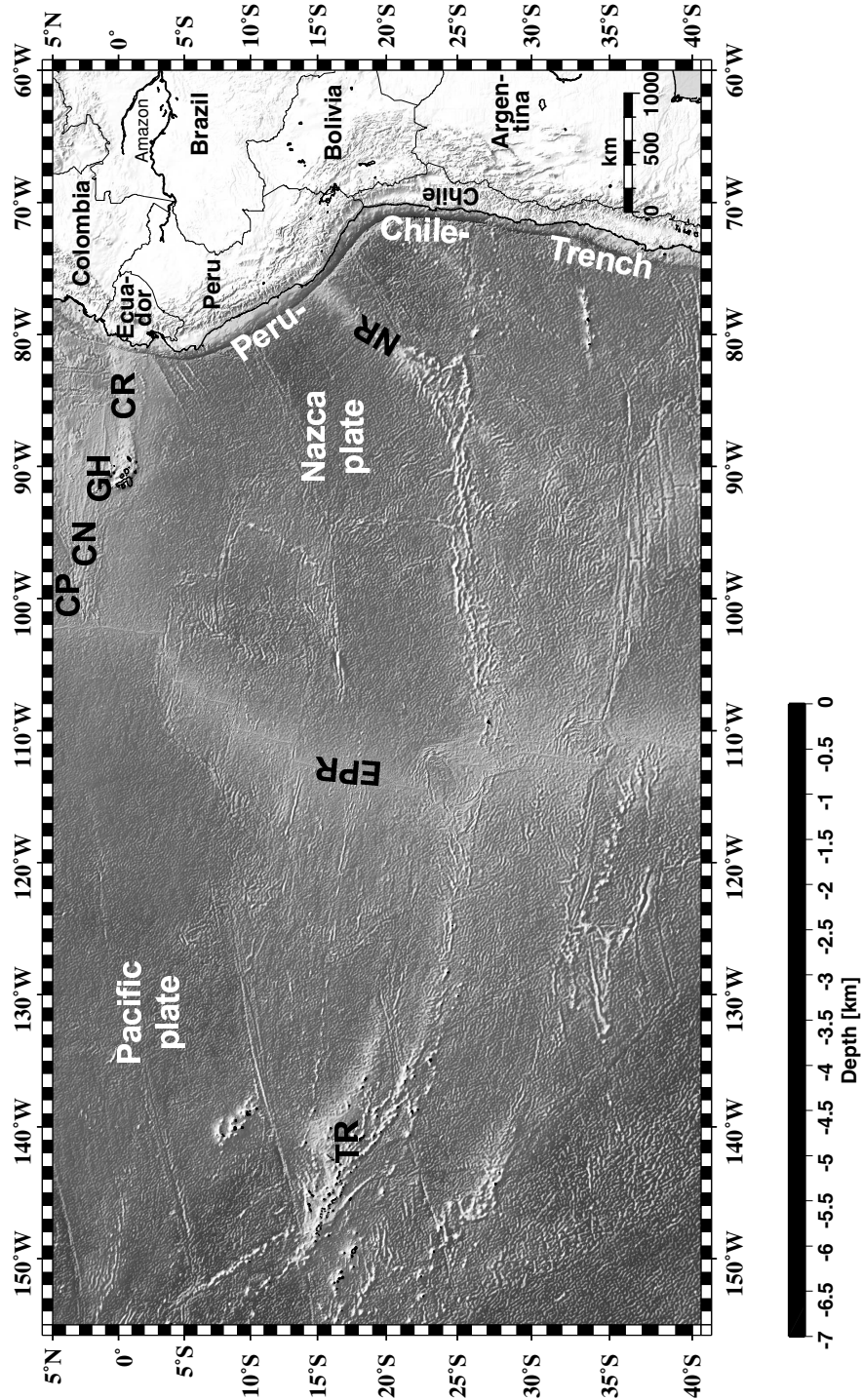


Figure 1.2: Geodynamic setting of the southern East Pacific region with bathymetry data from *Sandwell and Smith [1997]*, illumination is from northeast. CN: Cocos-Nazca spreading center; CR: Carnegie Ridge; CP: Cocos plate; EPR: East Pacific Rise; GH: Galapagos Hotspot; NR: Nazca Ridge; TR: Tuamoto Ridge.

at 13°S (Fig. 1.4). The Lima and West Pisco basins were affected by the southward migration of the Nazca Ridge, which caused uplift and subsidence along the margin leading to increased rates of erosion [von Huene and Suess, 1988; Pecher et al., 1996; Clift et al., 2003]. The coastline of Peru is also affected by the Nazca Ridge, forming a seaward bulge where it is currently subducting. An eastward migration of the continental margin north of Peru since the Mesozoic is linked to subduction erosion [von Huene and Scholl, 1991]. An eastward shift from the position of the Mesozoic magmatic arc to the late Cenozoic arc is also documented for Peru [McKee and Noble, 1990].

More than 25 years ago, Barazangi and Isacks [1976] concluded from teleseismic earthquake hypocenters, that the South American continental margin of Peru is characterized by flat subduction. The subducting angle of the oceanic plate is about 30° down to a depth of 100 km. Then the oceanic plate subducts largely horizontal for some 100 km [Hasegawa and Sacks, 1981], before the subduction angle increases again and the plate descends steeply down to the 670 km discontinuity and beyond. The segment between 5°S and 15°S is the largest area worldwide, where flat subduction occurs [Norabuena et al., 1994]. The flat subduction and uplift of the continental upper plate is associated with the buoyancy of the thickened oceanic crust of the Nazca Ridge [Vogt et al., 1976; Pilger, 1981; Norabuena et al., 1994]. Flat subduction is coincident with the lack of Quaternary volcanism as observed as well at other places where ridge subduction occurs, e.g., Cocos Ridge underneath Costa Rica and Juan Fernandez Seamount Chain underneath Chile [Steinmann, 1929; Nur and Ben-Avraham, 1981; Pilger, 1981; Protti et al., 1995; Gutscher et al., 2000].

## 1.2 Previous investigations and the GEOPECO project

In the late 1970's extensive geological and geophysical studies were carried out along the continental margin of Peru within the Nazca Plate Project [Kulm et al., 1981]. In 1988 ten sites on the Peruvian margin were drilled during ODP Leg 112 (Fig. 1.3) and correlated with high quality seismic multichannel (MCS) data, acquired in 1972 at 12°S by the Shell Oil Co. (the Hague) (CDP-1, CDP-2, 1017 and 1018 lines, Fig. 1.3) [von Huene and Suess, 1988]. These lines were later depth migrated and used along with MCS data acquired by the Hawaii Institute of Geophysics (HIG lines, Fig. 1.3) [Moore and Taylor, 1988] to re-evaluate the tectonic processes across the Peru margin [von Huene et al., 1996]. These studies only partly cover the Peruvian margin, mainly the northern area, where the uplift and subsidence history, due to the passing Nazca Ridge, was investigated, as well as the resulting tectonic processes and the material transfer modes, e.g., the erosional effects of Nazca Ridge subduction.

Within the scope of the GEOPECO project (GEOPECO is the acronym for GEOphysical experiments at the PERuvian CONTinental margin), seismic reflection and refraction data (lines SO146-1 to SO146-6, Figs. 1.1–1.4) were acquired during R/V *Sonne* cruise SO146 offshore Peru in 2000 [Bialas and Kukowski, 2000]. The seismic data were supplemented by high resolution bathymetry and gravity data.

## 1.2. PREVIOUS INVESTIGATIONS AND THE GEOPECO PROJECT

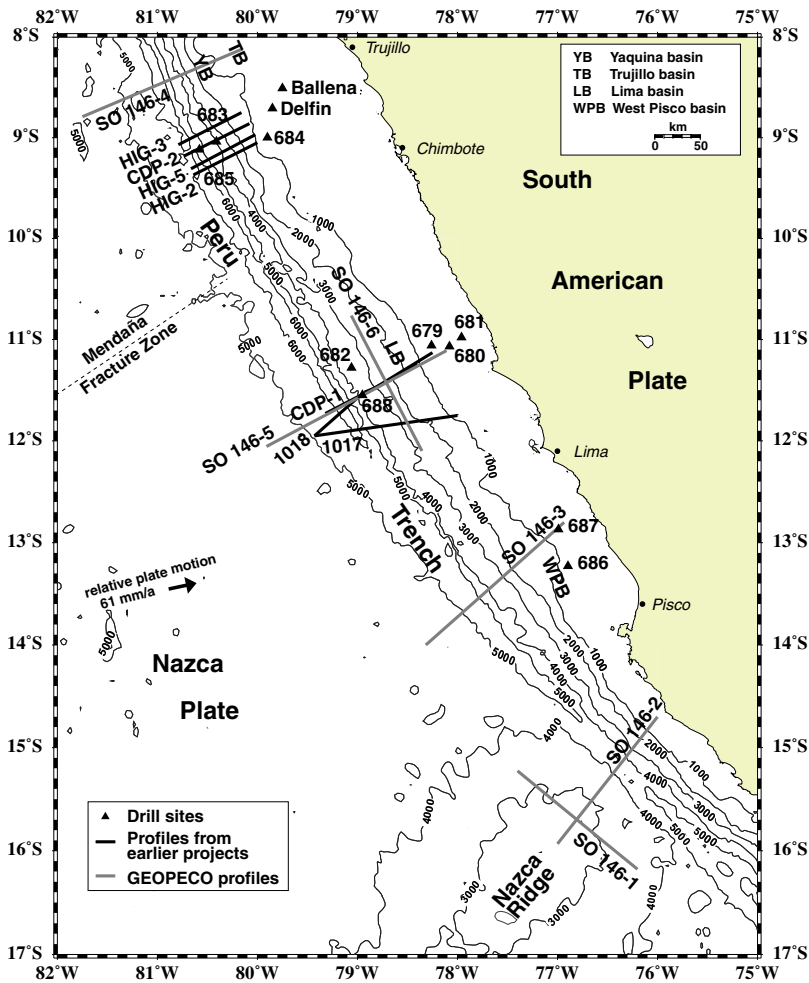


Figure 1.3: Locations of the seismic lines and drill sites across the Peruvian continental margin. Bathymetry is taken from *Sandwell and Smith [1997]*. *Norabuena et al. [1999]* determined the plate motion vector. The important geologic features in the research area, e.g., the Peru trench and Nazca Ridge, are annotated.

Heat flow measurements were conducted along with sea floor sampling and ocean floor video observations [*Pecher et al., 2001*]. A quantitative characterization of the structures and geodynamics of the Peruvian section of the Andean subduction zone and the associated gas hydrate systems in regions with variable tectonic histories were the main objectives of this cruise. Integrating the geologic-geophysical information mentioned above, this study concentrates on the analysis of four wide-angle seismic profiles acquired across and along the margin during the GEOPECO cruise. The aim is to obtain the deep crustal structure and determine the tectonic processes from the velocity models along the entire Peruvian margin. Integrating earlier acquired high resolution MCS data of line CDP-1 [*von Huene and Suess, 1988*], improves the resolution of the first kilometers of the refraction-velocity-depth models, and therefore, the resolution of the entire crustal structure at 12°S.

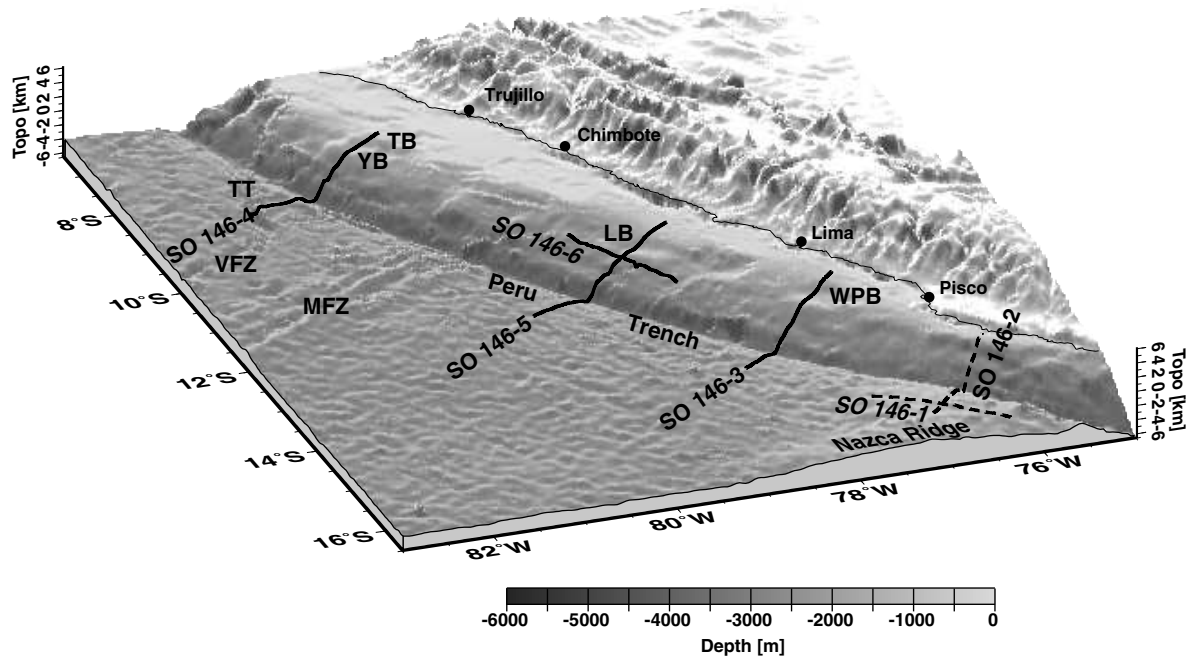


Figure 1.4: A detailed overview of the GEOPECO study area with bathymetry data from *Sandwell and Smith [1997]*, illumination is from northeast. The solid lines are the positions of the GEOPECO wide-angle seismic profiles discussed in this study, whereas the dashed lines are the positions of the GEOPECO wide-angle seismic profiles presented by *Hampel et al. [2004]*. Profile SO146-4 covers Trujillo Trough (TT) at its seawardmost part. LB: Lima Basin; MFZ: Mendaña Fracture Zone; TB: Trujillo Basin; VFZ: Viru Fracture Zone; WPB: West Pisco Basin; YB: Yaquina Basin.

### 1.2.1 The migration history of the Nazca Ridge

Oblique subduction of the Nazca plate and the resulting southward migration of the Nazca Ridge along the margin characterize the region investigated during cruise SO146 (Fig. 1.1). It was believed, that the entire Peruvian margin, starting at 5°S to the present collision zone at 15°S, was affected by Nazca Ridge subduction [*von Huene et al., 1996*]. A re-evaluation of the migration history of the Nazca Ridge, yields the northernmost collision zone of Nazca Ridge with the South American plate at 11°S [*Hampel, 2002*] (Fig. 1.5). The reconstruction of the paleo-positions of the Nazca Ridge relative to a fixed South American plate was conducted by using updated plate motion data, assuming a linear continuation of the ridge, as suggested by the shape of the present ridge (dark grey, Fig. 1.5), and a paleo-trench position similar to the present trench line [*Hampel, 2002*]. The three differing displacement vectors for different time periods, ranging from 123 mm/a to 75 mm/a, are annotated in Figure 1.5.

## 1.2. PREVIOUS INVESTIGATIONS AND THE GEOPECO PROJECT

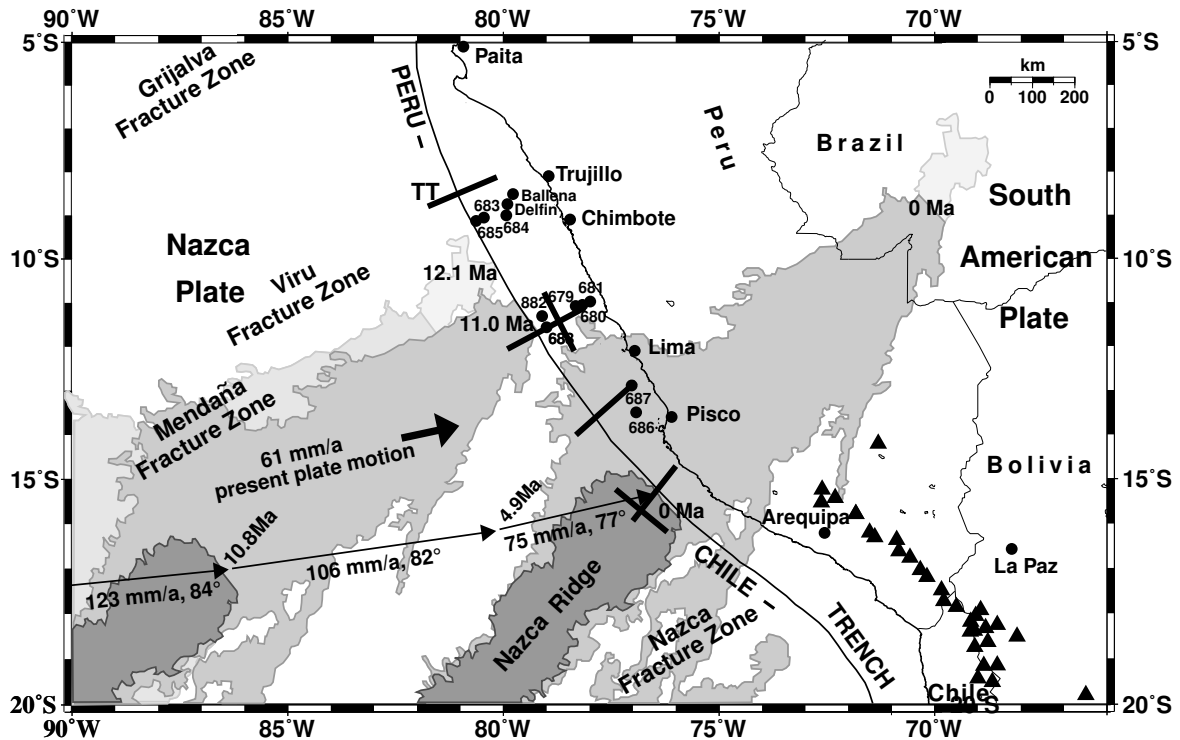


Figure 1.5: The southward migration of the Nazca Ridge along the Peruvian margin, modified after [Hampel \[2002\]](#). The present ridge position (4000 m depth isolines) is dark grey at 0 Ma, 15°S. The subducted ridge continues 900 km landwards (lighter grey at 0 Ma), reconstructed after the 4000 m depth contour of the Tuamotu Ridge. The outermost tip is light grey. The onset of the Nazca Ridge subduction occurred at 11.0 Ma ago at 11°S, if accounting for the outermost tip of the subducted ridge, 12.1 Ma ago at 10°S. The plate motion vectors used for the reconstruction of the Nazca Ridge position are annotated arrows. The solid lines are the positions of the GEOPECO wide-angle seismic profiles. Drill sites are annotated circles. Positions of the important geologic features are annotated. TT: Trujillo Trough.

The subducted portion of the Nazca Ridge (lighter grey, Fig. 1.5), with a length of 900 km, was obtained by comparison with the shape of the Tuamotu Ridge, its conjugate feature on the Pacific plate. The northwesternmost tip of the Tuamotu Ridge probably has formed on 10-20 Ma old oceanic crust on the Pacific plate, and not at the spreading center [[Cande et al., 1989](#)]. Therefore, it probably does not have a counterpart, the outermost tip (light grey, Fig. 1.5) of the subducted portion of the Nazca Ridge. The plate reconstruction, accounting for the outermost tip of the subducted Nazca Ridge, yields the onset of the ridge subduction at 10°S, 12.1 Ma ago [[Hampel, 2002](#)]. Not accounting for the outermost tip of the subducted Nazca Ridge for the reason mentioned above, the onset of the Nazca Ridge subduction at 11°S, 11 Ma ago [[Hampel, 2002](#)] is preferred in this study (Fig. 1.5). These reconstruction scenarios are consistent with

the drilling information across the Peruvian margin, continuous shale deposition at 9°S (indicating no uplift and subsidence) and sedimentary and benthic foraminiferal stratigraphy at 11°S (indicating uplift and subsidence since the Miocene) [*von Huene and Suess, 1988*].

Thus, three of the seismic profiles, SO146-5, SO146-6, both at 12°S, and SO146-3 at 14°S (Fig. 1.5), cover the area where the subducting Nazca Ridge has passed during the last 11 my [*Hampel, 2002*], which permit to study the subduction processes at different stages after Nazca Ridge subduction. They represent 'time slices' of the margin after the ridge subduction and thus allow the process of 'returning to equilibrium' in the wake of the ridge crest subduction to be reconstructed [*von Huene et al., 1996*]. The northernmost profile (SO146-4/9°S) characterizes portions of the Peruvian margin, which have not been affected by ridge subduction [*Hampel, 2002*]. Therefore, this part of the Peruvian margin is defined in this study as representing the 'state of equilibrium' concerning subduction mechanisms. Thus, profile SO146-4/9°S serves as reference to compare with the lines affected by Nazca Ridge subduction (the refraction profiles SO146-6/12°S, and SO146-3/14°S).

### 1.3 Subduction zones

A section across a subduction zone typically shows an incoming plate, the trench, an accretionary/frontal prism, the forearc with a forearc basin and the volcanic arc on the overriding plate. The incoming plate, oceanic lithosphere, is usually modified by subduction, while tectonic and geochemical evidence indicates that active margins are likely the principal source of the continental crust [e.g., *Dewey and Windley, 1981; Taylor and McLennan, 1985; Rudnick and Fountain, 1995; Barth et al., 2000*]. Subduction zones are classified into erosive and accretive convergent margins, depending on the mass flux [*Clift and Vannucchi, 2004*]. *von Huene and Scholl [1991]* classified convergent margins as type 1 and type 2 margins. They define type 1 convergent margins, where accretionary prisms form, therefore being an accretionary convergent margin. At type 2 margins little net accretion takes place, and effectively, all sediment is subducted beneath the basement forming the landward trench slope. Later they subdivided the type 1 convergent margins into margins with small accretionary prisms (5–40 km wide, which is also widely known as intermediate accretionary wedges [e.g., *Lallemand et al., 1994*]) and accretionary wedges with large frontal prisms (>40 km wide, which are the typical accretionary wedges) [*von Huene and Scholl, 1993*]. In this study, the terms of convergent margins classifications (erosive/accretionary) are defined by net mass wasting/production across the entire margin, including the volcanic arc) following the classification of *Clift and Vannucchi [2004]*, are preferred. If the volume of the continental crust is to be maintained, the average magmatic productivity of arcs must exceed 90 km<sup>3</sup>/my [*Clift and Vannucchi, 2004*]. Figure 1.6 illustrates the characteristics of both, accretionary and erosive, convergent margin types with a schematic diagram.

#### 1.3.1 Accretionary subduction zones

Accretion is favored in regions of slow convergence ( $\leq 7.6$  cm/yr) and where the trench sediment thickness is  $>1$  km [Clift and Vannucchi, 2004]. Most of the incoming sediment is frontally accreted at the toe of the continental slope [von Huene and Scholl, 1991], building landward dipping thrusts [Wang and Davis, 1996]. Accretion may also occur through underplating, leading to the growth of the overriding plate. At the same time small amounts of sediment may return into the upper mantle via sediment subduction, however, sediment accretion dominates at accretive subduction zones. The thickness of the trench sequence is dominated by the sediment supply [Helwig and Hall, 1974]. The accretion of sediment results in gently dipping trench slopes and consequently small margin tapers. These sediment masses accrete against a backstop structure, which is strengthened sediment, typically consisting of lithified, dewatered remains of an older ('ancient') accretionary prism [von Huene and Scholl, 1991]. The forearc basins are characterized by large amounts of horizontally layered undisturbed sediments. Accretionary subduction systems are areas of net crustal growth. Examples of accretionary convergent margins are the Cascadia, Makran, Barbados, Java, and Sumatra region [e.g., Hyndman et al., 1990; Kopp et al., 2000; Brown and Westbrook, 1988; Kopp and Kukowski, 2001; Schlüter et al., 2002; Moore and Taylor, 1982].

#### 1.3.2 Erosive subduction zones

In contrast to accretion, tectonic erosion is favored in regions where the convergence rates exceed  $6 \pm 0.1$  cm/yr and where the trench sedimentary cover is  $<1$  km [Clift and Vannucchi, 2004]. Sedimentary rocks are typically limited to the forearc basin, where they may be faulted but are not strongly sheared in the fashion of an accretionary wedge (Fig. 1.6a). The sediments in the forearc basin are underlain by continental or volcanic arc basement, which extends seaward to the lower slope [Wang and Davis, 1996]. The sedimentary wedge (frontal prism) accretes against the backstop structure, which is the seawardmost part of the basement. A rough incoming plate and strong coupling between the overriding and subducting plates result in rapid tectonic erosion [Lallemand, 1995, 1998]. Thus a landward retreat of the trench is observed [e.g., von Huene and Lallemand, 1990; Vannucchi et al., 2001]. Frontal tectonic erosion is known to steepen the trench slopes, therefore leading to a large margin taper [e.g., Dupont and Herzer, 1985; von Huene and Lallemand, 1990]. The small amounts of trench sediment are mostly returned into the upper mantle forming a 'subduction channel' with the eroded upper plate material. At some erosive convergent margins long-term erosion is superimposed by periods of strong tectonic erosion caused by specific subduction events, such as subducting seamounts or aseismic ridges. von Huene and Lallemand [1990] calculated long-term erosion rates of 2.5–3.5 km/my trench retreat since 20 Ma for the Peruvian margin.



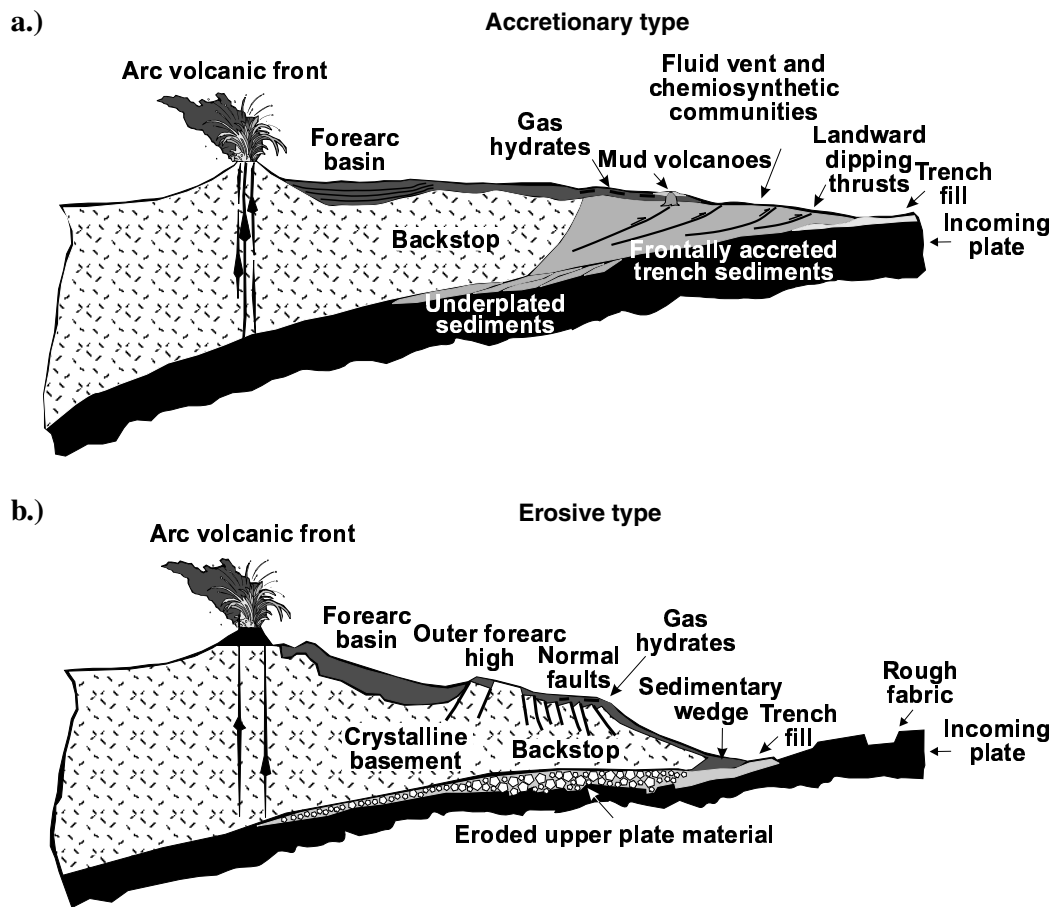


Figure 1.6: Schematic cartoon showing the characteristics of an (a) accretionary and (b) erosive convergent margin, modified after [Cift and Vannucchi, 2004]. See text for details.

Since 11 Ma Nazca Ridge accelerates the erosion rates, from 3.1 km/my trench retreat since the Eocene (47 Ma) in Lima Basin at 12°S at the Peruvian margin, which is consistent with the values determined by *von Huene and Lallemand* [1990], to 10 km/my trench retreat short-term rates [Cift et al., 2003]. Ridge collision is leading to vertical tectonics and appears to dominate the erosive history in many other examples (e.g. Tonga, southern Chile, Mindanao, and Costa Rica [Dupont and Herzer, 1985; Cande and Leslie, 1986; Ballance et al., 1989; Pubellier et al., 1999; Behrmann and Kopf, 2001; Laurson et al., 2002; Vannucchi et al., 2003]). Other processes leading to subsidence of erosional convergent margins are basal tectonic erosion of the forearc crust, which is driven by high fluid pressure in some regions, such as northern Chile [von Huene and Ranero, 2003]. An unstable steep tapered wedge may result in gravitational collapse and consequently extension of the forearc [Platt, 1986]. Basal tectonic erosion of the

### 1.3. SUBDUCTION ZONES

---

forearc crust and not horizontal extension is the cause for crustal extension implied by subsidence, if only slight normal faulting occurs in the forearc acoustic basement [*Ranero and von Huene, 2000; Vannucchi et al., 2001*]. Erosive subduction zones are sinks of continental crust. Most of the characteristics of erosive continental margins are found at the Peruvian convergent margin. These typical features will be discussed in the following sections on the basis of the GEOPECO seismic refraction dataset.

# 2

---

## Seismic data

### 2.1 Wide-angle data

Seismic measurements off Peru were carried out using the R/V *Sonne* during cruise SO146 [Bialas and Kukowski, 2000]. Six wide-angle seismic profiles were shot with an array of three 32 l airguns at a shot interval of 60 s and a ship speed of 4 kn, resulting in an average shot spacing of 120 m. Data were recorded by a total of 97 stations using GEOMAR ocean bottom hydrophones (OBH) [Flueh and Bialas, 1996] and seismometers (OBS) [Bialas and Flueh, 1999] (see Figures 1.1–1.4 for locations of the refraction profiles).

#### 2.1.1 Processing procedure

A raw/unprocessed SEG-Y section of the hydrophone channel of OBS station 61 is shown in Figure 2.1a. The data are dominated by a low frequency content and the bubble pulse of the airgun is very strong, which inhibits the unambiguous identification of reflections and refractions. The seismic signal holds frequencies from about 4 to 16 Hz for the different phases. Therefore a time and offset dependent frequency filter was applied to adjust for the time and offset dependent variations. To further improve the temporal resolution of the seismic data, a gated Wiener deconvolution was applied to compress the basic seismic wavelet. Additionally, the refraction seismic data were corrected with relocated OBH/S positions. The processed and relocated data of the hydrophone channel of OBS station 61 are shown in Figure 2.1b. Data quality is very good and the source energy was sufficient to receive signals from a distance of at least 130 km from the OBH/S stations penetrating to a depth of 30 km. Station OBH 43 of profile SO146-4/9°S (Fig. 2.2) is a representative example of the seismic sections.

## 2.1. WIDE-ANGLE DATA

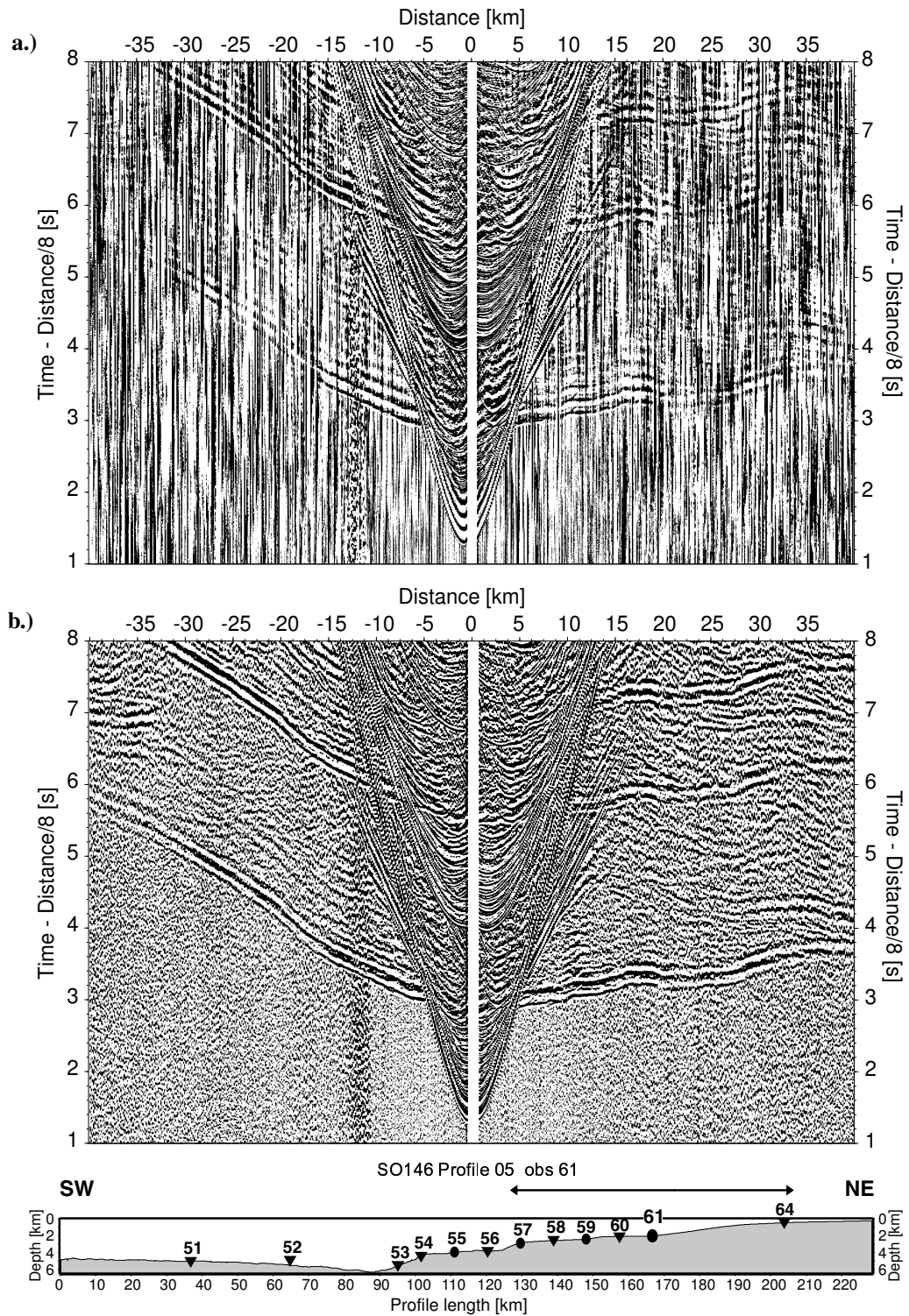


Figure 2.1: *The near offset traces of the hydrophone section of OBS station 61 along refraction profile SO146-5/12° S, displayed with a reduction velocity of 8 km/s. Comparison of raw SGY-data (a) and processed and relocated section (b), (see text for details). Topography and positions of OBH/S stations are plotted below.*

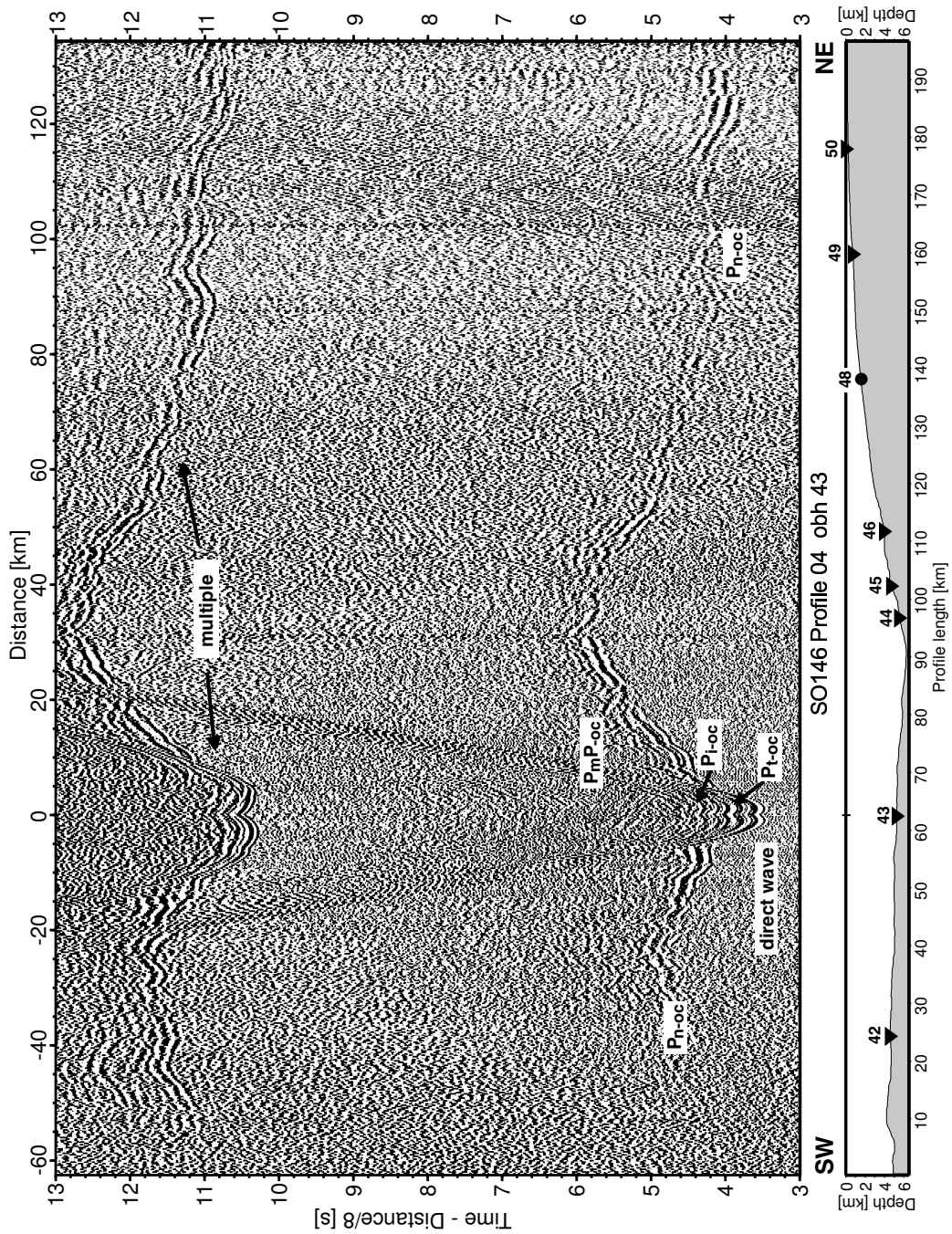


Figure 2.2: Representative example of a wide-angle seismic section recorded by OBH 43 located on the oceanic crust on the northernmost profile SO146-4/9°S. The data are displayed with a reduction velocity of 8 km/s.  $P_{t-oc}$  and  $P_{i-oc}$  denominate the reflections from the top of the oceanic crust and from an intracrustal boundary, respectively. The mantle refraction  $P_n$  shows a good signal as far as 130 km offset from the OBH position.  $P_mP$  denotes the reflected wave from the crust-mantle boundary. The topography along the profile is shown underneath the seismic section with all the locations of the OBH/S stations, triangles/circles mark OBH/OBS stations.

## 2.2 Reflection data

Multichannel seismic (MCS) data were acquired simultaneously to the refraction profiles (Figs. 2.3 and 3.1). A 24 channel streamer recorded the seismic signal along an active length of 120 m and was towed about 50 m behind the ship's stern [*Bialas and Kukowski, 2000*]. The data were sorted for common midpoints and a frequency-filter was applied before stacking. Due to the low frequency content of the seismic signal and the great water depth across the lower slope the Fresnel zone is large. Spatial aliasing occurs at steep topographic features as a consequence of the large shot point distance of 150 m. Hence, structures beneath the steep lower slope, such as the frontal prism, cannot be resolved. However, even with this low resolution MCS data, some distinct characteristics of the Peruvian margin can be identified. The subducting oceanic plate with a thin pelagic sediment layer can be resolved landwards from the trench axis underneath the lower continental slope (Fig. 2.3a). A prominent bottom simulating reflector (BSR) is present underneath the lower slope, which is further investigated in a different study by *Pecher et al. [2001]*. The landward part of the seismic section reveals erosional tectonic features, most distinct in the area between OBS station 60 and OBH station 61 (Fig. 2.3b). Normal faults are identified across the upper continental slope, despite the low resolution.

Additional MCS data from line CDP-1 published by *von Huene and Suess [1988]* (Fig. 2.4), which is coincident with the GEOPECO line SO146-5/12°S (Fig. 2.3), reveals more details across the forearc: The higher lateral resolution of this time migrated MCS line enables the identification of structures beneath the steep lower slope. Forward verging thrusts occupy the seaward part of the lower slope. The reflection from the top of the backstop structure is identified with no reflection patterns below. The most prominent reflector originates from the subducting slab. The BSR, parallel to the lower slope, as well as all other characteristics across the middle and upper slope are distinct in both, the earlier recorded high resolution CDP-1 line in Figure 2.4, [*von Huene and Suess, 1988*], and the lower resolution GEOPECO SO146-5/12°S MCS line in Figure 2.3.

## 2.3 Results from reflection data

The quantification of the characteristic features of the Peruvian margin is obtained from the two coincident MCS lines described above (Figs. 2.3 and 2.4). The Nazca plate shows the typical sediment thickness of the oceanic crust offshore Peru, with  $\sim 150$  m around profile km 70 and  $\sim 0$  m around profile km 75 (Fig. 2.3a and c). The trench axis marks the greatest depression across the margin at  $\sim 8.3$  s TWT ( $\sim 6200$  m water depth). The distinct reflection from the top of the oceanic crust is traced up to 15 km in the GEOPECO SO146-5/12°S MCS line (Fig. 2.3), and more than 30 km in the CDP-1 MCS line (Fig. 2.4) landwards of the deformation front. It originates from the subducting slab underneath the overriding South American plate.

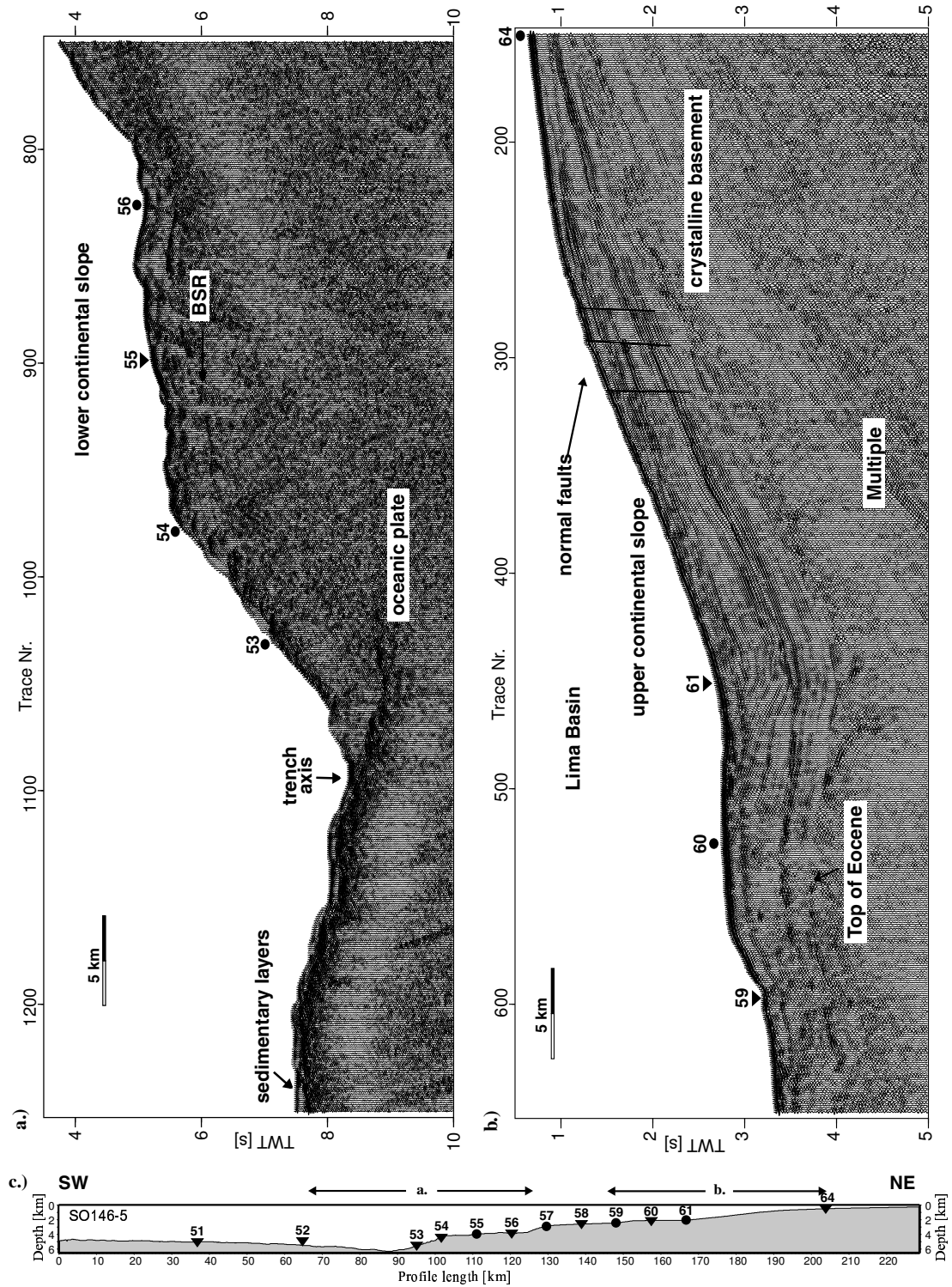


Figure 2.3: Two parts of reflection seismograms from profile SO146-5/12°S are displayed. The seaward part (a), the middle and upper slope (b), and the topography of the entire refraction profile for a better orientation (c) are shown. Locations of OBH/OBS stations are marked with triangles/circles. Vertical exaggeration at seafloor is  $VE = 5$ .

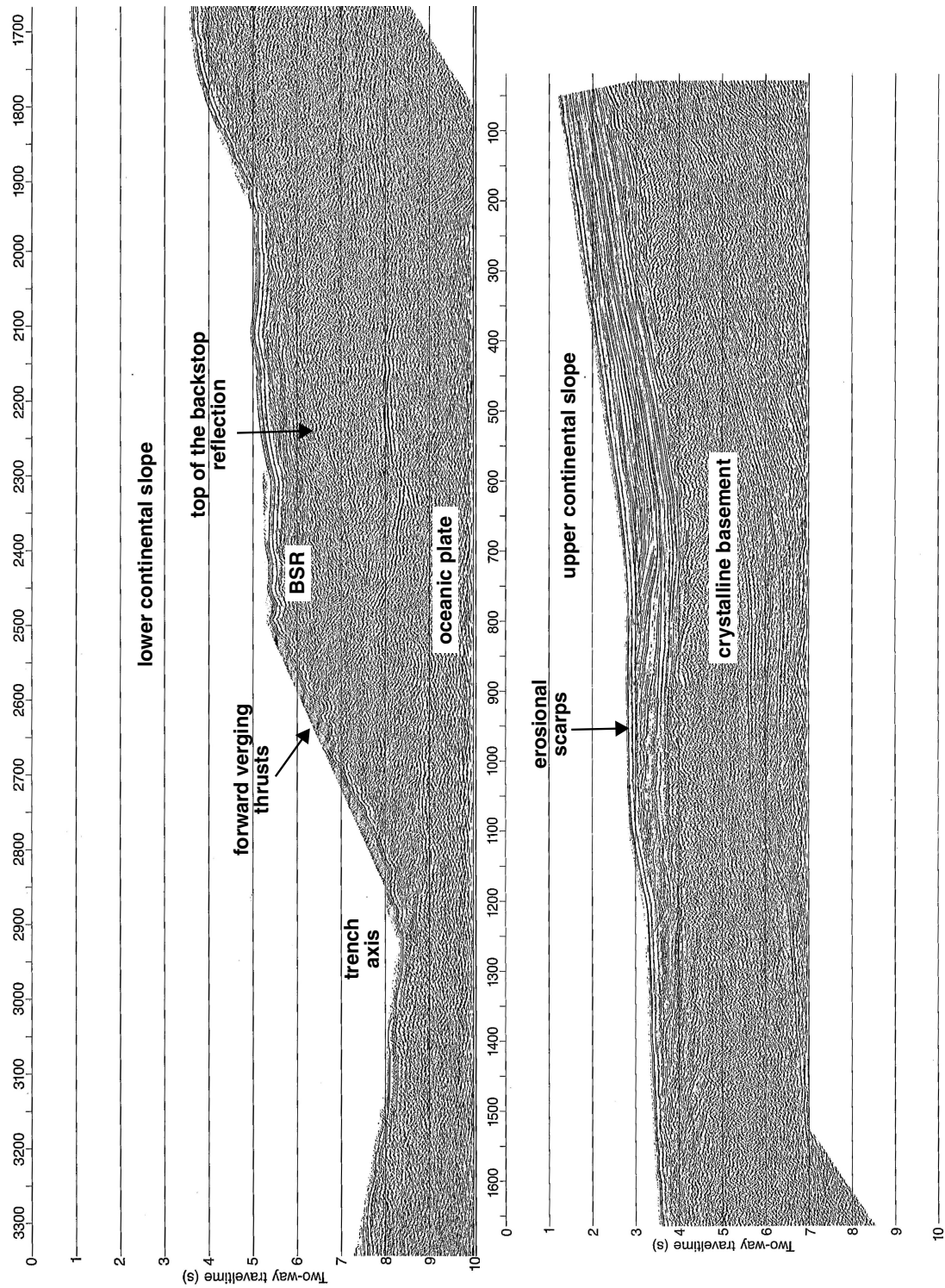


Figure 2.4: The seaward (left) and continental (right) part of the time migrated high resolution MCS data of line CDP-1 from *von Huene and Suess [1988]*, for location see also Fig. 1.3. The line is coincident with the refraction line SO146-05/12° S (compare with Fig. 2.3). Vertical exaggeration V.E.=3.



The BSR on the lower slope indicates the presence of gas hydrates, marking the base of the gas hydrate stability zone. Across the Lima Basin several sediment sequences reveal the erosional and transgressional history of the upper slope and onlap onto the Peru shelf [*Pecher et al., 2001; Clift et al., 2003*]. Extension is indicated by normal faulting. The normal faults marked in Fig. 2.3b around trace number 300, cut through all sedimentary sequences, from the older strata overlying the basement to the recently deposited sediments on the seafloor. Consequently, these faults are active. The interpretation of the horizons, e.g., the identification of the Top of the Eocene, follows *von Huene and Suess [1988]* and *von Huene et al. [1996]*. The thick diffracting section beneath the middle and upper slope of the continental margin marks the horizon of the crystalline basement. The forward verging thrusts (Fig. 2.4) indicate the presence of a small frontal prism and the compressive stress within, originating from the converging plates.

The MCS lines (Figs. 2.3 and 2.4) were used to relate the geological structures to the seismic velocities, obtained by forward modeling (which will be discussed in the following section), especially along the lower and middle slope. The MCS line drawing [*von Huene and Suess, 1988*] of line CDP-1 was correlated with the coincident time-converted refraction model of Profile SO146-5/12°S for a better interpretation (and will be discussed later).



# 3

---

## Determination of seismic velocity models

To obtain the two-dimensional deep structure of the margin and the P-wave velocity field, a forward modeling technique was applied to profiles SO146-3/14°S, SO146-4/9°S and SO146-5/12°S. With this technique not only the first arrivals, but also later refraction and reflection phases could be used to resolve the complex structures on the profiles. Additionally, a tomographic inversion was applied on strike-line SO146-6/12°S. The major horizons (top of oceanic crust, subducting slab, top of the crystalline basement (Top of Eocene; Fig. 2.3b)) identified in the MCS sections are correlated with the reflection phases from the wide-angle data at zero offset (Fig. 3.1) to provide a starting model for forward modeling [Zelt, 1999; Luetgert, 1992].

The reflection and refraction arrivals were identified and picked on all seismic OBH/S sections. Picking accuracy in the seismogram sections is better than 50 ms for the near offset range, as well as for oceanic crustal phases, and is better than 100 ms for large offsets where seismic phases interfere with strong multiple reverberations of the direct wave from previous shots. The above picking uncertainties correspond to an uncertainty in a layer depth of  $\pm 100$  and  $\pm 500$  m if a  $v_{RMS}$  of 2 and 5 km/s is assumed, respectively. Due to reverberations resulting from the shallow water depth on the upper slope and shelf region, picking accuracy decreases in this area for the near offset range on all dip lines. The top of the subducting oceanic plate (designated  $P_{t-oc}$ ; Figs. 2.2 and 3.2–3.8) is well identified on all profiles up to a distance of 60 km landwards of the trench. On all three dip lines north of Nazca Ridge, a reflection from an intracrustal reflector of the subducting oceanic plate (designated  $P_{i-oc}$ , Figs. 3.2, 3.7 and 3.8) is clearly visible. The changing slope of the first arrivals at a distance of around  $\pm 10$  km from the OBH position (refraction from upper crustal layer,  $P_{u-oc}$ , to the refraction of the lower crustal layer,  $P_{l-oc}$ ; enlargement of OBH station 51, Fig. 3.2) additionally supports the existence of the intracrustal boundary in the oceanic crust across the Peruvian margin.  $P_mP_{-oc}$  is the mantle reflection within the subducting oceanic plate with its corresponding refraction  $P_{n-oc}$  (Figs. 2.2 and 3.2–3.8).

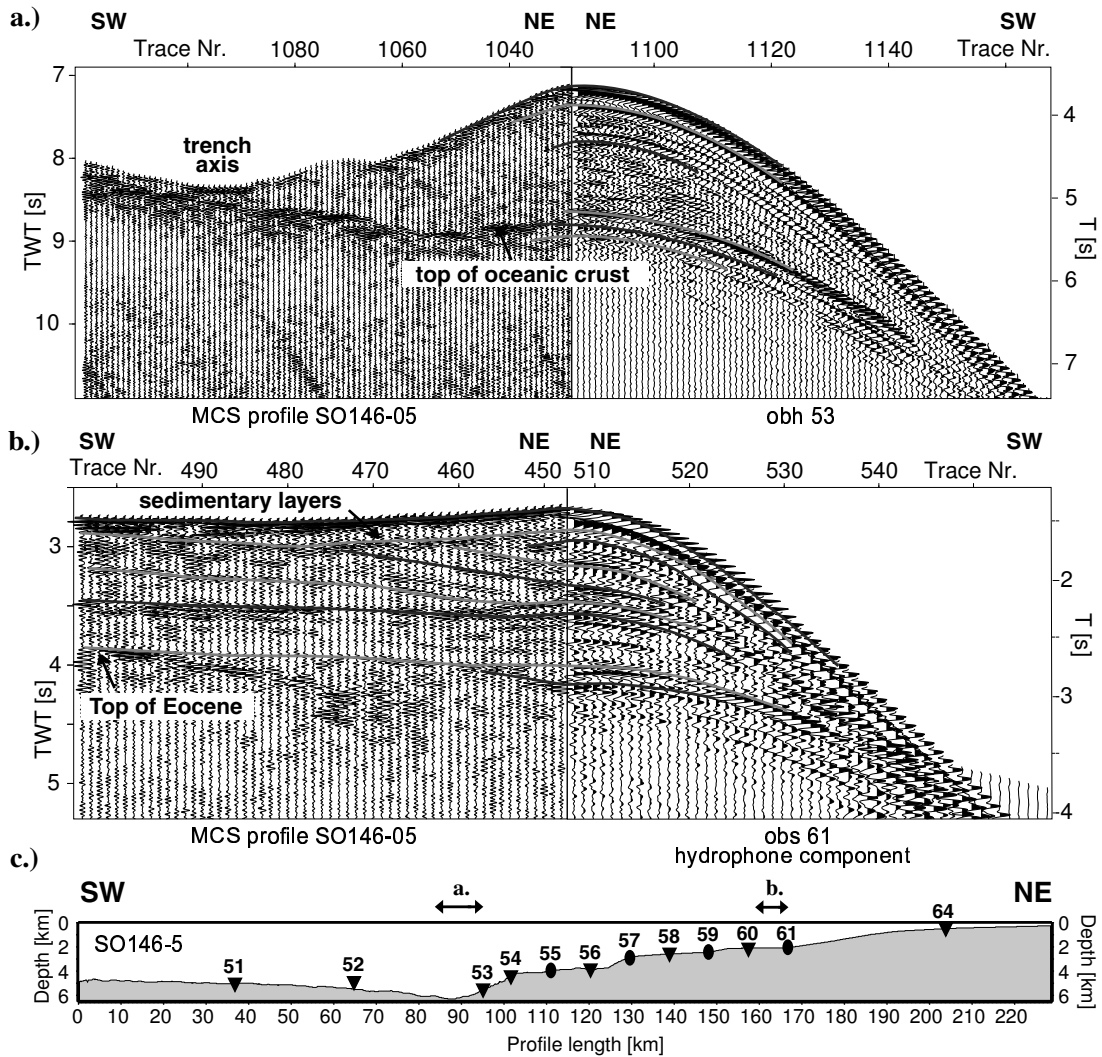


Figure 3.1: Reflection seismograms in the left parts of the figures and OBH/S stations in the right parts of the figures. This type of display supports the identification and correlation of reflection seismic events between MCS and wide-angle seismic data in order to support forward modeling. (a) shows the subducting slab underneath the continental margin, which can be correlated with the  $P_{t-oc}$  phase denoting the reflection from the top of the oceanic crust. The OBH station in this Figure (b) is located at the upper slope of the continental margin. Several sedimentary phases can be identified in both seismic sections as well as the top of the crystalline basement. (c) shows the topography of line SO146-5/12°S and locations of OBH/S stations for orientation.

### 3.1 Forward modeling

A two-dimensional seismic ray tracing method was applied using the MacRay program [Luetgert, 1992]. The layers are defined by their seismic velocities at their top and bottom, which may vary laterally. The interfaces in the model are represented by first or second order discontinuities. The starting model consists of two layers: The water column with the P-wave velocity of 1.5 km/s and a second layer below are divided by the seafloor. The water depth along the profile is known from bathymetric multibeam registration [Bialas and Kukowski, 2000]. The model is expanded by adding layers below the seafloor and changing the velocity model systematically, until the calculated arrivals fit the observed traveltimes of the refraction seismic records. Examples of recorded seismic data superimposed with calculated arrivals for each profile are given in Figures 3.3–3.8. The strong multiple arrivals observed in some OBH/S stations were used to identify seismic events, e.g.,  $P_{n-oc}$  of the downgoing slab on SO146-4/9°S OBH 44 (Fig. 3.3). The modeled data fit the wide-angle data with mean traveltimes deviations being within the picking accuracy.

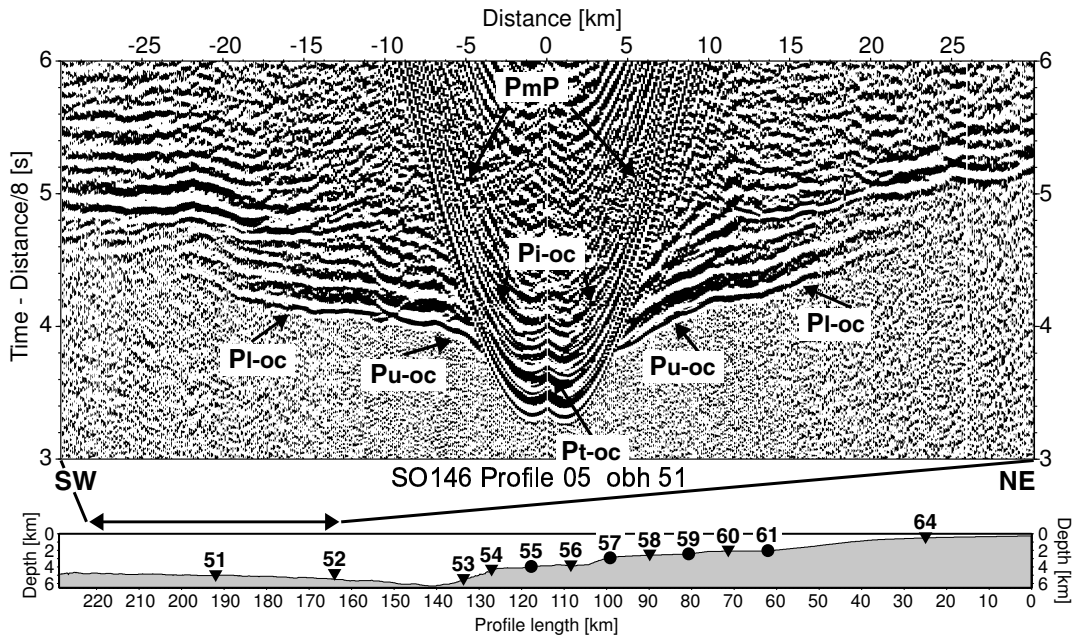


Figure 3.2: Near-offset traces of the wide-angle seismic section recorded by OBH 51 located on the oceanic crust on Profile SO146-5/12°S. The data are displayed with a reduction velocity of 8 km/s.  $P_{t-oc}$ ,  $P_{i-oc}$ ,  $P_{mP}$ : reflections from the top of the oceanic crust, intracrustal boundary, crust-mantle boundary.  $P_{u-oc}$ ,  $P_{l-oc}$ : refractions from the upper oceanic crust, lower oceanic crust. The topography along the entire profile is shown underneath the seismic section with all the locations of the OBH/S stations, triangles/circles mark OBH/OBS stations.

### 3.1. FORWARD MODELING

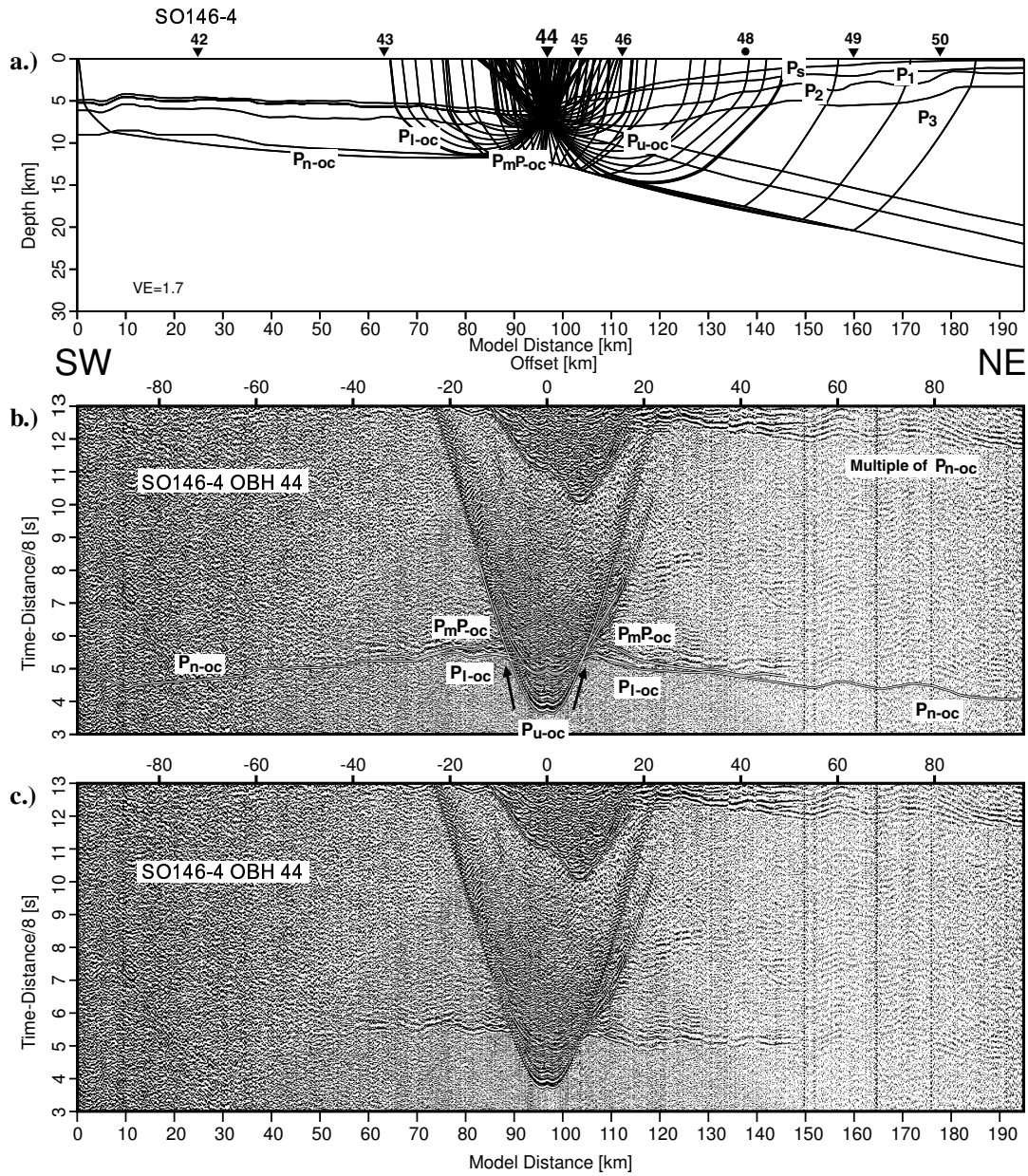


Figure 3.3: The  $P$ -velocity model (a) for profile SO146-4/9°S is shown with representative ray paths calculated for the seismic section below. The record section OBH 44 on the continental margin (b, c), overlain with traveltimes curves (b).  $P_mP_{-oc}$ : oceanic Moho reflection;  $P_{n-oc}$ : oceanic mantle refraction;  $P_s$ : refraction from continental sediment. Location of OBH/S stations at 9°S are shown on the left.

### 3. DETERMINATION OF SEISMIC VELOCITY MODELS

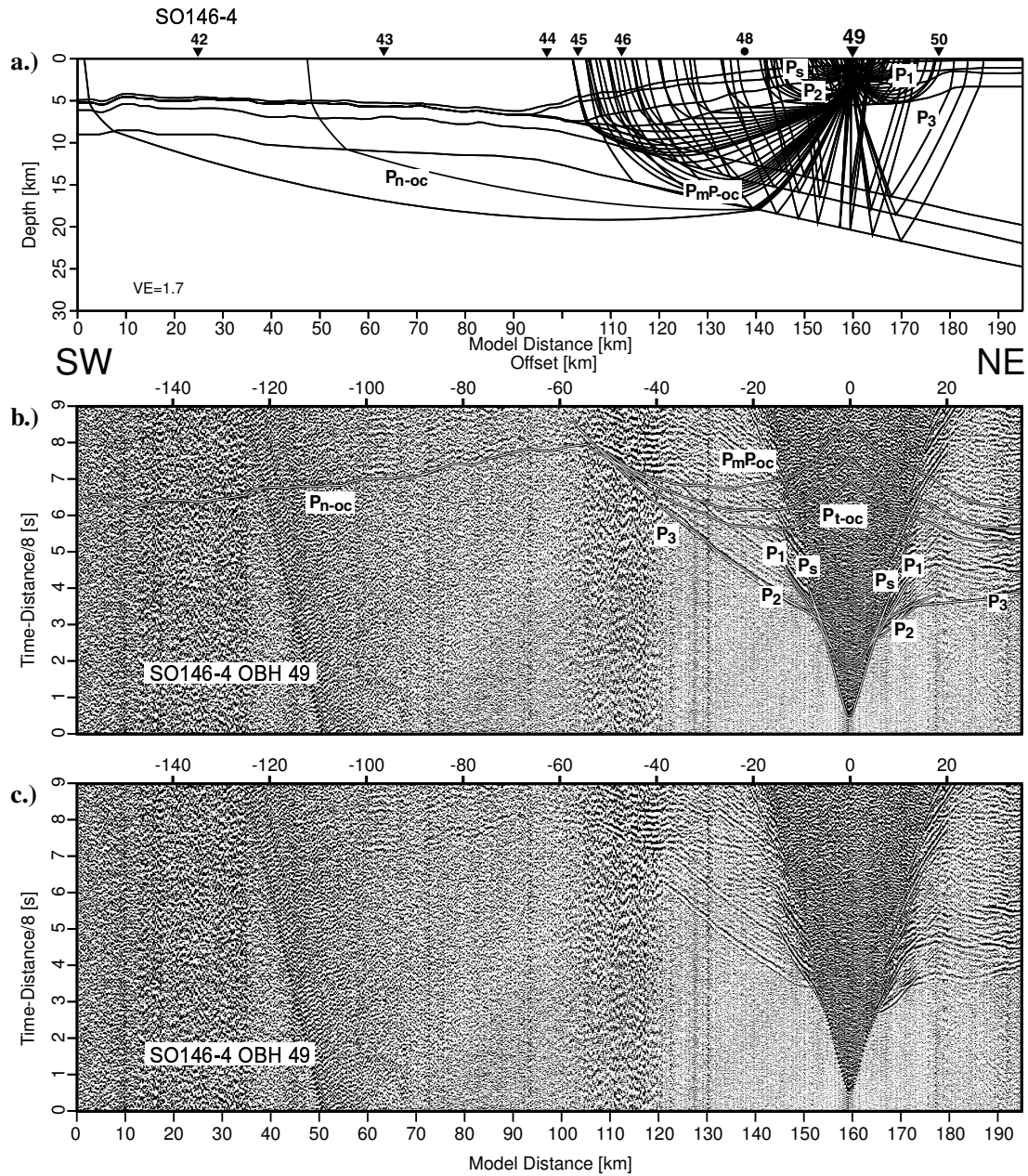


Figure 3.4: The  $P$ -velocity model (a) for profile SO146-4/9°S is shown with representative ray paths calculated for the record section OBH 49 on the upper slope (b, c), overlain with traveltime curves (b).  $P_{t-oc}$ : reflection from top of oceanic crust;  $P_{i-oc}$ : intracrustal reflection on oceanic plate;  $P_1 - P_3$ : refractions from continental interfaces. See Figure 3.3 for further details and definitions of abbreviations.

### 3.1. FORWARD MODELING

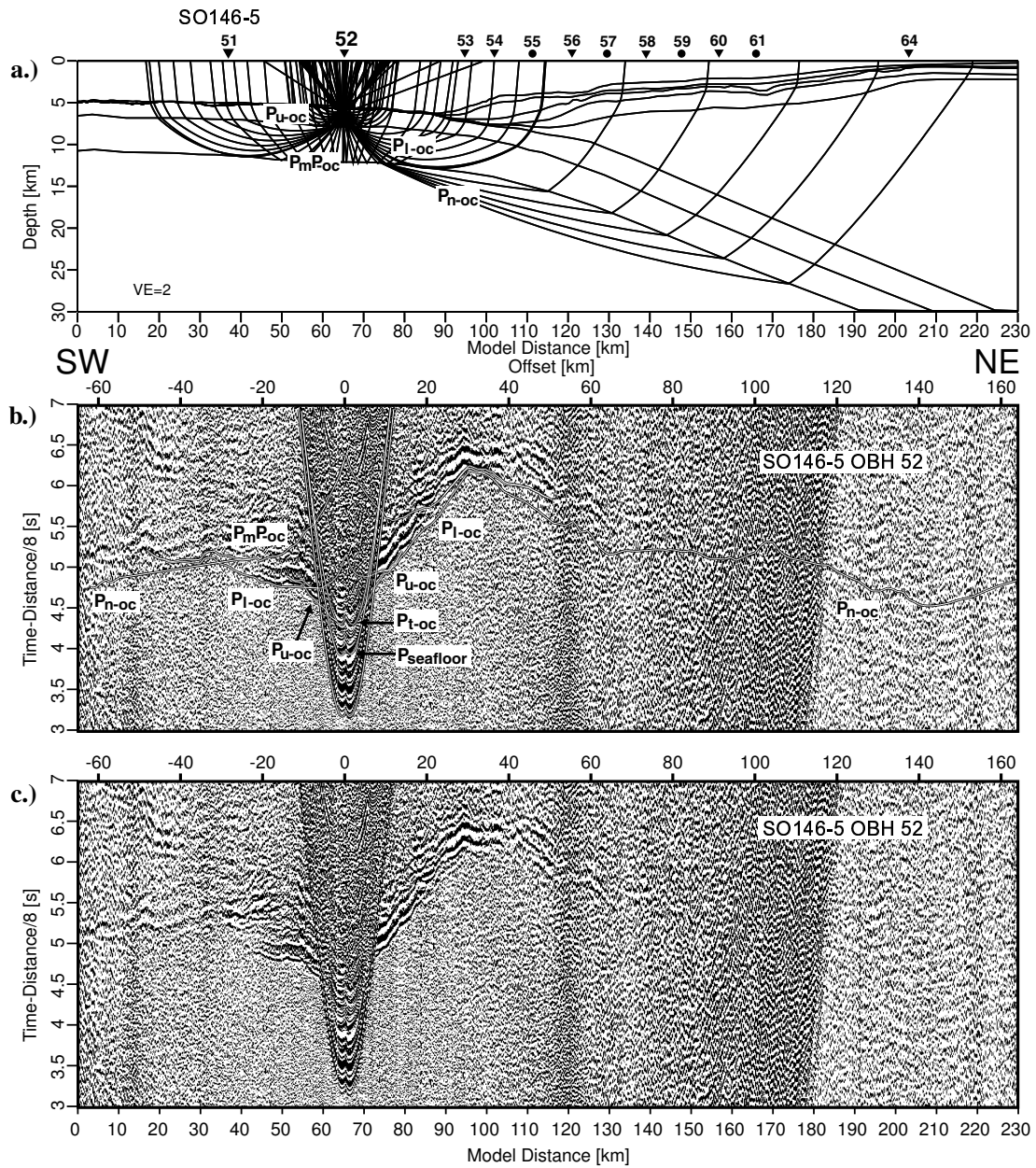


Figure 3.5: The P-velocity model for profile SO146-5/12°S (a) with record section OBH 52 (b, c) located on the oceanic crust. The seafloor reflection in record section OBH 52 is not coincident with the direct arrival, because the instrument was placed 600 m above the seafloor. Location of OBH/S stations at 12°S are shown on the left. See Figures 3.3 and 3.4 for details and definitions of abbreviations.



### 3. DETERMINATION OF SEISMIC VELOCITY MODELS

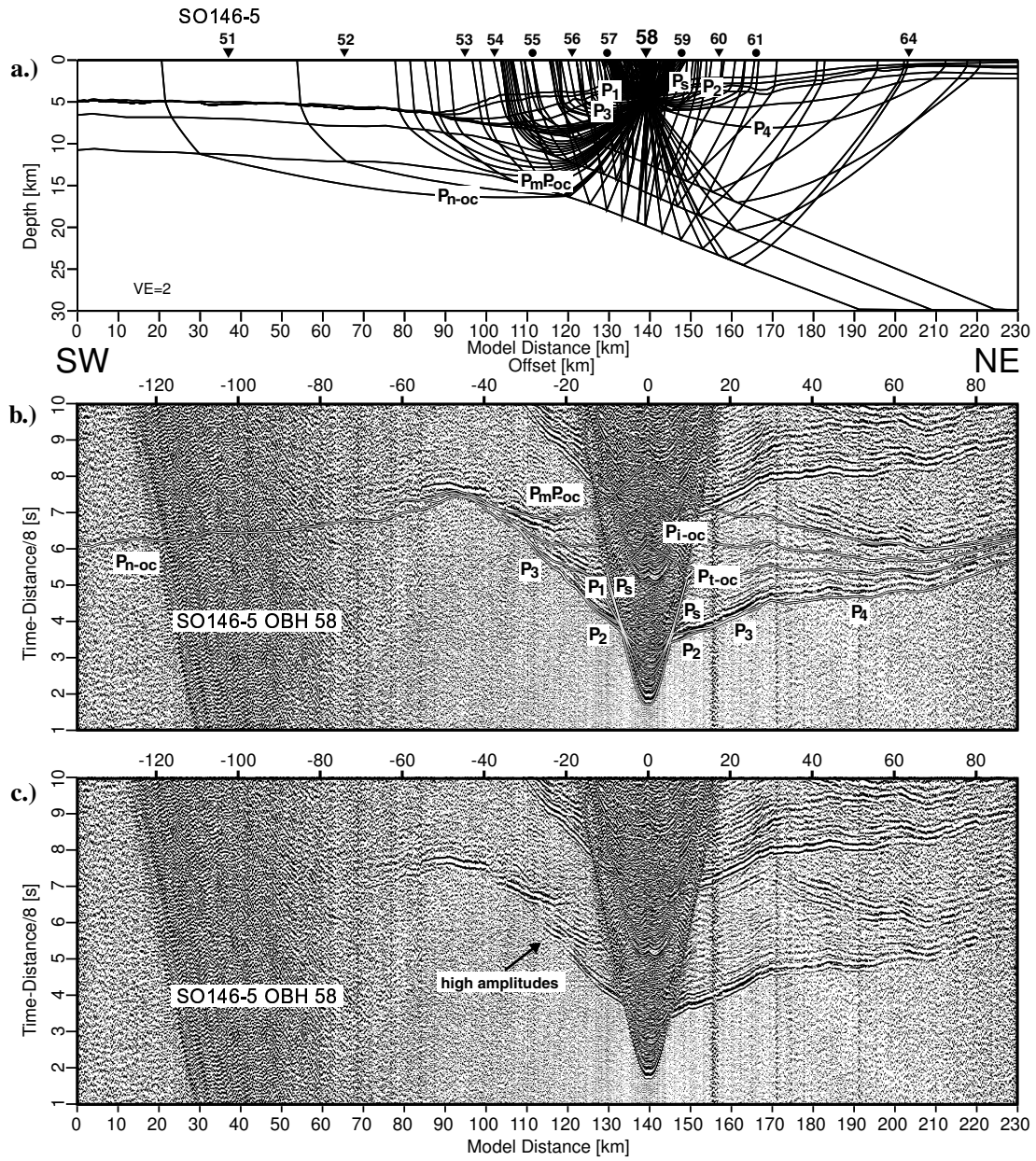


Figure 3.6: The P-velocity model for profile SO146-5/12°S (a) with record section OBH 58 (b, c) located on the middle slope. See Figures 3.3 and 3.4 for details and definitions of abbreviations.

### 3.1. FORWARD MODELING

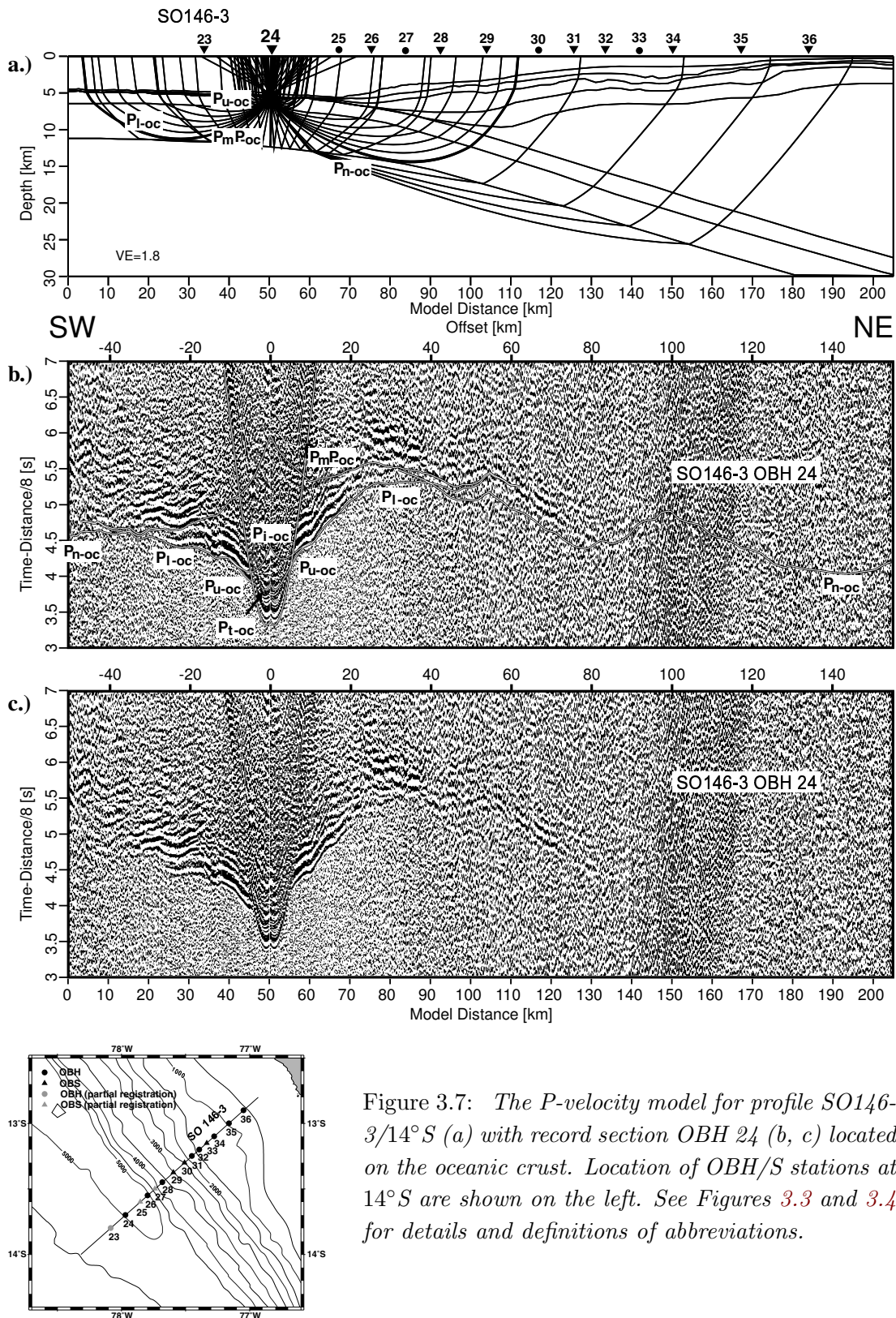


Figure 3.7: The  $P$ -velocity model for profile SO146-3/14°S (a) with record section OBH 24 (b, c) located on the oceanic crust. Location of OBH/S stations at 14°S are shown on the left. See Figures 3.3 and 3.4 for details and definitions of abbreviations.

### 3. DETERMINATION OF SEISMIC VELOCITY MODELS

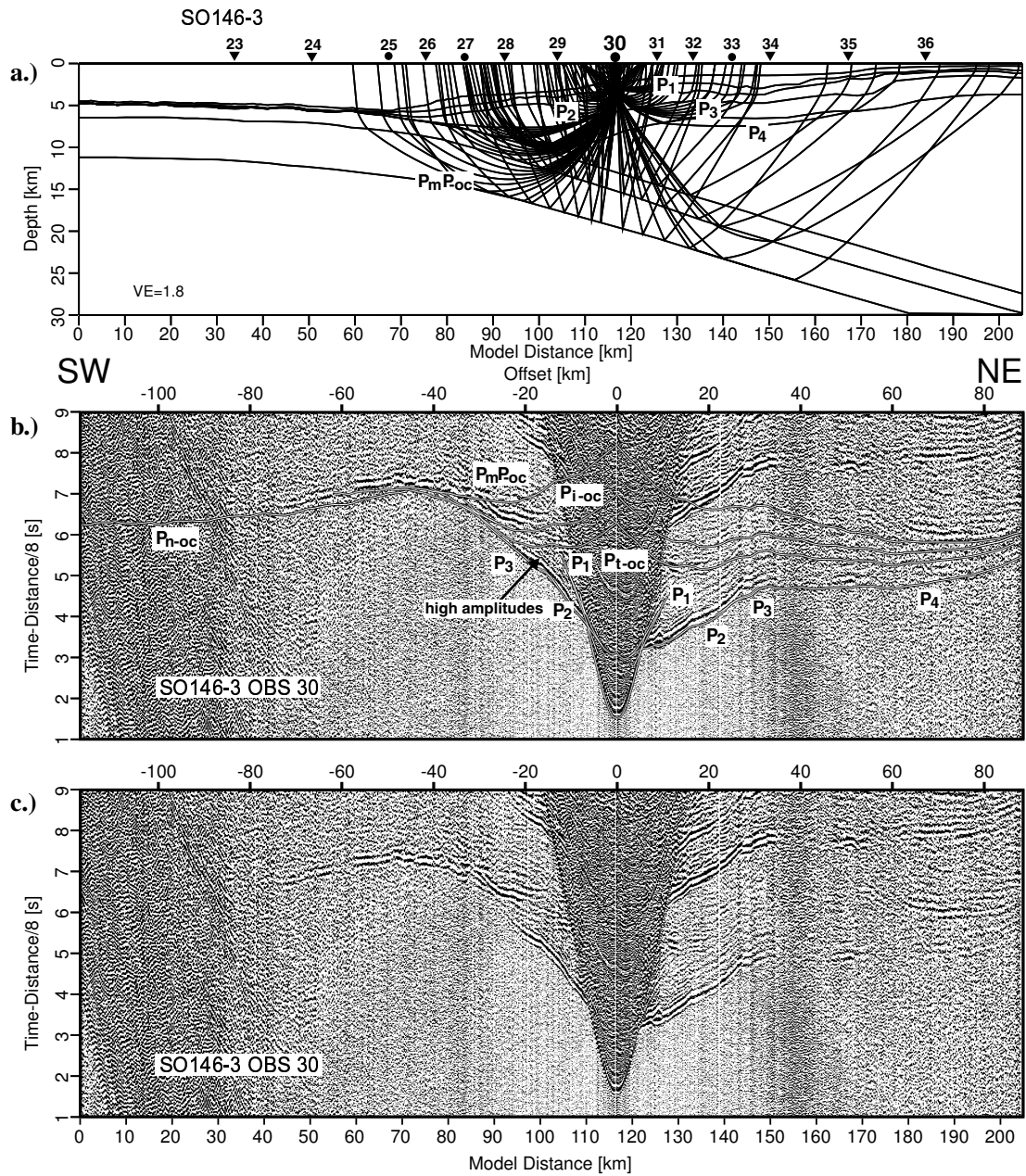


Figure 3.8: The P-velocity model for profile SO146-3/14°S (a) with record section OBS 30 (b, c) located on the middle slope. See Figures 3.3 and 3.4 for details and definitions of abbreviations.

### 3.2 Tomographic inversion

Line SO146-6/12°S is the crossline of profile SO146-5/12°S with a denser OBH/S spacing of about 10 km. A data example will be given in the section 'Amplitude modeling'. This geometry allows a tomographic inversion on this profile to derive the P-wave velocity structure underneath the Lima Basin using the First Arrival Seismic Tomography (FAST) code [e.g., *Zelt and Barton, 1998*; *Kopp et al., 2004*]. A flowchart of the constituent steps of the tomographic method is given in Figure 3.9.

Only the first arrivals of the seismic records were picked and used for the traveltimes inversion (Fig. 3.10). First arrivals were generally picked within an accuracy of 30 ms for the near offset range and 80 ms for far offsets. Picking uncertainty is not more than 120 ms for phases, which were not confidently identified.

The velocity distribution obtained along line SO146-5/12°S by forward modeling at the junction with crossline SO146-6/12°S at OBS station 70, served as starting model (Fig. 3.11a). The starting model consists of velocity gradients increasing with depth, which are laterally not varying (one-dimensional starting velocity-depth model). Velocity isolines are indicated by dotted lines, but they are not representing boundaries in the starting model as well as in the final model (Fig. 3.11a, b). An iterative approach is employed by the FAST program, in which new raypaths are calculated for each iteration. The velocity-depth distribution is verified at each iteration until the calculated fit the picked traveltimes allowing a user-specified uncertainty, which is here within the picking accuracy (as discussed above). The forward calculation of traveltimes and raypaths, incorporated in the FAST tomography program, uses the *Vidale [1988, 1990]* scheme.

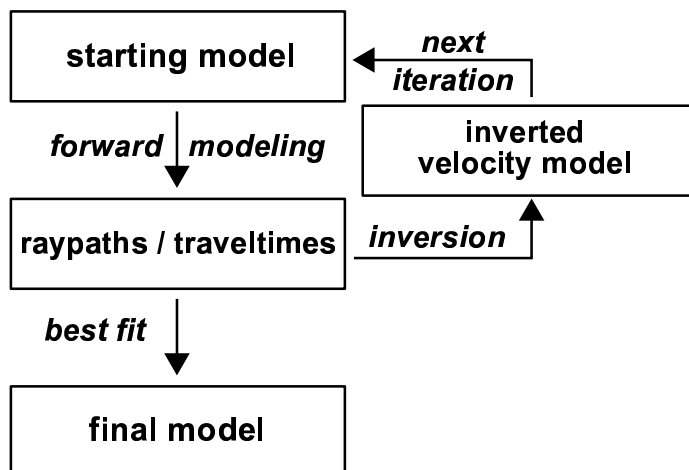


Figure 3.9: *Flowchart of the FAST inversion method. A detailed description of the constituent steps of the algorithm is given in the text.*

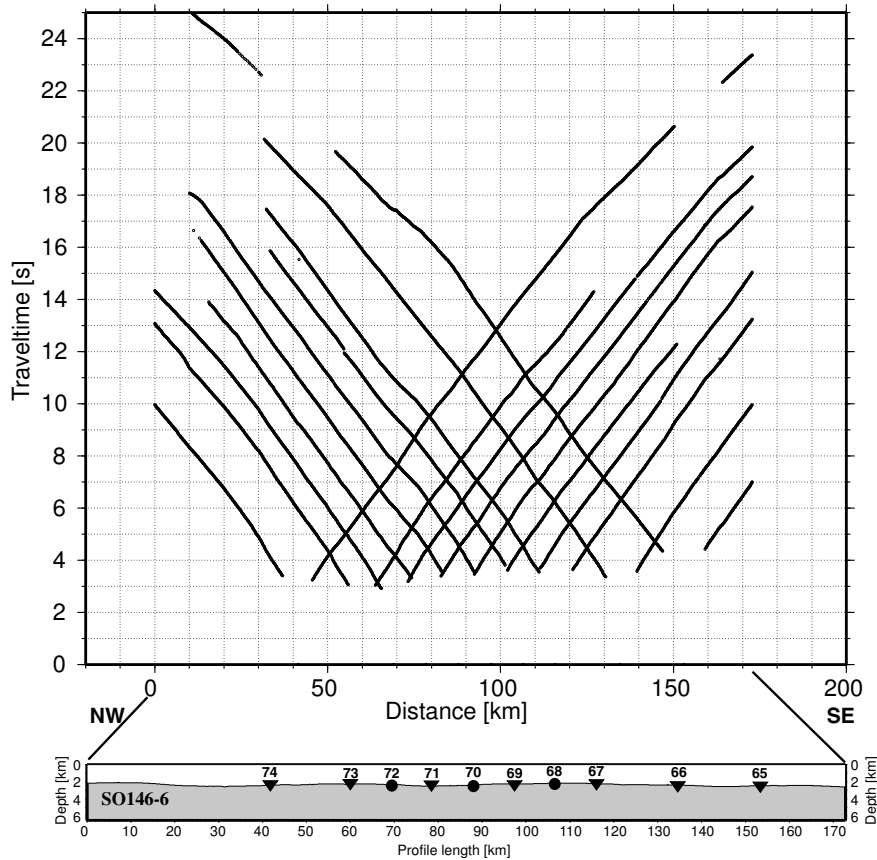


Figure 3.10: *First arrivals picked across the 10 OBH/OBS stations of line SO146-6/12°S, which were used for the tomographic inversion. The topography of this profile and the positions of the OBH/OBS stations, marked by triangles/circles, are shown below the picks.*

The [Vidale \[1988, 1990\]](#) method calculates first arrival traveltimes on a uniform grid by solving the eikonal equation by finite differencing. This algorithm is modified by [Hole and Zelt \[1995\]](#) to handle large velocity gradients or contrasts. After six iterations, the final model is obtained by this tomographic method, which shows little lateral P-wave velocity variations (Fig. 3.11b). The resolution of the model can be shown by the ray coverage. A coverage of up to 2000 hits per cell is achieved, which yields good resolution of the crustal structure and the boundary between the continental and the subducting oceanic plate. There is a sparse coverage in the peripheral region of the model (Fig. 3.11c).

### 3.2. TOMOGRAPHIC INVERSION

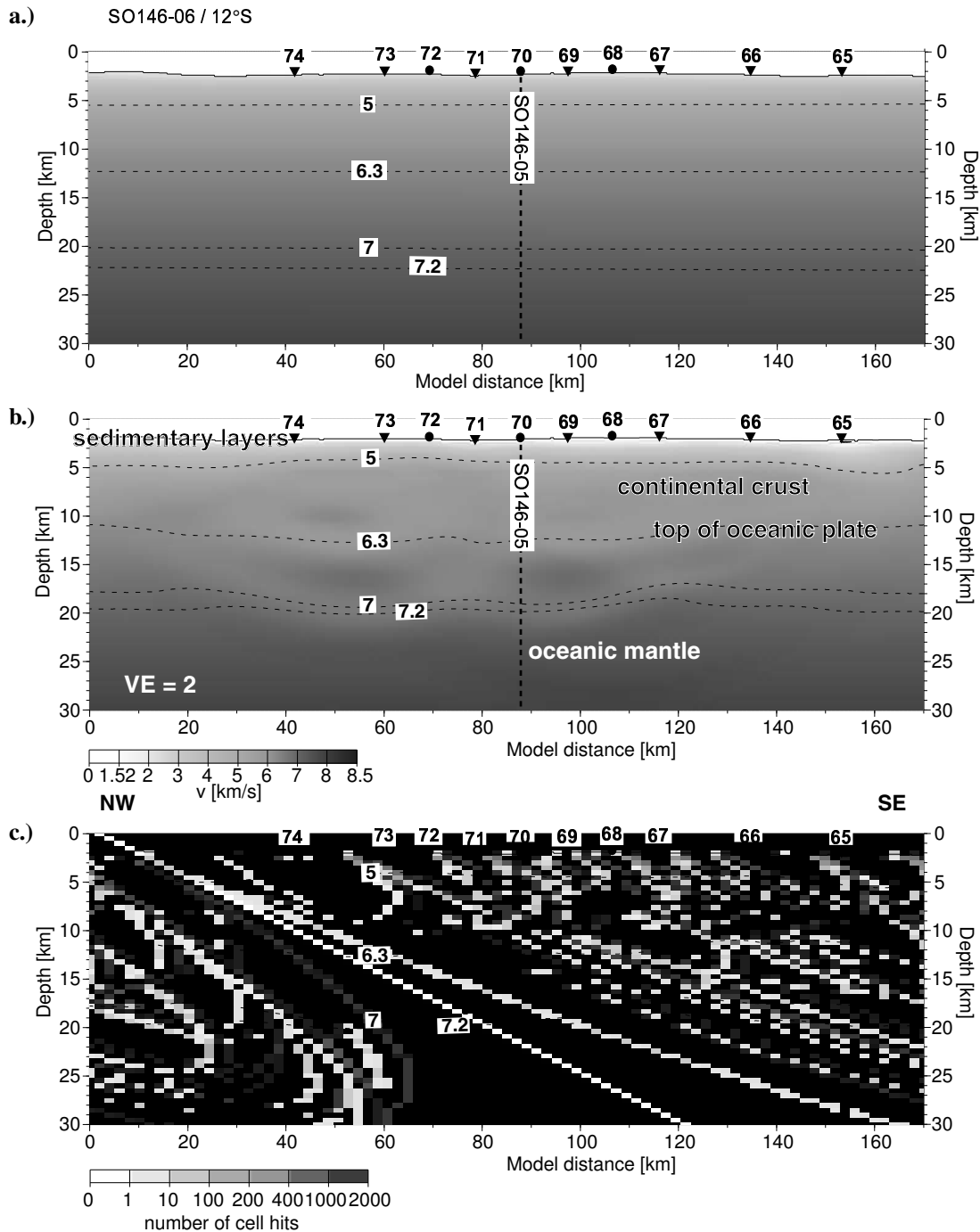


Figure 3.11: *Tomographic inversion of line SO146-6/12°S along strike of the middle slope of Lima Basin. The starting model and the result are shown in (a) and (b), respectively. The dashed lines are P-wave velocity isolines and the gray shade code for the velocities can be drawn from the scale. Vertical exaggeration  $VE = 2$ . (c) shows the coverage of the seismic tomographic inversion, note the scale below. The resolution is good with some restrictions in the lower corners of the model. Triangles/circles mark OBH/OBS stations.*

### 3.2.1 Sensitivity of the FAST algorithm

To assess the lateral resolution of the model, a "checkerboard" test [e.g., *Hearn and Ni, 1994; Zelt and Barton, 1998*] is applied. Therefore, the starting model (see Fig. 3.11a) is superimposed with a laterally and vertically varying velocity anomaly pattern of squares of the size of  $13 \text{ km} \times 8 \text{ km}$  with alternating values. The velocities of the anomaly pattern are varying from  $\pm 5\%$  for the upper 10 km and  $\pm 3\%$  below. Only the velocity model below the seafloor is accounted for. Synthetic traveltimes and raypaths are calculated for this "checkerboard" model, using the real data's source-receiver geometry. Gaussian noise is added to the synthetically calculated picks with a standard deviation equal to the pick uncertainties. The tomographic inversion of the calculated picks using the starting model (with superimposed velocity anomaly pattern) recovers the anomaly pattern (Fig. 3.12). The recovered anomaly pattern gives an estimate of the model's ability, along with the used source-receiver geometry and noise level, to resolve anomalies with lateral dimensions equal to the size of the anomaly pattern (scale in Fig. 3.12). The resolution of the model is good underneath the positions of the OBH/S stations and it breaks down, where the ray coverage is poor, compare Figures 3.11c and 3.12.

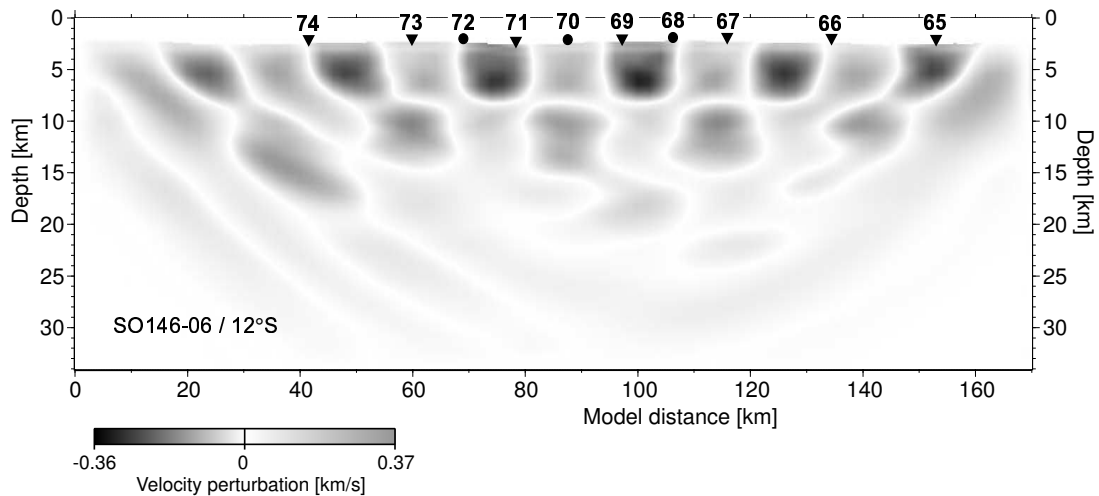


Figure 3.12: *Sensitivity of the FAST tomographic inversion algorithm applied to the refraction model of line SO146-6/12°S. The gray shade code for the P-wave velocities of the anomaly pattern can be drawn from the scale. Vertical exaggeration  $VE = 2$ . The resolution is good with some restrictions in the lower corners of the model. Triangles/circles mark OBH/OBS stations. Compare also with Figure 3.11c.*





# 4

## Results and discussion of the refraction data

### 4.1 The oceanic plate

Oceanic crust is produced at spreading centers at mid oceanic ridges (see cartoon, Fig. 4.1) and subducted where it is colliding with a continental plate, or may be overriding at an oceanic-oceanic plate collision zone [Press and Siever, 2003]. The crust at a spreading center is thin and thickens with age as it departs from the spreading center and cools down [e.g., Le Pichon et al., 1965; Goslin et al., 1972]. Marine geophysical investigations reveal a worldwide uniform structure of the oceanic crust. It is partly covered by sediment layers (Layer 1). The oceanic crust is divided into an upper and a lower crustal layer. The upper crust (Layer 2a, b) consists of extrusive basaltic lavas and dykes. The lower crustal layer (Layer 3) mainly consists of intrusive Gabbros [White et al., 1992]. Layer 2 and 3 both comprise the igneous section of the oceanic crust with little variable thickness globally.

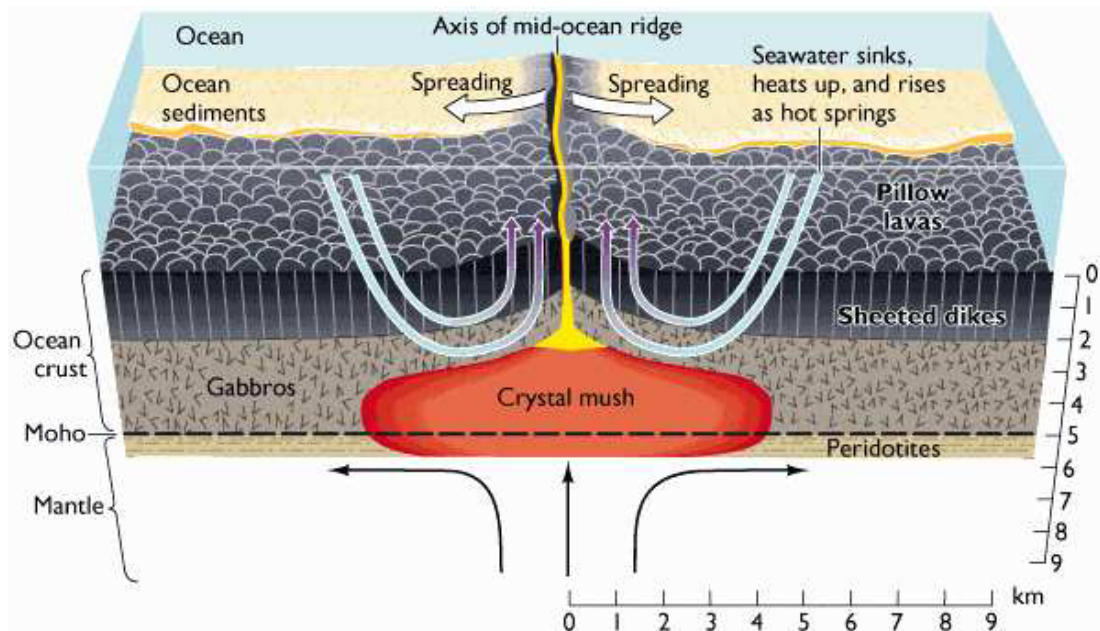


Figure 4.1: Schematic diagram of the production and structure of the oceanic crust, taken from Press and Siever [2003].

In the following, this is referred to 'normal' oceanic crust. Anomalous oceanic crustal thickness is known from several geological settings in oceanic basins, including fracture zones, seamounts, elevated regions surrounding hot spots, aseismic ridges (e.g., Nazca Ridge offshore Peru), and extremely young crust under active spreading centers [e.g., [Walther, 2003](#); [White et al., 1992](#)].

#### 4.1.1 General seismic velocity-depth distributions

The oceanic crust cools and therefore its density increases with increasing distance to the spreading center. Consequently, the seismic velocities of the oceanic crust rise as well with increasing crustal age and distance to the mid-ocean ridge axis. The seismic velocities of 0–5 Ma old upper oceanic crust have an average value of 2.83 km/s and only rarely >4 km/s [[Carlson, 1998](#)]. Velocity sections of different oceanic crustal ages for the Pacific ocean are given in Figure 4.2. Seismic velocities of oceanic crust >5 Ma are >4 km/s with an average value of 4.44 km/s. The transition of lower to higher upper crustal seismic velocities occurs in 1–5 Ma old oceanic crust [[Carlson, 1998](#)]. The velocities of the upper oceanic crustal layer show stronger variations compared to the lower oceanic crust, which results from a higher degree of fracturing, porosity and weathering of the more exposed upper oceanic crust. The average seismic velocity of the lower oceanic crust is  $\sim 6.8$  km/s [[Walther, 2003](#)]. A global compilation of the results of seismic studies gives an average thickness of the oceanic crust of  $7.1 \pm 0.8$  km. The Mohorovičić Discontinuity (Moho) is the boundary between the oceanic crust and the mantle. It is characterized by a sudden jump of the seismic velocities to values >7.6 km/s.

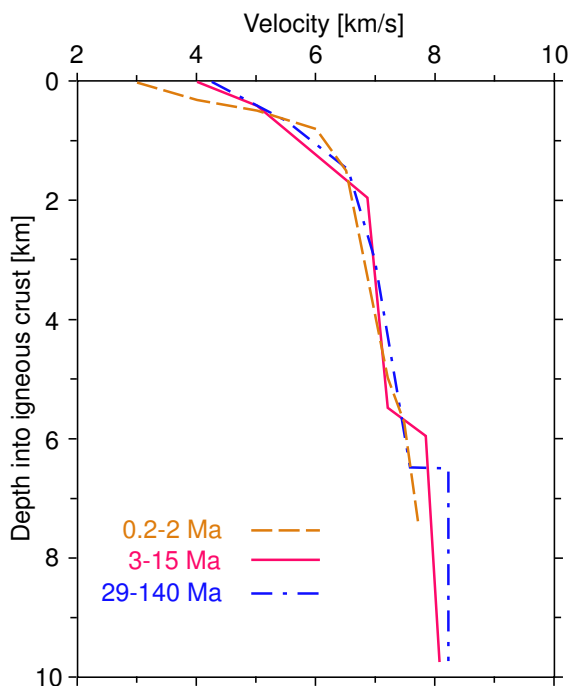


Figure 4.2: *Distribution of the seismic P-wave velocities of the oceanic crust in the Pacific ocean, modified after [White et al. \[1992\]](#). Note the lower velocities of the young upper oceanic crust compared to the older oceanic crust.*

Therefore, the reflections in the seismic records originating from the Moho show high amplitudes due to the strong impedance contrast. The upper mantle consists mainly of peridotites. Average values for seismic velocities of the upper mantle are 7.9–8.0 km/s, but velocities  $>7.6$  km/s are considered being mantle velocities [White *et al.*, 1992]. The global seismic velocity-depth distribution of the 'normal' oceanic crust and upper mantle is given in Figure 4.3.

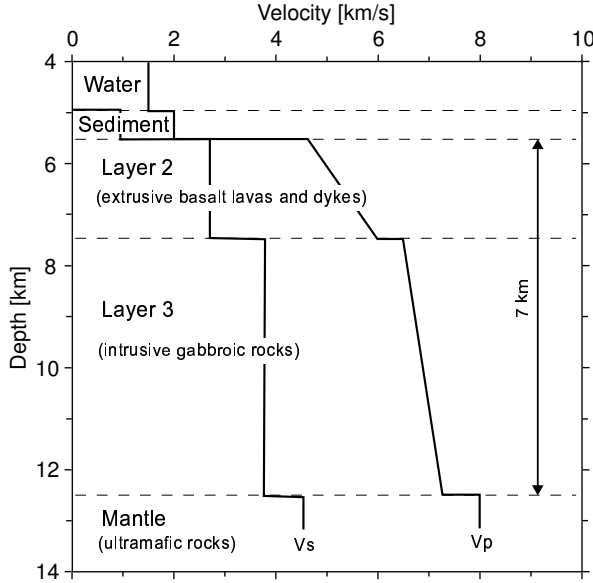


Figure 4.3: Schematic diagram of the 'normal' oceanic crustal structure and the seismic velocities, modified after White *et al.* [1992].

#### 4.1.2 The crustal structure of the oceanic Nazca plate

The crustal structure of the Nazca plate was determined from the reflected P-waves at the top of the oceanic crust  $P_{t-oc}$ , the intracrustal reflection  $P_{i-oc}$  (boundary between Layer 2 and 3) and the reflection from the crust-mantle interface  $P_mP$ . The refracted waves traveling through the upper crustal layers (Layer 2)  $P_{u-oc}$  are consistent with velocities gradually increasing from 4.7–6.1 km/s and the refractions of the lower crustal layer (Layer 3)  $P_{l-oc}$  with velocities from 6.4–7.3 km/s with some small regional variations (see the traveltime curves in Figures 3.3–3.8, 4.5 and 4.6).

The oceanic crust has a mean total thickness of 6.4 km comprising a 1.6–2.1 km thick upper crustal layer and a lower crust with 4.2–5.2 km thickness (Fig. 4.4). The position of the Moho and the velocity distribution in the upper mantle were derived from the P-waves reflected (at pre- and postcritical angle) at the crust mantle interface  $P_mP$  and the corresponding refraction  $P_n$  (Figs. 3.3b–3.8b and 3.3c–3.8c). Coincident MCS data (line 1018, the landward part published by von Huene and Suess [1988]) constrain the position of the Moho on profile SO146-5/12°S at 2.1 s TWT below seafloor [R. von Huene, pers. communication]. The mean Moho depth is about 6–7 km below the seafloor and the mean P-wave velocity of the mantle is about 7.9 km/s, averaged over the three refraction transects north of Nazca Ridge.

### Differences in the oceanic Nazca plate from North to South

The Nazca plate shows an overall rough topography, as revealed by satellite derived predicted bathymetry (Figs. 1.1 and 1.4) and more detailed swath bathymetry published by *Kukowski et al.* [2002]. This is also apparent in the wide-angle seismic data, e.g., the undulations of the refracted phase that traveled through the lower crust. It is denoted as  $P_{l-oc}$  at the westernmost part of the model originating from Trujillo Trough in Figs. 4.5. There are differences in the oceanic crust north and south of Mendaña Fracture Zone, which are discussed below. Trujillo Trough is located on the westernmost part of profile SO146-4/9°S (Fig. 1.4) and is characterized by a graben-like structure, which is 5 km wide with a vertical offset of about 500 m at the seafloor. This graben-like structure also extends into the igneous crust (Fig. 4.4a). Modeled traveltime curves of this line compared with the seismic refraction dataset, e.g., OBH 42 in Figure 4.5, are consistent with the downward continuation of Trujillo Trough to the Mohorovičić discontinuity (Moho) depth, 4 km below the seafloor, which is anomalously thin compared to the average 6.4-km-thick oceanic crust offshore Peru [*Krabbenhöft et al.*, 2004]. Gravity modeling [*Heinbockel et al.*, 2003] supports the results obtained from the refraction seismic data of the oceanic crustal structure in the Trujillo Trough region. Immediately east of Trujillo Trough the crust is elevated about 1 km relative to that west of the trough, as far as profile km 35. This elevation is concurrent with a very thin sediment layer and a relatively thin oceanic crust of about 4 km thickness, comprising the upper and lower oceanic crust (Layer 2 and 3) (Figs. 4.4a, 4.5, and 4.6). The model is consistent with the arrivals of the Moho reflection occurring  $\sim 1.7$  s two-way traveltime (TWT) after the direct arrival at OBH station 42, and 2.1 s TWT at OBH station 43 ( $P_m P_{-oc}$ , Figs. 4.5, and 4.6), with 'normal' oceanic crustal thickness. This 30 km long segment of thinned oceanic crust (Fig. 4.4a) is linked to the east-west extensional regime proposed by *Huchon and Bourgois* [1990]. The topographic highs and lows trending perpendicular to Mendaña Fracture Zone, and which are located eastwards of Trujillo Trough in the vicinity of OBH 43 persist downward at least until the intracrustal oceanic boundary (between Layer 2 and 3) (Figs. 1.4 and 4.4).

The oceanic crust south of Mendaña Fracture Zone differs from the structures observed in profile SO146-4/9°S. The ocean floor shows a rough topography, but without a specific orientation and in contrast to the northern line (SO146-4/9°S). This rough topography along profiles SO146-5/12°S and SO146-3/14°S extends only to the upper crustal boundary (top of Layer 2) but not to the Moho. The velocity model of profile SO146-5/12°S (Fig. 4.4b) is consistent with a very thin sedimentary layer, locally with a maximum thickness of about 200 m. The rough oceanic crust sporadically outcrops, e.g., between profile length 20–30 km. No oceanic crust crops out on the southern profile SO146-3/14°S (Fig. 4.4c) that has a sedimentary cover that reaches a maximum thickness of 200 m. The oceanic crustal layers (comprising Layer 2 and 3) of these two seismic models are overall similar. Comparing the crustal thicknesses of profiles SO146-5/12°S and SO146-3/14°S, there is an increase of about 0.5 km towards the south, which is likely reflecting the outermost edge of the Nazca Ridge.

#### 4. RESULTS AND DISCUSSION OF THE REFRACTION DATA

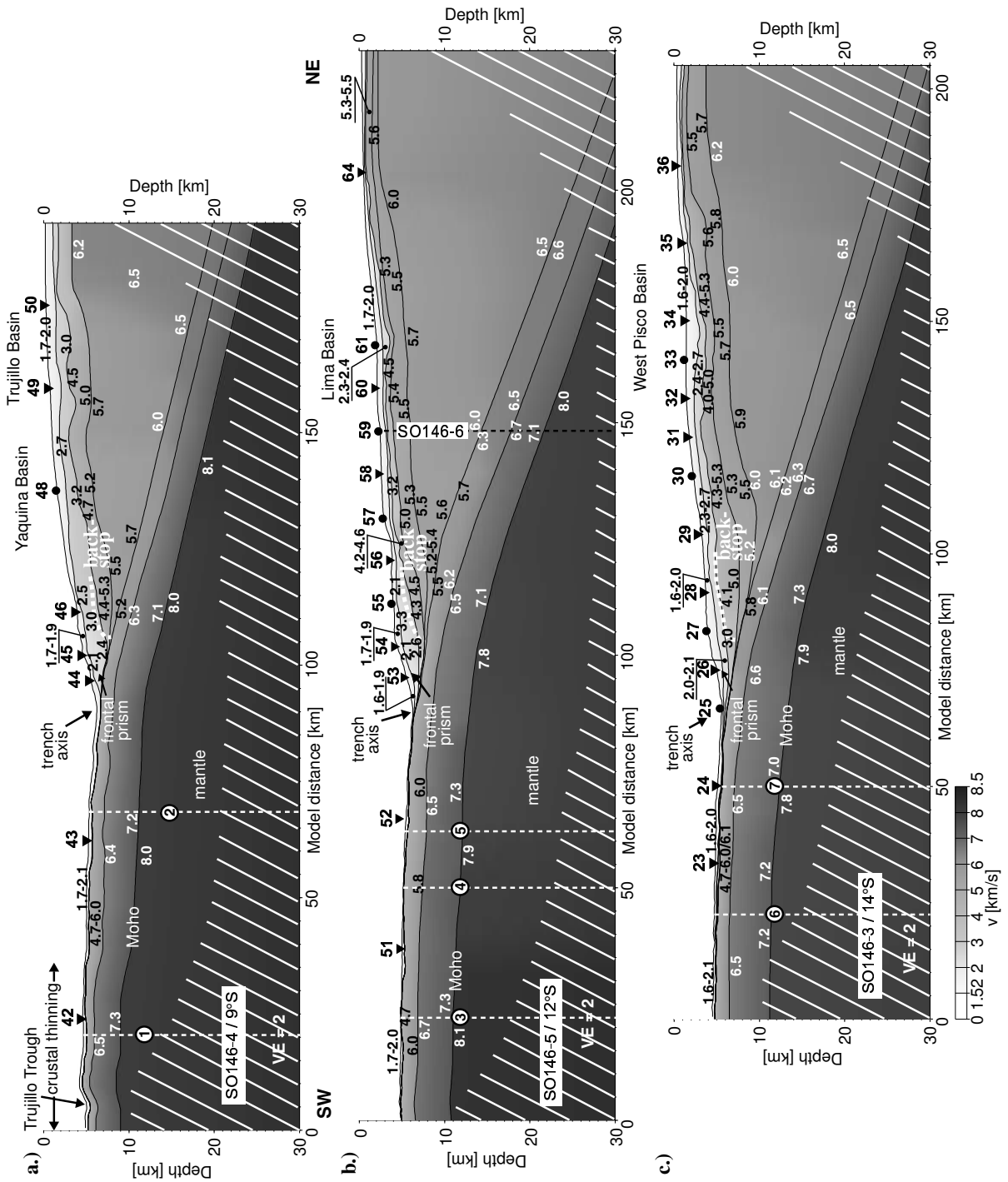


Figure 4.4: Models obtained from forward modeling of the seismic refraction profiles [Krabbenhöft et al., 2004] are displayed from north to south. Note the values of the seismic P-wave velocities in the scale below. Locations of the crossing profile/selected velocity-depth distributions are indicated by the black (b)/white dashed lines ① – ⑦. Locations of the OBH/OBS stations are marked by triangles/circles. Only the seaward-most portion of the backstop is marked by a dotted line, it extends further landwards. The white hatched area is not constrained by seismic observations.

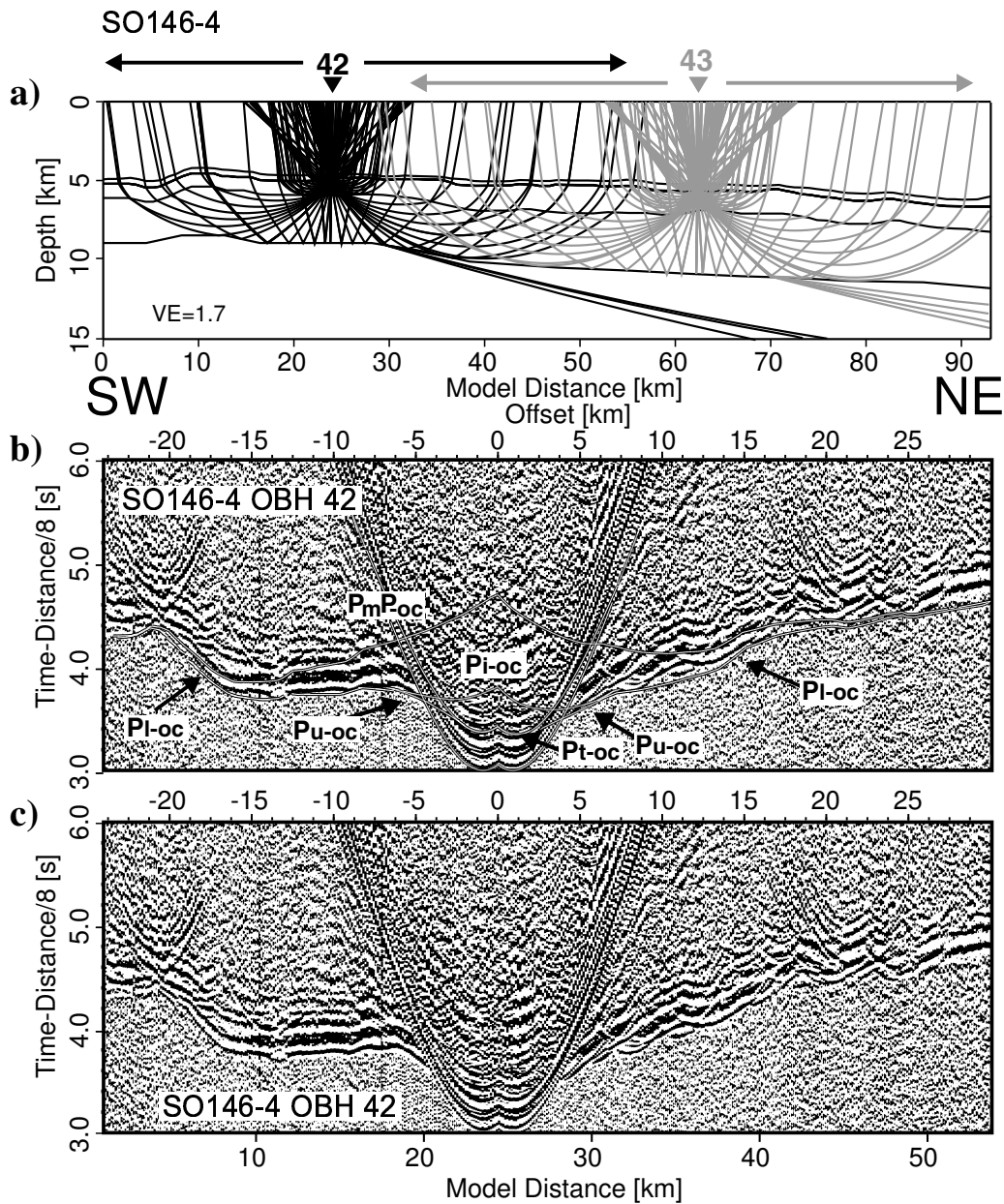


Figure 4.5: *Enlargement of the P-velocity model (a) for profile SO146-4/9°S shown with representative ray paths calculated for the seismic sections below and Figure 4.6. The regions covered by the enlargement of the seismic sections are marked above the model. Enlargements of record section OBH 42 and OBH 43 (Fig. 4.6) for comparison of the oceanic crustal thickness along the profile (c) are overlain with traveltimes curves (b). See Figures 3.3 and 3.4 for details and definitions of abbreviations.*

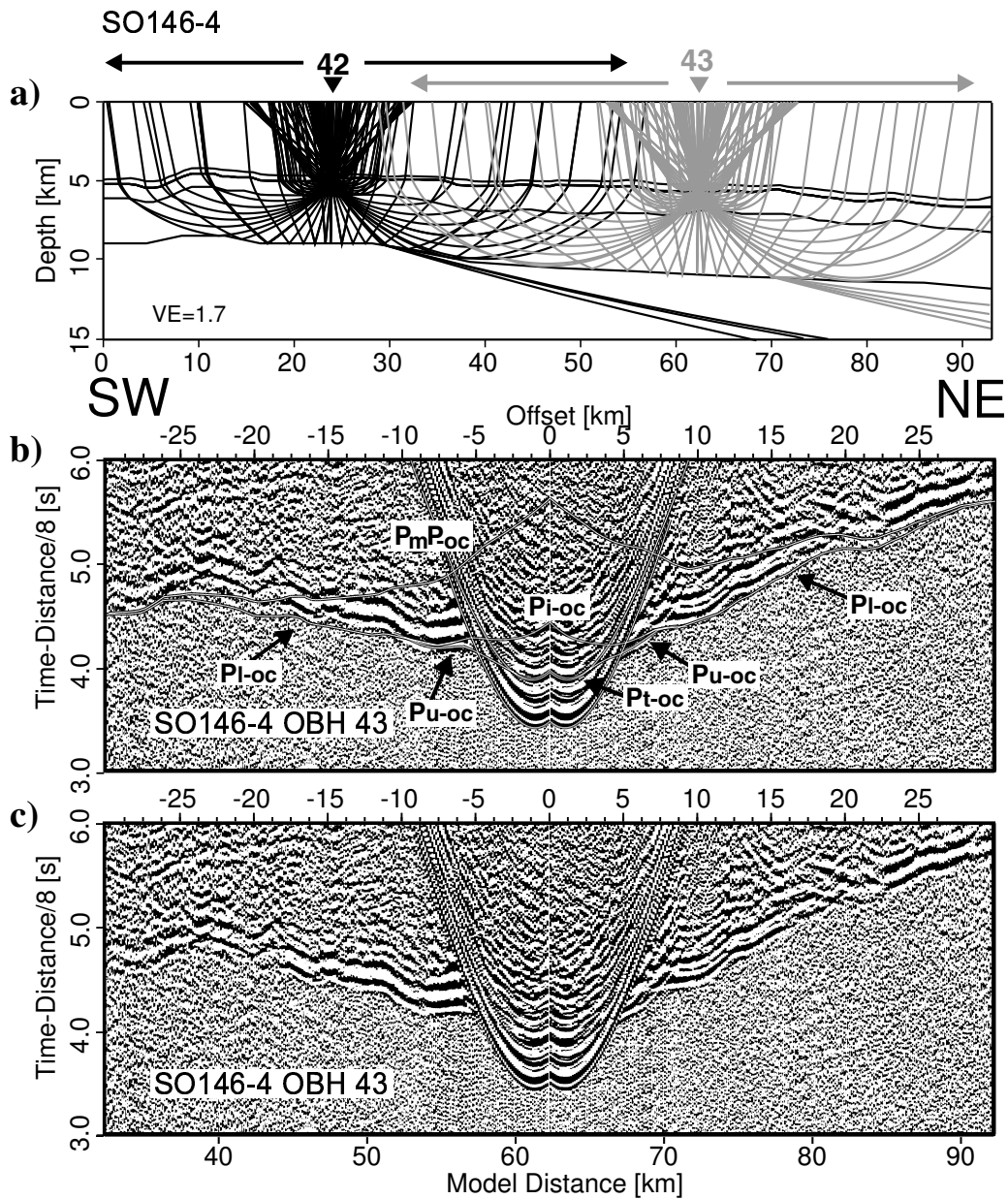


Figure 4.6: *Enlargement of the P-velocity model (a) for profile SO146-4/9°S shown with representative ray paths calculated for the seismic sections below and Figure 4.5. The regions covered by the enlargement of the seismic sections are marked above the model. Enlargements of record section OBH 42 and OBH 43 (Fig. 4.5) for comparison of the oceanic crustal thickness along the profile (c) are overlain with traveltime curves (b). See Figures 3.3 and 3.4 for details and definitions of abbreviations.*

### The oceanic Nazca plate in a global, geologic context

The refraction models, obtained by modeling the new seismic refraction data, reveal a 'normal' oceanic crustal composition for the Nazca plate, covered by a thin pelagic sediment layer [Grevenmeyer *et al.*, 1999; Walther, 2003]. Along the oceanic part of each GEOPECO profile representative locations were selected to show the characteristics of the oceanic crust in the study area, locations are indicated by white dashed lines ① – ⑦ in Figure 4.4.

The compilation of the velocity-depth distribution of the oceanic crust across the Peruvian margin, obtained from this study [see also Krabbenhöft *et al.*, 2004], is given in Figure 4.7. The left part of the figure includes the water depth and sediment thickness information. The right side only contains the oceanic crustal and upper mantle velocity distribution for a better comparison of the crustal structure. The velocity-depth sections in Figure 4.7 are located at profile km 20 (curve ①, Fig. 4.7), where the oceanic crust is thin, and km 68 (curve ②, Fig. 4.7) at profile SO146-4/9°S. Locations of the velocity-depth sections along profile SO146-5/12°S are at profile km 22, km 50, where the oceanic crust outcrops, and km 62 (curves ③, ④, ⑤, Fig. 4.7, respectively). The velocity-depth sections of profile SO146-3/14°S are located at profile km 22 and km 50 (curves ⑥, ⑦, Fig. 4.7). The water depth ranges between 4.5 km and 5.5 km, increasing towards the trench due to the bending of the lithosphere.

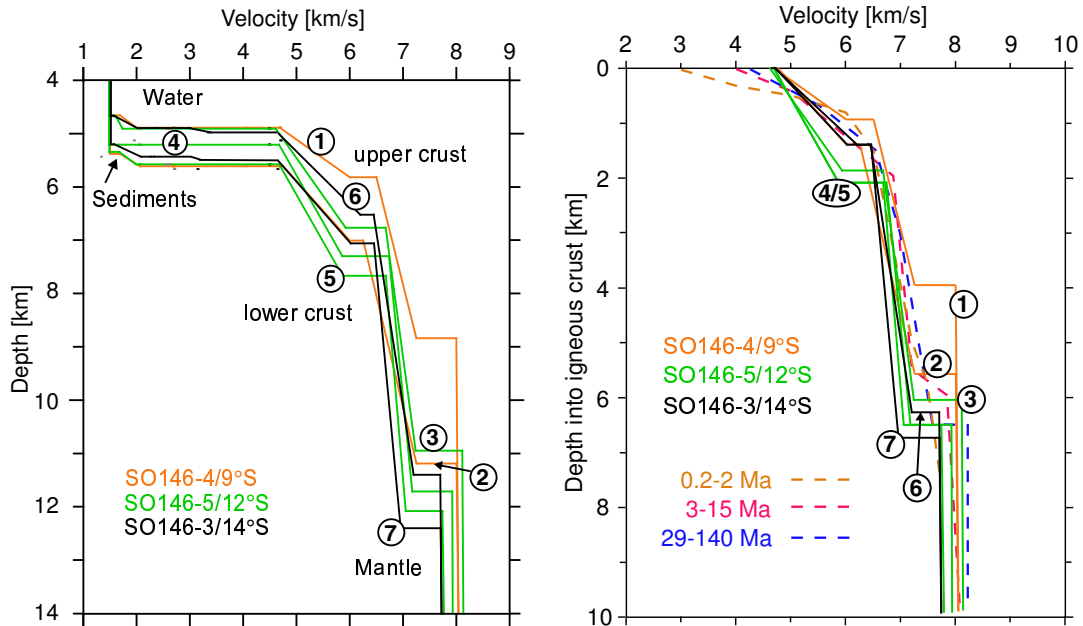


Figure 4.7: Seismic *P*-wave velocities at selected locations along the GEOPECO profiles (left, ① – ⑦, see Fig. 4.4 for locations) compared to the average oceanic crustal seismic velocities of the Pacific ocean (right, dashed lines are representative for 0.2–2, 3–15 and 29–140 Ma-old-crust, compiled by White *et al.* [1992]).



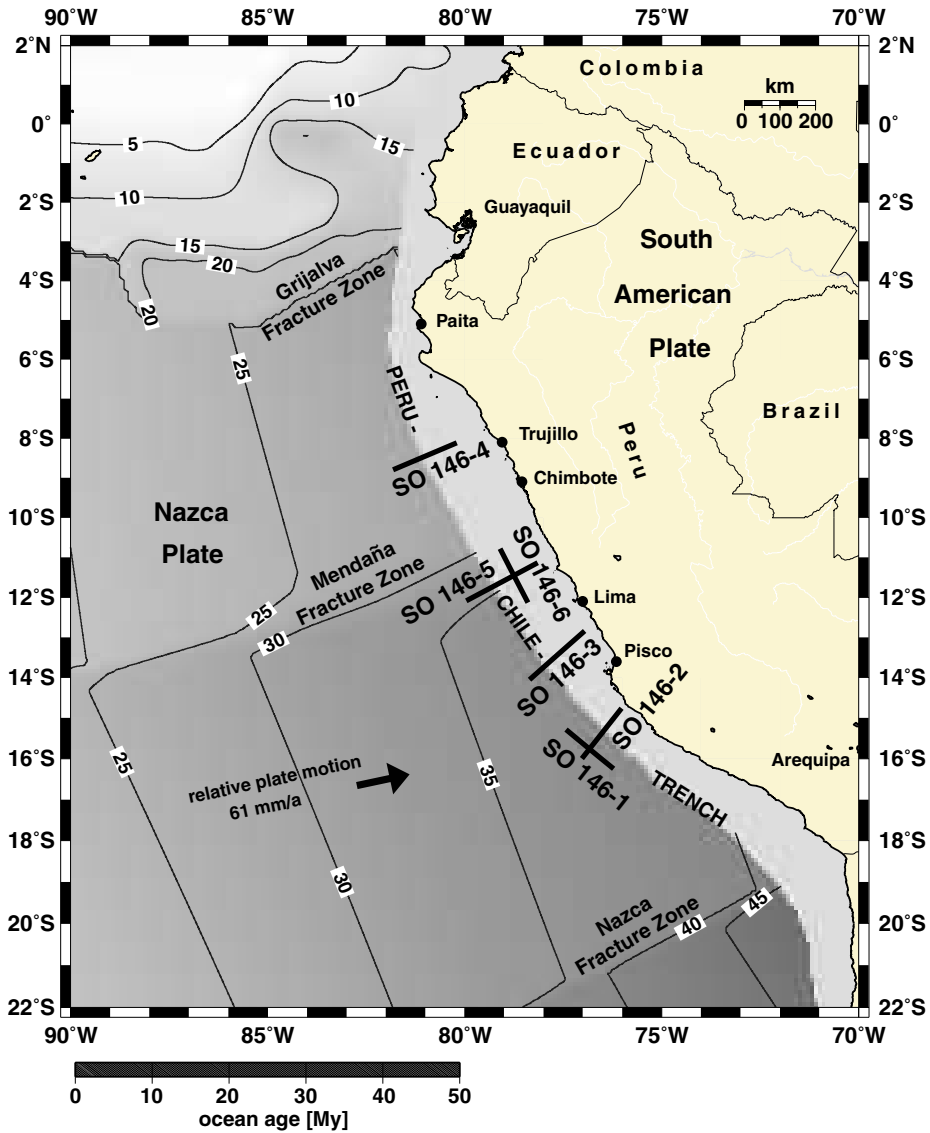


Figure 4.8: Overview of the Peruvian margin showing the oceanic crustal age of the Nazca plate, note the greyshaded scale below. The ages are notated at 5 Ma isolines and the locations of the GEOPECO profiles are shown. Crustal ages are from Müller *et al.* [1997].

The thickness of the pelagic sediment layer is variable: Sporadically the sediment layer is lacking, e.g., on profile SO146-5/12°S, where the oceanic crust outcrops, whereas the maximum Layer-1-thickness across the profile is  $\sim 200$  m (Figs. 4.4, 4.7 left). The oceanic crustal velocity-depth sections of this study comply with the curve of 29–140 Ma old oceanic crust of the compilation for different crustal ages for the Pacific ocean by White *et al.* [1992] (Fig. 4.7, right). The crustal age of the oceanic Nazca plate offshore Peru at the trench axis varies between 28 Ma and 38 Ma with a sudden jump

across the Mendaña Fracture Zone (Fig. 4.8). The only 4-km-thick oceanic crust in the area of Trujillo Trough, compared to an average oceanic crustal thickness of 6.4 km in the study area, is attributed to the extensional regime (compare curve ① to the other curves, Fig. 4.7, right). It has been known for some decades from seismic experiments that the crust beneath fracture zones is generally thinner than 'normal' crust [White *et al.*, 1992], which is observed here on profile SO146-4/9°S (①, Fig. 4.7, right). The entire crustal thickness of profile SO146-4/9°S is about 0.5–1 km thinner than the crust of the profiles south of Mendaña Fracture Zone (SO146-5/12°S (③, ④, ⑤) and SO146-3/14°S (⑥, ⑦), Fig. 4.7, right). This may be explained, in addition to the extensional regime in the region of Trujillo Trough, by the higher crustal age in the south. Oceanic crustal thickening with age has been observed in the Pacific ocean by, e.g., Le Pichon *et al.* [1965]; Goslin *et al.* [1972]; Christensen and Salisbury [1975]. Across all profiles, the upper oceanic crustal velocity (of Layer 2) increases from about 4.5 km/s to 6.5 km/s. This relatively large velocity gradient of the upper 1.5–2 km of oceanic crust reflects the variability in degree of fracturing, porosity and weathering, which causes the low velocities in the upper crust [Whitmarsh, 1978]. The lower crust (Layer 3) with velocities from about 6.5 km/s at the top, and 7.2 km/s at the base, exhibits far less scatter in velocities and much smaller velocity gradients than the upper oceanic crust. The velocity of the lower crust increases smoothly with depth as a result of the increasing pressure [White *et al.*, 1992].

## 4.2 The trench across the Peruvian margin

The trench axis is about 6 km deep. There is very little sediment fill visible on all three refraction dip lines, which is consistent with the overall thin sedimentary layer on top of the oceanic Nazca plate. The trench fill consists of turbidites [Kulm *et al.*, 1981]. With 0.5 km it is slightly thicker at the northernmost profile SO146-4/9°S than on line SO146-5/12°S, with only 0.2 km of trench fill (Fig. 4.4). The trench fill on the southern profile is 0.3 km thick. Before interpreting the two-dimensional velocity models obtained by forward modeling with regard to the structure at the toe of the margin, some considerations about definitions and the applicability of the critical margin wedge model are discussed.

### 4.2.1 The critical taper - the Coulomb theory - a stable wedge

The structure of a collisional margin wedge is dependent on the stresses acting upon it [e.g., Davis *et al.*, 1983; Dahlen *et al.*, 1984]. Despite the great variety in fold-and-thrust belts and accretionary wedges, their cross sections exhibit several common properties. To be concordant with the common literature [e.g., Davis *et al.*, 1983; Dahlen *et al.*, 1984], the term of the accretionary wedge is used in this section for the toe of the margin, consisting of sediments at accretionary as well as erosive margin settings.

The main structural features of fold-and-thrust belts and accretionary wedges are folds of various sizes, thrust faults, a basal detachment surface (or décollement), often out-of-sequence thrusting, and a characteristic wedge shape. Analyzing the geometry and the above characteristics, yields information on the stability of the margin wedge. Early works of Elliott [1976] and Chapple [1978] on fold-and-thrust belts (e.g., western Taiwan [Davis *et al.*, 1983]) and accretionary wedges (e.g., Cascadia [Hyndman *et al.*, 1990]) illustrate the mechanics of these natural wedges with a wedge, that forms in front of a bulldozer or plow, moving with a velocity  $v$  (Fig. 4.9). A critical wedge, by definition, is one at the verge of shear failure everywhere under horizontal compression [e.g., Davis *et al.*, 1983; Dahlen *et al.*, 1984]. At a convergent margin, an accretionary wedge forms, while being compressed and deformed, as the wedge slides along its rigid weak base. The sediments on top of the subducting plate may act as rigid base.

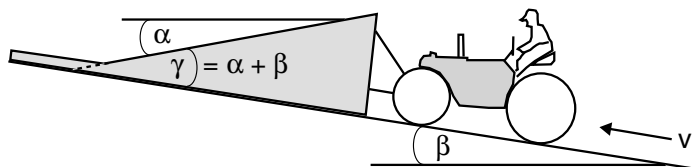


Figure 4.9: *Schematic diagram illustrating the mechanics of a subaerial wedge analogous to the mechanics of the wedge in front of a bulldozer or snow plow (after Davis *et al.* [1983]).*

Shortening and thickening of the wedge material occurs, until the critical taper is attained, after which the wedge material slides stably. Deformation of the wedge occurs as long as the taper is smaller than the critical taper, which is then defined as under-critical taper. The wedge slides stably without deforming, if the taper is larger than the critical taper, and it will be mainly affected by collapsing and erosion [e.g., *Davis et al., 1983; Dahlen et al., 1984*].

The critical taper is influenced by the material properties of the margin (the upper and lower plate), e.g., the roughness of the subducting plate. Hence, the critical taper changes when ridge or seamount subduction occurs [*Lallemand et al., 1994*]. The taper of the margin wedge is given by  $\gamma = \alpha + \beta$  (see Fig. 4.9), where  $\alpha$  is the angle of a horizontal line with the surface slope, and  $\beta$  the dip angle of the subducting plate with a horizontal line. The Coulomb theory (equations are given in appendix A) is used to calculate the stability field of a margin wedge. The rock is treated as a frictional plastic material (Coulomb type) without cohesion. The non-cohesive critical taper model is a reasonably good approximation for many geological applications. Submarine margin wedges are such settings, where the non-cohesive Coulomb model can be applied to. The mechanics of a margin wedge are dependent on different parameters. The internal friction  $\mu$  affects the degree of deformation within the margin wedge. The internal friction increases with increasing lithification, compaction, and cementation of the margin wedge material [e.g., *Davis et al., 1983*]. The basal friction  $\mu_b$ , which varies laterally across a margin with changing material properties across the plate boundary (e.g., roughness of the subducting oceanic plate), also depends on the pressure in the pore fluids across the margin. Hydrostatic pressure typically occurs at the toe of the margin wedge, whereas overpressuring of pore fluids typically increases with greater depths and greater distance from the trench axis at the base of the margin wedge [e.g., *Dahlen et al., 1984*].

### Application of the non-cohesive Coulomb theory

The exact critical taper equation for a homogeneous non-cohesive Coulomb wedge is given by [e.g., *Davis et al., 1983*]:

$$\alpha + \beta = \Psi_b - \Psi_0 \quad (4.1)$$

The solution is applicable to an active fold-and-thrust belt or convergent margin wedge by choosing both  $\Psi_b$  and  $\Psi_0$  to be positive acute angles. Figure 4.10 illustrates the angles, forces and parameters, forming at and affecting a margin wedge [*Davis et al., 1983*].  $\Psi_b$  and  $\Psi_0$  are the angles of the maximum compressive stress  $\sigma_1$  at the base of the wedge and at the seafloor, respectively. In a Coulomb wedge, the orientation of  $\sigma_1$  is everywhere the same ( $\Psi_0 = \text{constant}$ ). Variables  $\phi$  and  $\phi_b$  are the internal and basal friction angles. They are related to the internal and basal friction coefficients:  $\mu = \tan\phi$  and  $\mu_b = \tan\phi_b$ , respectively.

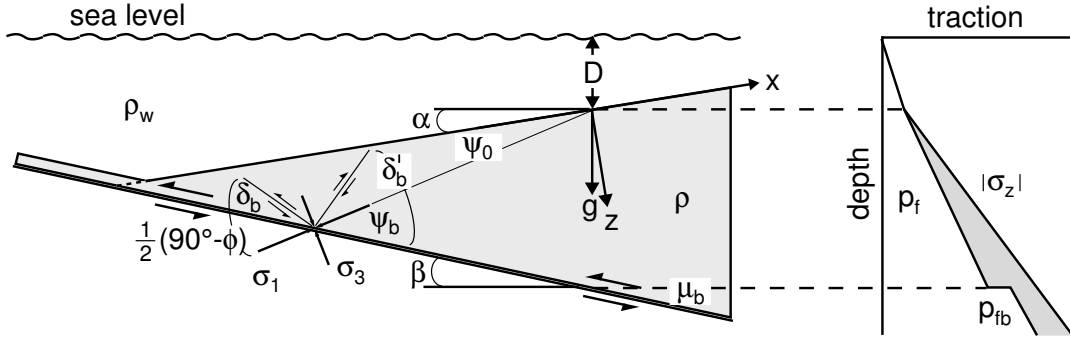


Figure 4.10: Schematic diagram of a submarine wedge, which is under horizontal compression on the verge of Coulomb failure throughout (after [Davis et al. \[1983\]](#)), showing forward-verging and backthrusts. The geometry is given in Cartesian coordinates  $x$ ,  $z$  and the angles  $\alpha$ ,  $\beta$ ,  $\Psi_b$ ,  $\Psi_0$ ,  $\delta_b$ ,  $\delta'_b$ , and  $\phi$ . The strength in the wedge is proportional to the effective stress  $\sigma_z$  (shaded area on the right).

Variables  $\lambda$  and  $\lambda_b$  (not shown in Fig. 4.10) are the internal and basal pore fluid pressure ratios corresponding to  $(P_f - P_{seafloor})/(\sigma_z - P_{seafloor})$ ;  $P_f$  is the pore fluid pressure and  $\sigma_z$  is the lithostatic pressure along an axis normal to the seafloor. Variables  $\rho_w$  and  $\rho$  are the densities of the water and the rocks, respectively. In the following, the effective basal friction coefficient  $\mu_b^*$ , which can be measured directly, is given instead of  $\mu_b$ . The relation of the effective basal friction coefficient to the basal friction coefficient is given by:  $\mu_b^* = \mu_b(1 - \lambda_b)/(1 - \lambda)$ .

Laboratory experiments yield values for the internal friction coefficient  $\mu = 0.6 - 1.0$  for virtually all rocks. The corresponding internal friction angles are  $\phi = 3 - 45^\circ$ . Cohesion  $S$  varies from  $\sim 0 - 150$  MPa with strong dependence on porosity, cementation, mineralogy, and other factors [[Dahlen, 1990](#)]. Shale and sandstone, typical constituents in margin wedges, usually have values of  $S = 5 - 10$  MPa [[Hoshino et al., 1972](#)]. These low values play a minor role in the mechanics of fold-and-thrust belts and accretionary wedges, consequently the cohesion is not accounted for. Cohesion is also of little account in the case of frictional sliding on pre-existing faults. [Byerlee \[1978\]](#) showed with laboratory experiments, that the friction coefficient is remarkably uniform for a variety of rock types, with  $\tau = -0.85\sigma_n^*$  for  $\sigma_n^* < 200$  MPa, where  $\sigma_n^*$  is the effective normal traction. Therefore, the assumption is appropriate, to treat the fold-and-thrust belt and accretionary wedge rock as Coulomb material, which is governed by e.g., brittle fracture [[Paterson, 1978](#)] or frictional sliding [[Byerlee, 1978](#)].

[Lallemand et al. \[1994\]](#) compiled the characteristic parameters of Coulomb critical wedges from different studies, which are used to illustrate the Coulomb theory and mechanics of convergent margin wedges. Plotting  $\alpha$  against  $\beta$  yields the graphical description of the stability field of a convergent margin. The values of Table 4.1 are summarized in the stability field diagram in Figure 4.11 (right). They are from well data measured in frontal wedges from different margins (e.g., the accretionary Oregon

## 4.2. THE TRENCH ACROSS THE PERUVIAN MARGIN

---

margin) [*Lallemand et al., 1994*]. The values for  $\mu$  and  $\mu_b^*$  were calculated from structural considerations of conjugate thrust faults at the toe of the wedge for Nankai, and Oregon by *Lallemand et al. [1994]* using the method of *Davis and von Huene [1987]*, who calculated the values for the Aleutian margin.

The magnitude of the critical taper is governed by the relative magnitudes of the frictional resistance along the base and the compressive strength of the wedge material: An increase in sliding resistance results in the increase in critical taper, since the drag on the base is fundamentally responsible for the deformation. An increase in wedge strength results in the decrease of the critical taper, since a stronger wedge can be thinner and still slide stably over a rough base without deforming. Variation of the pore fluid pressure ratio  $\lambda$  has the greatest impact on the stability of the margin wedge, while comparing the error estimation (Fig. 4.11, right) of the mean values of the internal and effective basal friction coefficient  $\mu$  and  $\mu_b^*$ , and the pore fluid pressure ratio  $\lambda$ .

Measured Values	$\mu$	$\mu_b^*$	$\lambda$
Taiwan	-	-	$0.675 \pm 0.05$
Aleutian	$0.45 \pm 0.09$	$0.28 \pm 0.07$	$\sim 0.87$
Nankai	$0.45 \pm 0.09$	$0.28 \pm 0.07$	-
Oregon	$0.45 \pm 0.09$	$0.28 \pm 0.07$	-
Barbados & Makran	-	-	$\sim 1$

Table 4.1: Values of the internal and the effective basal friction coefficient  $\mu$  and  $\mu_b^*$  as well as the pore fluid pressure ratio  $\lambda$ , measured from well data.

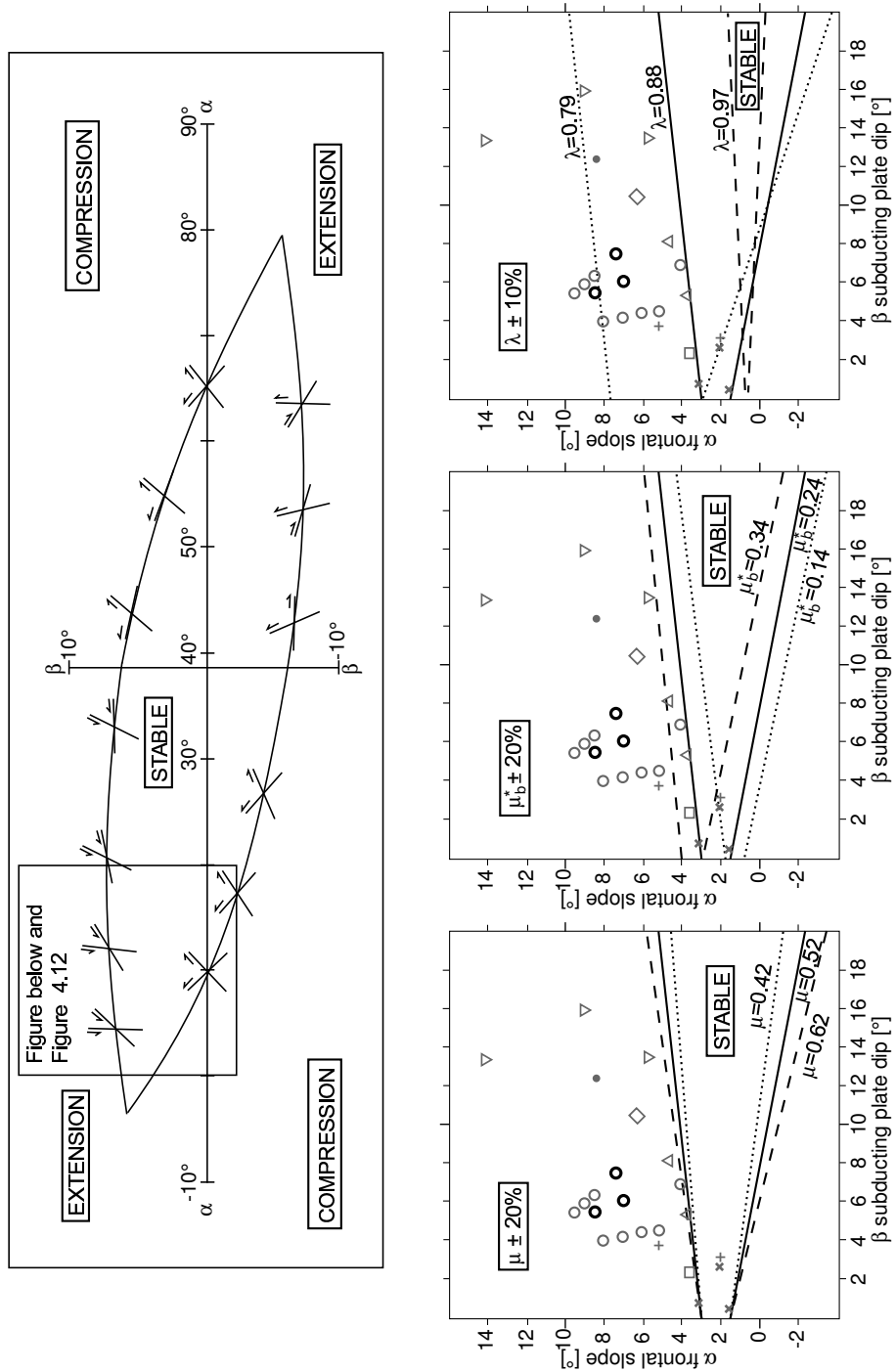


Figure 4.11: Stability field for critical wedges using mean measured friction angles and pore fluid pressure ratio, e.g.,  $\mu = 0.52$ ,  $\mu_b^* = 0.24$ , and  $\lambda = 0.88$ ,  $\rho_w = 1030 \text{ kg/m}^3$ , and  $\rho = 2300 \text{ kg/m}^3$  (mean density for a wedge thickness of 0–10 km). The box (left) outlines realistic taper values for natural wedges. The graphical error estimation for  $\mu$ ,  $\mu_b^*$ , and  $\lambda$  is plotted on the right. The triangles/circles/squares/crosses mark values of measured wedge tapers (for details see Figure 4.13).

### 4.2.2 The critical taper applied to the toe of the Peruvian margin

The Peruvian margin wedge complies with the requirements for non-cohesive Coulomb material as described in the section above. Therefore, the critical Coulomb theory is applicable to the convergent margin.

The taper of the Peruvian margin is obtained directly by measuring the angles of the surface slope,  $\alpha$ , and the dip angle of the subducting plate,  $\beta$ , from the velocity models obtained by forward modeling (Fig. 4.12). The surface slope is steep along all three transects with  $\alpha = 7.5^\circ$  for SO146-4/9°S,  $\alpha = 8.5^\circ$  for SO146-5/12°S and  $\alpha = 7^\circ$  for SO146-3/14°S. The dip angle of the subducting plate is  $\beta = 7^\circ$  for the northern profile and the two profiles south of Mendaña Fracture Zone have similar values with  $\beta = 5.5^\circ$  for SO146-5/12°S and  $\beta = 6^\circ$  for SO146-3/14°S. The above values result in a taper of  $\gamma = 12^\circ$  on profile SO146-3/14°S increasing towards the north with a value of  $13^\circ$  for line SO146-5 and  $\gamma = 14.5^\circ$  for the northernmost profile [Krabbenhöft *et al.*, 2004]. Hampel *et al.* [2004] obtained values for the refraction profile SO146-2/15°S across the subducting Nazca Ridge. There, the surface slope angle is  $\alpha = 9.5^\circ$  and the dip angle of the subducting oceanic plate is also very high with  $\beta = 9^\circ$ . Hence, the resulting taper is largest across the Peruvian margin at the location of current ridge subduction, with  $\gamma = 18.5^\circ$ .

The taper values were used to compare the Peruvian margin with a global evaluation of the stability field of the margin compiled by *Lallemand et al.* [1994]. The values for a stable wedge are delimited by the minimum and maximum critical taper (Fig. 4.13), which are governed by the internal and the effective basal friction coefficient  $\mu$  and  $\mu_b^*$  as well as the pore fluid pressure ratio  $\lambda$ . Here the minimum and maximum critical taper for a stable wedge is derived from global mean values for  $\mu = 0.52$ ,  $\mu_b^* = 0.24$  and  $\lambda = 0.88$ , the internal and effective basal friction and pore fluid pressure ratio, respectively (see section above) [Lallemand *et al.*, 1994]. The critical taper derived from all refraction models of this study (SO146-3/14°S, SO146-4/9°S, and SO146-5/12°S) supplements the taper for Peru derived from earlier studies, gray circles in Figure 4.13, modified after *Lallemand et al.* [1994] (HIG- and CDP-lines, see Figure 1.3 for locations). The relatively high taper values, with only little variation across the Peruvian margin, are consistent with an erosive regime. The taper at the Peruvian margin north of 14°S is smaller than the one for the profile where the Nazca Ridge currently subducts (SO146-2/15°S [Hampel *et al.*, 2004]). The highest taper value offshore Peru at SO146-2/15°S almost lines up with the values of the highly erosive Chilean margin, and the Tonga region (Fig. 4.13). Across the overall erosive Peruvian margin, enhanced erosion occurs due to the ridge subduction at the present Nazca Ridge collision zone.



4. RESULTS AND DISCUSSION OF THE REFRACTION DATA

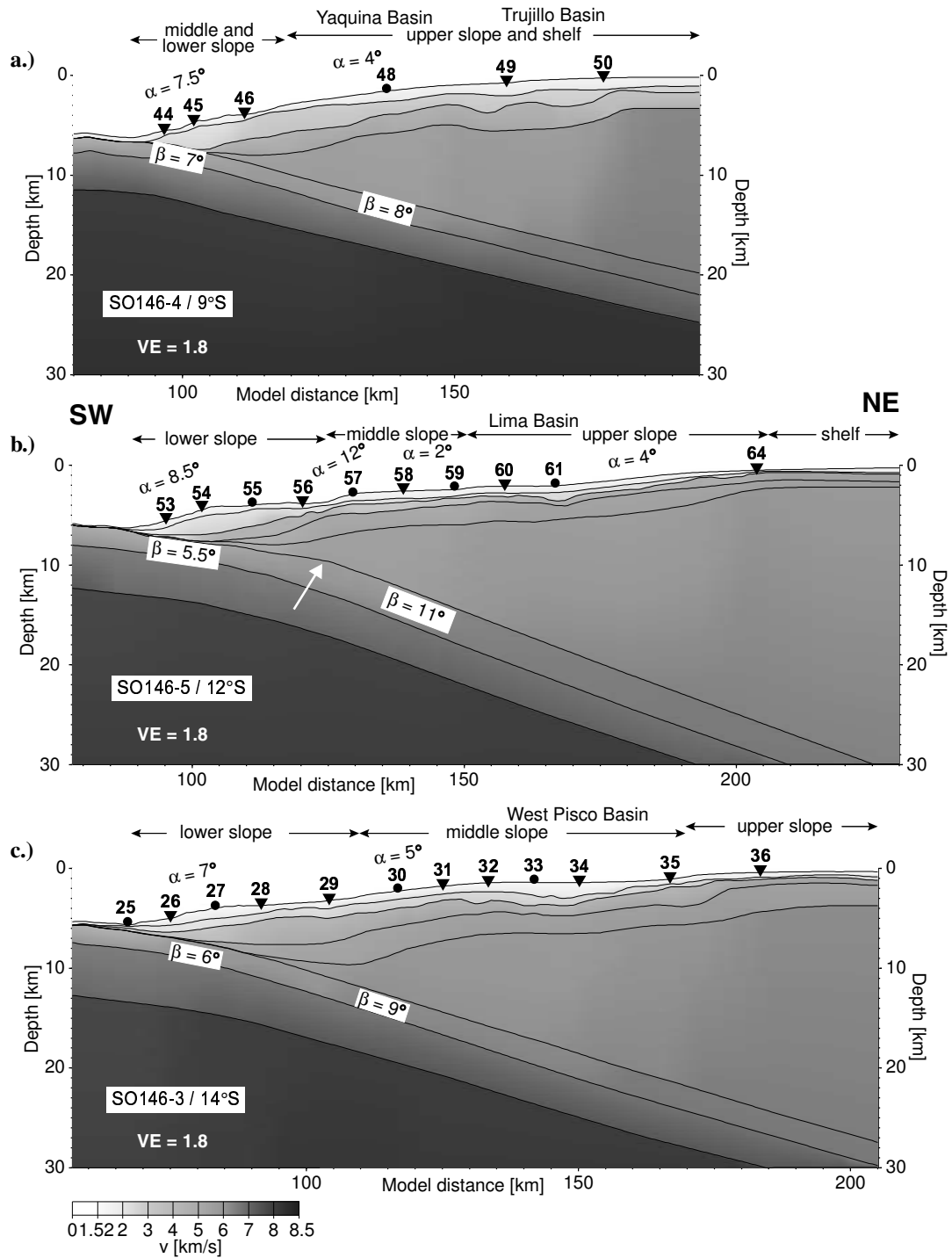


Figure 4.12: The taper ( $\alpha+\beta$ ) across the Peruvian margin from the velocity-depth models. The increasing taper landward of the trench reveals the higher strength of the continental basement compared to the frontal prism. Increased erosion is suspected where the white arrow points at. There the change in slope of the subducting slab is most distinct across the Peruvian margin. Note the values of the seismic P-wave velocities in the scale below. Locations of the OBH/OBS stations are marked by triangles/circles.

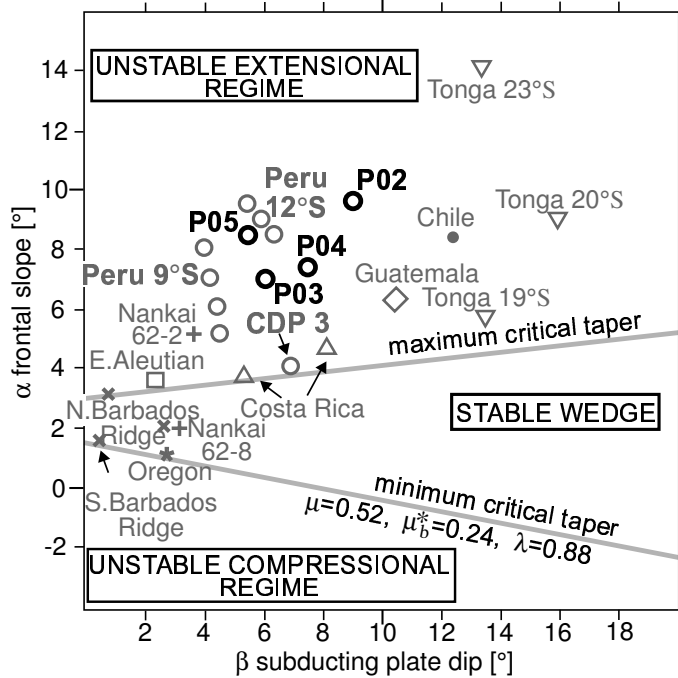


Figure 4.13: *Wedge taper analysis modified after Lallemand et al. [1994] with  $\mu = 0.52$ ,  $\mu_b^* = 0.24$  and  $\lambda = 0.88$ . Accretionary wedges like Barbados, highly erosive margins, e.g., Tonga and northern Chile, and erosive margins, but with a small frontal prism, like Japan and Peru. The wedge tapers, obtained from the refraction models of this study, are designated P03–P05, P02 is from Hampel et al. [2004], the residual Peru tapers are from von Huene et al. [1996].*

Simultaneously with the very large taper at the present collision zone of the Nazca Ridge with the South American plate, there is no frontal prism present [Hampel et al., 2004]. The Peruvian margin is dominated by erosional subduction mechanisms, which are increased along SO146-2/15°S as a consequence of the Nazca Ridge subduction [Hampel et al., 2004].

### 4.3 The continental slope and shelf structure

The seismic P-wave velocities obtained from forward modeling are characterized by different vertical and lateral gradients across the continental slope of the entire Peruvian forearc. The upper two layers consist of sediments with velocities from 1.6–2.0 km/s (Fig. 4.4) and velocities from 2.1–3.3 km/s, increasing from the trench landwards. These are consistent with modeling the traveltimes of the seismic refraction phases  $P_s$  and  $P_1$  as denoted in Figures 3.4, 3.6, and 3.8.

#### 4.3.1 The lower slope

The frontal prism is identified in the coincident MCS line CDP-1 by the typical forward verging thrusts (Fig. 2.4). The prism is made up of sedimentary deposits added to the toe of the margin. This process, depending on the subduction mechanisms, is governed either by accretion (accretionary prism) or due to slope failure [von Huene and Scholl, 1991]. An increase in the seismic P-wave velocity across the frontal prism ( $v_p = 2.1$  underneath OBH 54 at profile km 100, Fig. 4.14) is directly linked to the change in the reflection pattern along the lower slope. Figure 4.14 shows the landward part of the refraction line SO146–5/12°S overlain with the line drawing interpretation of the coincident high resolution MCS data of von Huene and Suess [1988]. The landward verging thrust located at the landwardmost part of the margin toe that is interpreted in this MCS line drawing, complies with the local maximum in the seismic P-wave velocities across the steep lower slope (Figs. 2.4 and 4.14) [Krabbenhöft et al., 2004]. The landward verging thrusts border seabed-parallel sediment sequences further upslope, causing the change in reflection pattern. Directly seawards and landwards of this seismic P-wave velocity anomaly, their values decrease to 1.9–2.0 km/s. This P-wave velocity pattern within the frontal prism can be observed along the three refraction profiles SO146-3/14°S, -4/9°S and -5/12°S.

The trench turbidites at the Peruvian margin are redeposited from the continental plate due to slope failure. A small amount of trench fill is typical in non-accretive margins [Clift and Vannucchi, 2004]. The large taper, indicative of high basal friction [Kukowski et al., 1994], is further evidence consistent with the Peruvian margin being erosive [Lallemand et al., 1994]. The volume of the frontal prism for all refraction profiles is defined by the low seismic velocities of the sediments (Figs. 4.4 and 4.14). The frontal prism volumes of this study are consistent with estimates of the frontal prism from earlier interpretations of reflection seismic data [Kulm et al., 1981; von Huene and Suess, 1988; von Huene et al., 1996], and are now verified along the entire Peruvian margin (Figs. 4.4, 4.15). The low seismic velocities indicate high porosities and low strength of the frontal prism material that may be explained by overpressured pore fluids in the accreted sediment [Lallemand et al., 1994]. The frontal prism along the Peruvian margin is small and consistently associated with the steep lower slope.

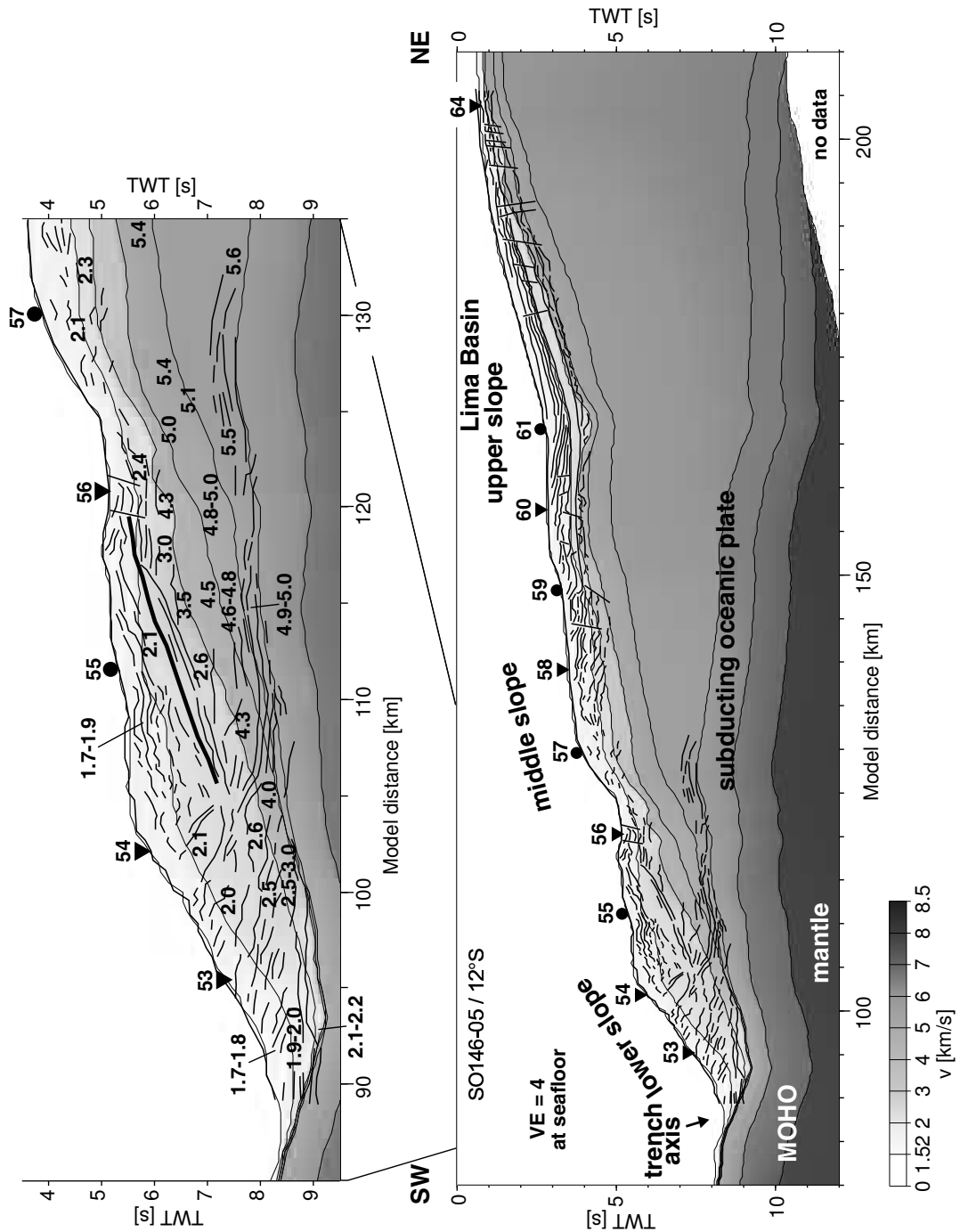


Figure 4.14: The landward part of the model of line SO146-5/12°S obtained from forward modeling. It is converted into a time-section and shows good correlation when compared with the line drawing of the time migration of the coincident high resolution seismic record CDP-1 shown in Figure 2.4 [von Huene and Suess, 1988]. Locations of the OBH/OBS stations are marked by triangles/circles. Seismic P-wave velocities are gray shade coded and annotated at the lower and middle slope.

#### 4. RESULTS AND DISCUSSION OF THE REFRACTION DATA

The width of the frontal prisms across the GEOPECO refraction lines is correlated with the steep lower slope from satellite derived bathymetry data [Sandwell and Smith, 1997]. The area occupied by the prism in between the refraction profiles is interpolated across the entire Peruvian margin and displayed in Figure 4.15. Its width north of the Mendaña Fracture Zone is 15 km. The prism of the central profile (SO146-5/12°S) is of the same size, whereas the frontal prism identified in the southern line extends laterally only to a width of 12 km. It is absent where Nazca Ridge currently subducts [Hampel et al., 2004]. The values for the width of the frontal prism across the entire Peruvian margin from this study are compared with some representative global values in Table 4.2, modified after the compilation by Clift and Vannucchi [2004]. The width of frontal prisms for Peru from 9°S to 14°S are in the upper region, when compared with other margins, only at Kamchatka the prism is also ~15 km wide.

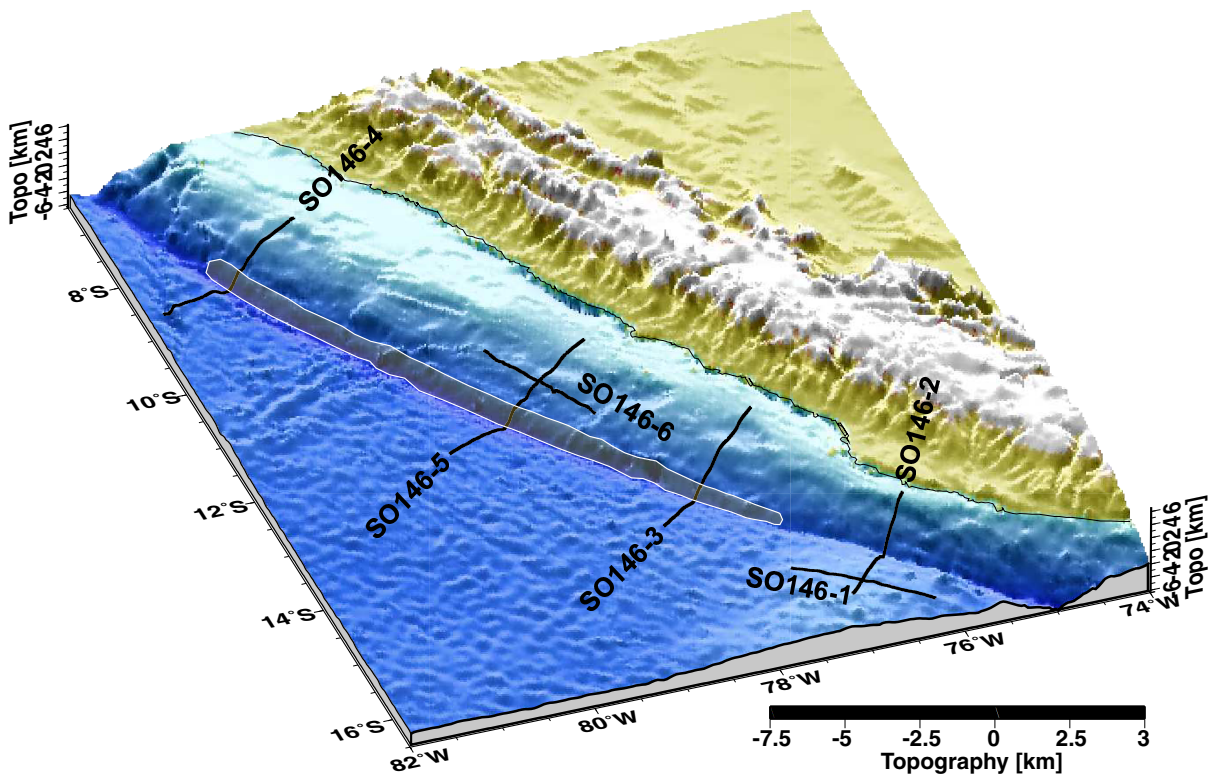


Figure 4.15: The frontal prism across the entire Peruvian margin is indicated by the white-framed shaded region across the lower slope. The extent of the prism is determined from the refraction lines across the GEOPECO profiles (see text for methodological details) and interpolated between the profiles taking into account for the associated steep lower slope from satellite derived bathymetry [Sandwell and Smith, 1997].

#### 4.3. THE CONTINENTAL SLOPE AND SHELF STRUCTURE

Frontal prisms - (erosive margins)	width [km]	convergence rate [km/my]	Trench sediment thickness [km]
Kamchatka 50°N	~ 15	80	0.8
Kurile 45°N	~ 10	85	0.3
Chile 32°S	~ 6	89	0.3
Kermadec / Tonga / Izu	no prism	67 / 110 / 90	0.2 / 0.3 / 0.3
Peru 9°S	~ 15	61	0.5
Peru 12°S	~ 15	61	0.2
Peru 14°S	~ 12	61	0.3
Peru 15°S	no prism	61	0.4
Accretionary prisms - (accretionary margins)			
Gulf of Alaska	~ 97	61	2.5
Aleutians 174°W	~ 80	62	1.5
Cascadia, Vancouver Island	~ 122	37	2.5
Nankai	> 124	38	2.3
Chile 45°S	> 124	20	3.2
Java 105°E	~ 175	76	1.3
Mediterranean 28°E	~ 170	20	8

Table 4.2: Values for the width of accretionary/frontal prisms from this study compared with a global compilation for different margin types, modified after *Clift and Vannucchi [2004]*. The values for Peru at 15°S are from *Hampel et al. [2004]*.

No frontal prism is found at the current Nazca Ridge collision zone at 15°S, as well as in the highly erosive Kermadec, Tonga and Izu subduction zones. The convergence rate across Peru is slightly lower than across the other erosive margins. The trench sediment thickness is similar to the ones at the erosive margins listed in Table 4.2. The accretionary convergent margins typically have much larger accretionary prisms, most of the ones listed in Table 4.2 are >100 km wide. The convergence rates are overall small and the trench thickness expectedly high. The maximum trench sediment fill is observed in the Mediterranean with 8 km. It is striking, that all the erosive margins listed here (and also in other literature, [e.g. *Lallemand et al., 1994*]), are located in the Pacific region.

In total, the volumes of the frontal prisms show values of 37 km<sup>3</sup> per trench km for profile SO146-4/9°S, 36.5 km<sup>3</sup> per trench km for profile SO146-5/12°S and 34 km<sup>3</sup> per trench km for profile SO146-3/14°S (Fig. 4.4). These values were calculated from the pixel information contained in the graphical display of the models (Fig. 4.16). The conditions across the frontal prism regions of all profiles are similar, e.g., no sediment overburden, similar thickness of frontal prism sediments, and similar seismic velocities. Therefore, no further assumptions concerning the porosities of the frontal prism sediments are included in this volume estimate.

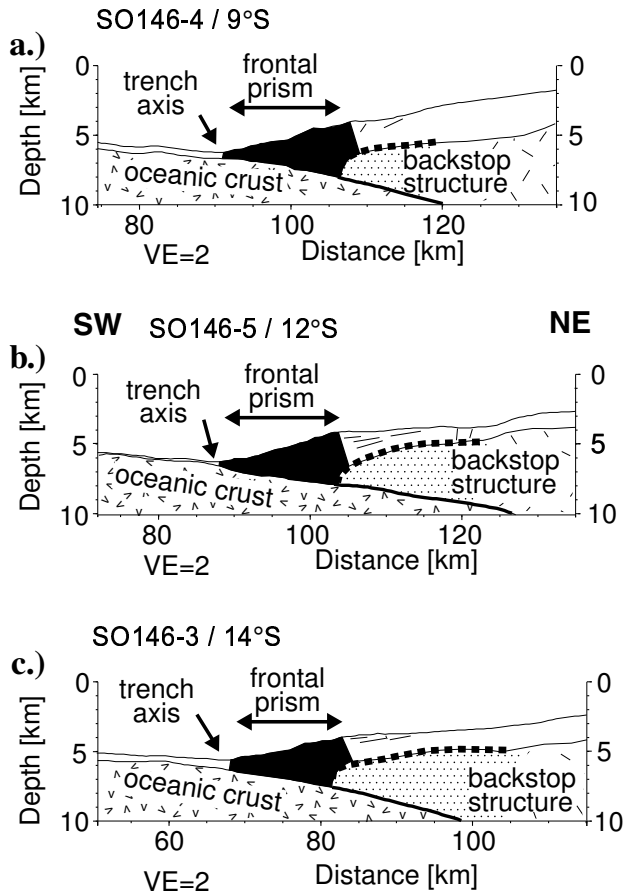


Figure 4.16: *Structural models with the region of the frontal prism from north to south. The seaward end of the frontal prisms is marked by the trench axis and its landward cessation is defined by the dip change of the reflectors and the backstop structure. The black area for all three profiles contains the pixel information for the calculation of the frontal prism volumes. The sedimentary prisms of the two northern profiles are about the same size with a width of 15 km ((a) and (b)), compared to the smaller (12 km wide) prism of profile SO146-3/14°S (c). See also Table 4.2.*

The small differences in size of the frontal prisms along the Peruvian lower slope may be explained by the influence of the southward migrating Nazca Ridge on subduction processes. The northern profile has not been affected by the subduction of the Nazca Ridge [Hampel, 2002]. Profile SO146-4/9°S is assumed to display a 'normal' stage of subduction at the typical long-term tectonically erosive Peruvian margin. Therefore, it is taken as reference for the comparison with the other refraction profiles across the Peruvian margin. The two southern profiles display different stages after the Nazca Ridge subduction took place at 11 Ma (the transect across Lima Basin, SO146-5/12°S) and at 6 Ma (the profile along West Pisco Basin, SO146-3/14°S) [Hampel, 2002]. During subduction of the Nazca Ridge, tectonic erosion dominates the subduction processes along the margin [Clift *et al.*, 2003], as observed at the present ridge collision zone at 15°S, with no frontal prism at the margin toe [Hampel *et al.*, 2004]. 6 my after Nazca Ridge subduction, a small frontal prism (12 km wide) has been re-established at the Peruvian margin at SO146-3/14°S. 11 my after the Nazca Ridge subduction, the frontal prism imaged at SO146-5/12°S is 15 km wide, and already completely re-developed, indicating the margin has returned to equilibrium after 11 my. This is inferred by the comparison of the width and volume of the frontal prism of profile SO146-4/9°S (both

are 15 km wide (Table 4.2), with similar volumes (Fig. 4.16)), which was never affected by Nazca Ridge subduction. A similar return of the margin to equilibrium has been witnessed also at the Alaska margin in the wake of the Yakutat Block collision [Fruehn *et al.*, 1999]. The frontal prisms at the Peruvian margin are of a typical size for an erosional type of margin (Table 4.2) (i.e., Japan, Tonga region) [von Huene and Scholl, 1991; Collot and Davy, 1998].

#### 4.3.2 The backstop region

The landward limit of the frontal prism is a backstop structure, which is defined here, by the increasing seismic velocities, related with higher material strength (Figs. 4.4 and 4.14). Increased landward vertical velocity gradients in the refraction models delimit the upper 3 km of the frontal prism. The shape of the backstop derived from the velocity-depth models across the Peruvian margin is between a type I and intermediate backstop structure, as defined by Byrne *et al.* [1993]. These backstop types are illustrated in Figure 4.17.

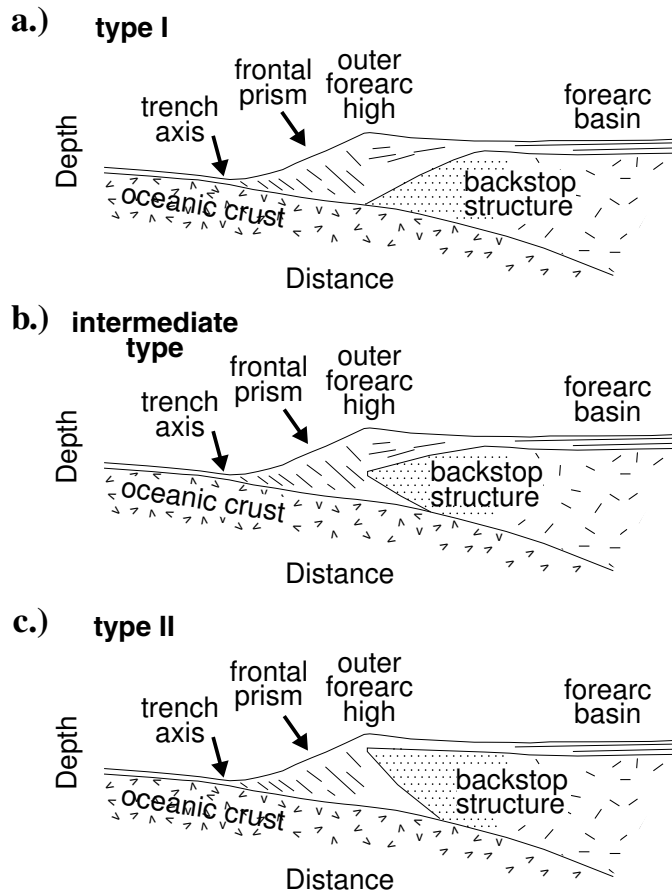


Figure 4.17: Schematic drawing showing the development of the outer forearc high at the position above the toe of the backstop for all the different backstop types. (a) type I, (b) intermediate type, and (c) type II (after [Byrne *et al.*, 1993]).



Above the sufficiently strong backstop a bathymetric high has developed, indicating an increase in internal material strength within the margin [Wang and Davis, 1996]. Numerical and sandbox modeling on the mechanical role of backstops show, that the position of the outer high is located above the toe of the backstop structure independent of the backstop type [e.g., von Huene and Suess, 1988; Byrne et al., 1993; Wang and Davis, 1996] (see Fig. 4.17). This is consistent with the interpretation in terms of the structure derived from the GEOPECO velocity-depth models. The shape and location of the backstop structure is constrained by the change to a chaotic reflection pattern in seismic MCS data as reported by von Huene and Suess [1988] in profile SO146-5/12°S. This chaotic reflection pattern is represented by a lack of continuous reflections in the line drawing in Figure 4.14. From commercial drill holes at 9°S it is known that the continental crust of the Peruvian forearc consists of foliated metamorphic rocks of Paleozoic or Precambrian age [Kulm et al., 1981]. However, drilling information is insufficient to define its seaward limit. The seaward limit of the continental basement in this study is defined by decreasing seismic velocities ( $v_p = 3.5\text{--}5.0$  km/s).

As the Peruvian margin is dominated by long-term erosional processes [von Huene and Suess, 1988; von Huene and Scholl, 1991; Pecher et al., 1996; Clift et al., 2003], the seaward part of the backstop may not be an ancient, consolidated accretionary prism, but is likely to be composed of (crystalline) continental crust along all three refraction lines. In the region drilled during ODP Leg 112 the middle Eocene section was drilled at SO146-5/12°S, at depths of 600 m and 400 m (at sites 688 and 682, Fig. 1.3) below the seafloor along the lower and the middle slope [von Huene and Suess, 1988]. This implies that the backstop across the Peruvian margin is composed of crystalline rock. The lower seismic P-wave velocities of the backstop structure compared to the crystalline basement beneath the forearc basins (from  $v_p = 3.5\text{--}5$  km/s to  $v_p = 5\text{--}6$  km/s, Figs. 4.4 and 4.14), consequently indicate a difference not in rock composition, but in internal structure (e.g., by cracks altered crystalline basement). This might be due to stronger coupling between the subducting and overriding plates underneath the backstop, resulting in fractures and cracks within the margin wedge material. This complies with high resolution seismic studies, which indicate fluid migration through fractures and due to anisotropic permeability across the lower slope along the northernmost profile SO146-4/9°S [Hübscher and Kukowski, 2003] and the central profile SO146-5/12°S [Pecher et al., 2001].

The similarities of the backstop structure across the entire Peruvian margin, e.g. the same shape between type I and intermediate backstop type on all three refraction models, indicate the same mechanical role of the backstop across the margin. Therefore, the cause for the structural difference of the outer highs on the three refraction profiles are explained by differences in the coupling between the subducting and the overriding plate [Davis, 1996]. The outer high along the transect at SO146-5/12°S is most distinct due to strong coupling, which produces extremely intense deformation at the toe of the backstop, leading to a high and narrow uplift [Byrne et al., 1993]. This is constrained by the change in reflection pattern (landward dipping to seafloor parallel) underneath

OBH station 54 (Fig. 4.14). Weaker basal coupling produces a wider outer high, like the topographic structures seen along the slopes of the northern- and southernmost GEOPECO profiles, indicating reduced strength of the backstop.

#### 4.3.3 The forearc region

##### General structure of the continental slope across Peru

The structure of the continental basement causes the overlying sediments to pond against a well-developed outer high in front of a forearc basin [Davis, 1996]. The forearc basins across the Peruvian margin are the Yaquina Basin located at the northernmost slope, which connects with the upper-slope Trujillo Basin, both at 9°S, Lima Basin across the middle at 12°S, and West Pisco Basin at the southernmost profile at 14°S. Yaquina Basin, a 3-km-thick forearc basin on the northernmost transect, displays velocities of 1.7–3.0 km/s within the sedimentary fill (Fig. 4.4a). Immediately landwards, Trujillo Basin shows the same thickness and seismic P-wave velocities (Fig. 4.4b). These values correspond to post-Eocene sediments, the uppermost part composed of Neogene slope sediments, which are known from commercial drill holes Delfin and Ballena located on the forearc 80 km further south [Kulm *et al.*, 1981] (see Fig. 1.3 for location). ODP Leg 112 revealed that the sedimentary sequences in Lima Basin are early Eocene-Quaternary sediments [von Huene and Suess, 1988] (see Fig. 1.3 for location). Along refraction line SO146-5/12°S their thickness is 1.0–1.5 km with velocities of 1.7–2.7 km/s. These values agree with the borehole data. Seismic velocities in West Pisco Basin across the southernmost transect at 14°S range from 1.6–2.7 km/s with a total thickness of 2 km (Fig. 4.4c).

The basins along the northern transect, which were not affected by Nazca Ridge subduction [Hampel, 2002], reveal slightly higher seismic velocities and are almost twice as thick as Lima and West Pisco Basins, which in contrast are affected by Nazca Ridge subduction [Hampel, 2002]. The sedimentary units along the upper slope in Lima Basin are cut by normal faults (Figs. 2.3b and 4.14) indicating extension. The boundary between the second and third layer delimits the top of the crystalline basement for all refraction profiles of this study. This interface is consistent with the traveltimes of the seismic refraction phases  $P_3$  as labeled in the models, Figures 3.4, 3.6, and 3.8. The top of the crystalline basement coincides with the cessation of reflection patterns with depth across the upper slope in the Lima Basin, as shown in the line drawing in Figure 4.14. The refraction models reveal velocities of 4.5–6.5 km/s for the continental crust. The upper velocity value of the continental crust is constrained by the ray coverage down to a depth of 25 km. The deepest boundary within the overriding continental plate marks a change in the velocity gradient within the crystalline basement, which is consistent with modeling of the seismic arrivals (designated  $P_4$ , Figs. 3.6 and 3.8).

**The oceanic/continental interface beneath the Peruvian forearc**

The interface between the overriding continental plate and the subducting Nazca plate is well constrained from the  $P_{t-oc}$  reflection (e.g., Fig. 3.1). Across the seaward part of the forearc, low seismic P-wave velocities ( $\sim 4.1 - 4.5$  km/s, Fig. 4.4) were modeled in the backstop region. The low P-wave velocities across the seaward part of the backstop region (resistive buttress of consolidated sediment and/or rock of the upper plate [von Huene and Scholl, 1991]; dashed lines, Fig. 4.4) indicate low seismic velocities above the plate boundary within this region.

The seismic reflections from the top of the oceanic crust under the backstop region hold high amplitudes, e.g., OBH station 58 and OBS station 30 (Figs. 3.6 and 3.8). They may originate from a high P-wave velocity contrast across the plate boundary indicating the presence of a subduction channel. A subduction channel is present when oceanic sediment remains attached to the subducting oceanic plate and/or material is removed from the upper plate, which is then subducted [von Huene and Scholl, 1991]. In addition to the subduction channel, elevated pore fluid pressure, which is likely to be generated by dewatering subducting sediments in that region [e.g., Hayward et al., 2003; Rüpke et al., 2004], may cause the high amplitudes, and simultaneously the low seismic P-wave velocities. However, the resolution of the refraction data is not sufficient to resolve a subduction channel of subducting sediment with low seismic P-wave velocity at the plate boundary with travelttime modeling. Therefore, the high amplitudes will be investigated with the method of one-dimensional wavefield modeling in the following chapter.

The interface of the oceanic/continental boundary across the entire Peruvian margin is added to a compilation of the slab depth from Gudmundsson and Sambridge [1998] in Figure 4.18. The 10- and 20-km-depths of the top of the subducting slab are from the refraction models of this study, the 10-km plate boundary depth at 14°S is from Hampel et al. [2004]. The 10- and 20-km-isolines (white dashed lines; Fig. 4.18) are interpolated between the GEOPECO profiles. Note that the flat subduction occurs further landwards where the oceanic/continental interface is at a depth range of 50 – 150 km.

#### 4.3. THE CONTINENTAL SLOPE AND SHELF STRUCTURE

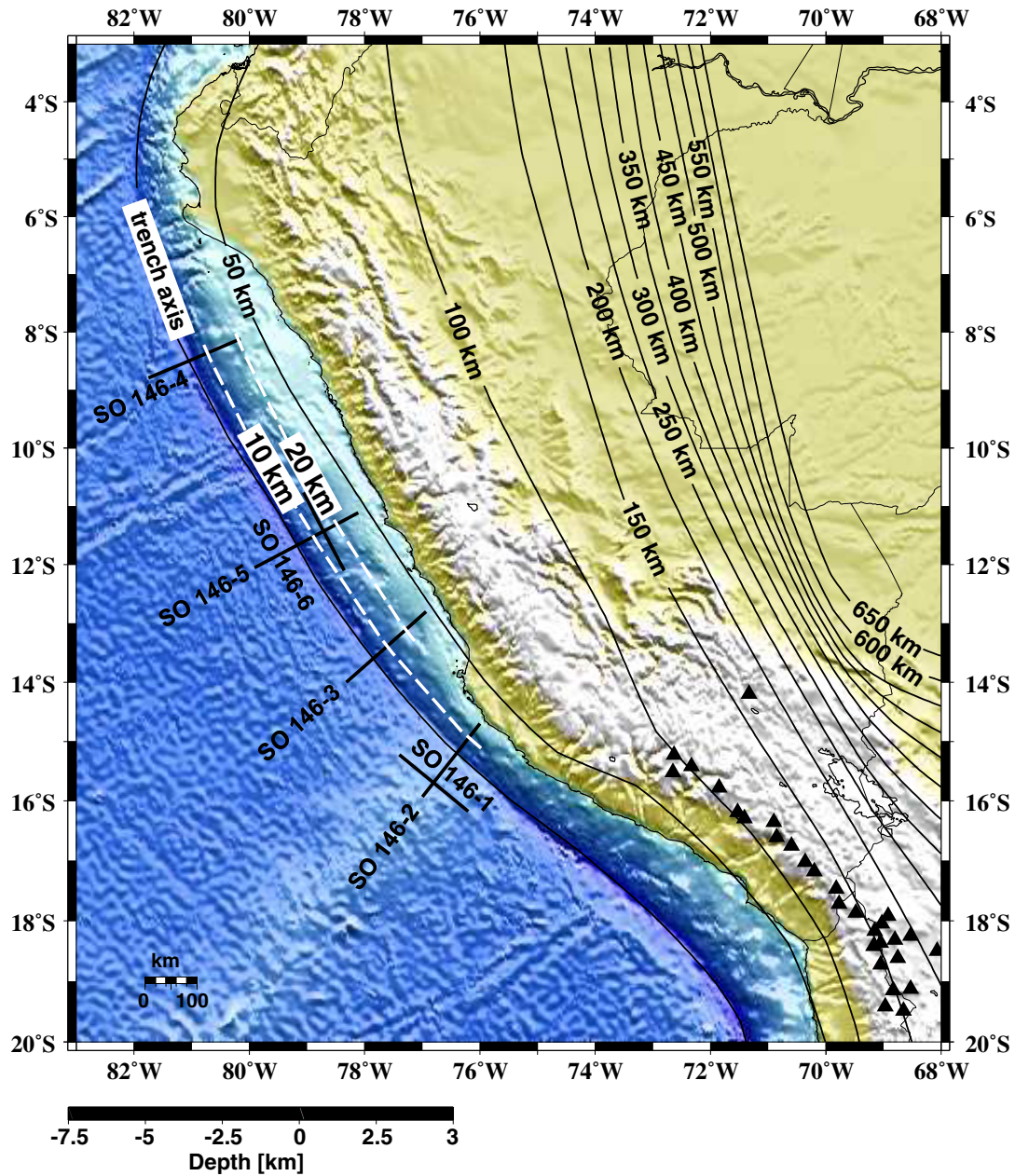


Figure 4.18: The depth of the subducting plate underneath the overriding continental plate is from Gudmundsson and Sambridge [1998] and the 10 and 20 km isolines from the refraction profiles. The active volcanic arc (triangles, from the Smithsonian Institution catalogue, available at <http://www.volcano.si.edu/world/summinfo.cfm>) is only present south of the research area, where there is no flat subduction. The active volcanic arc is located  $\sim 100$  km above the subducting oceanic plate as observed in all other subduction systems [Hamilton, 1995].

### The forearc basins across Peru

The structure of the Lima Basin obtained from the tomographic inversion along the strike-line SO146-6 from 11°S to 12.5°S reveals a 2-km-thick upper layer, defined by seismic velocities of 1.6–4.5 km/s (Fig. 3.11a). Figure 4.19 shows the perpendicular lines across Lima Basin for a better correlation. Although the data imply discrete boundaries, there are no sharp interfaces in the model of line SO146-6 as a result of the applied tomographic inversion method, compared to SO146-5 (obtained by forward modeling). The layer below the 2-km-thick upper layer exhibits P-wave velocities of 5.0–6.1 km/s. These are characteristic of the continental crust across the Peruvian margin, which is 8 km thick along profile SO146-6/12°S. The top of the downgoing oceanic plate is at a depth of about 11 km below the seafloor, 60 km landwards of the trench axis. The oceanic Moho is displayed at a depth of about 16 km below the seafloor, 60 km landwards of the trench axis. The uppermost layer of line SO146-6/12°S is thicker towards the south and the north of the Lima Basin, from 0–40 km and 140–170 km. There are also lateral variations in thickness of the layers below. The thickness decreases towards the peripheral regions, which might be an artifact due to the decreasing resolution of the tomographic inversion (Fig. 3.11b). Here, the depth of the ocean/continent boundary along profiles SO146-4/9°S and SO146-3/14°S, 60 km landwards of the trench, is taken into account (Figs. 4.4a and c). At this distance, the top of the oceanic plate is located at a depth of 13 km below the seafloor. This provides additional support for the idea that the continental crust may not be thinning towards the peripheral regions of strike-line SO146-6/12°S.

The sediment thickness in the basins south of the Mendaña Fracture Zone is 1.0–2.0 km, and therefore about half as thick as the sediments in the Yaquina and Trujillo Basins (SO146-4/9°S) which are around 3 km thick. This difference is also attributed to the uplift and subsidence caused by the southward migration of the Nazca Ridge and therefore its erosional effect on Peruvian forearc sediments. The slightly higher seismic P-wave velocities in Yaquina and Trujillo Basins at 9°S, with values from 1.7–3.0 km/s, compared to the velocities of 1.6–2.7 km/s in Lima and West-Pisco Basins are consistent with the thicker sediments on profile SO146-4/9°S and can therefore be explained by a higher degree of compaction. The sedimentary sequences at SO146-5/12°S reveal erosional scarps, which are correlated with the temporary uplift and permanent subsidence at 11 Ma when the Nazca Ridge passed under this region [Hampel, 2002; Clift *et al.*, 2003]. Such erosional scarps are restricted to the area of Lima Basin at profile SO146-5/12°S across Peru. Additionally, this part of the Peruvian margin was above sea level during the passage of the Nazca Ridge 11 Ma ago [von Huene and Suess, 1988], which was a period of increased erosion. In contrast, the profile north of the Mendaña Fracture Zone (SO146-4/9°S), which was never affected by the Nazca Ridge subduction, and the southernmost profile SO146-3/14°S, where the Nazca Ridge passed 6 Ma ago, have not been above the sea level.

#### 4.3. THE CONTINENTAL SLOPE AND SHELF STRUCTURE

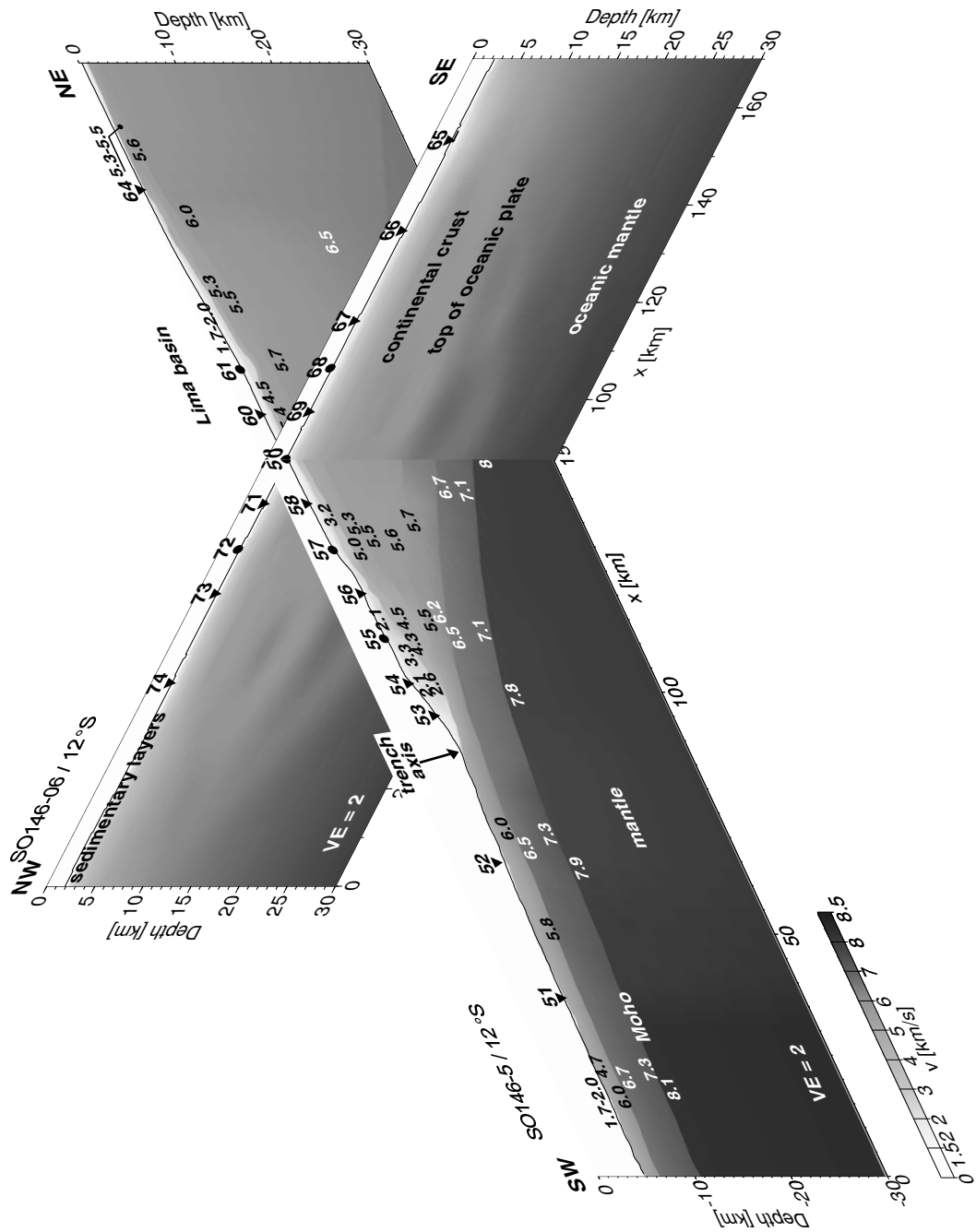


Figure 4.19: The models of the two crossing Profiles SO146-5 and SO146-6 at 12°S obtained from forward modeling and tomography. Locations of the OBH/OBS stations are marked by triangles/circles. Seismic P-wave velocities are gray shade coded and annotated.

Therefore, these two profiles were not exposed to enhanced erosion, as a consequence of uplift above the sea surface and subsequent subsidence. This difference in uplift and subsidence history across the Peruvian margin may explain why the sediment thickness in Lima Basin (12°S) is only 1.0–1.5 km thick, compared to 2 km in West Pisco Basin (14°S, also affected by Nazca Ridge subduction), and the 3 km thick Yaquina and Trujillo Basins (9°S).

The rough morphology along the middle slopes of the transects, in addition to the internal material strength, may reflect tectonic activity such as basal removal of upper plate material, which increases the surface slope. This would operate in conjunction with the strong coupling already mentioned above. Figure 4.20 comprises the interpretations and characteristics, derived from the refraction models of this study, across the overall erosive Peruvian margin. The area at the oceanic/continental plate interface, where subduction erosion is most effective, is indicated by the bold line (mostly beneath the backstop structure; Fig. 4.12). For line SO146-5/12°S the increase in wedge taper is most distinct at 120 km. Concurrent with the steep slope, indicating high basal friction, the dip angle of the subducting plate steepens (white arrow, Fig. 4.12). The change of slope angle across the continental margin, not only the slope angle across the lower slope, is annotated in Figure 4.12, and used to evaluate the material properties within the margin. The dip angle increases with distance from the trench across all three refraction lines across the Peruvian margin, but most distinct at 12°S, profile SO146-5 (from  $\alpha = 5.5^\circ$  to  $\alpha = 11^\circ$ , Fig. 4.12). This indicates that the basal friction is highest in this region of the investigated Peruvian margin. Therefore, the assumption is likely, that subduction tectonic erosion is most effective in this portion of the plate boundary. This process was described earlier by *Adam and Reuther* [2000] and *von Huene and Ranero* [2003] for the Chilean margin.

### 4.3. THE CONTINENTAL SLOPE AND SHELF STRUCTURE

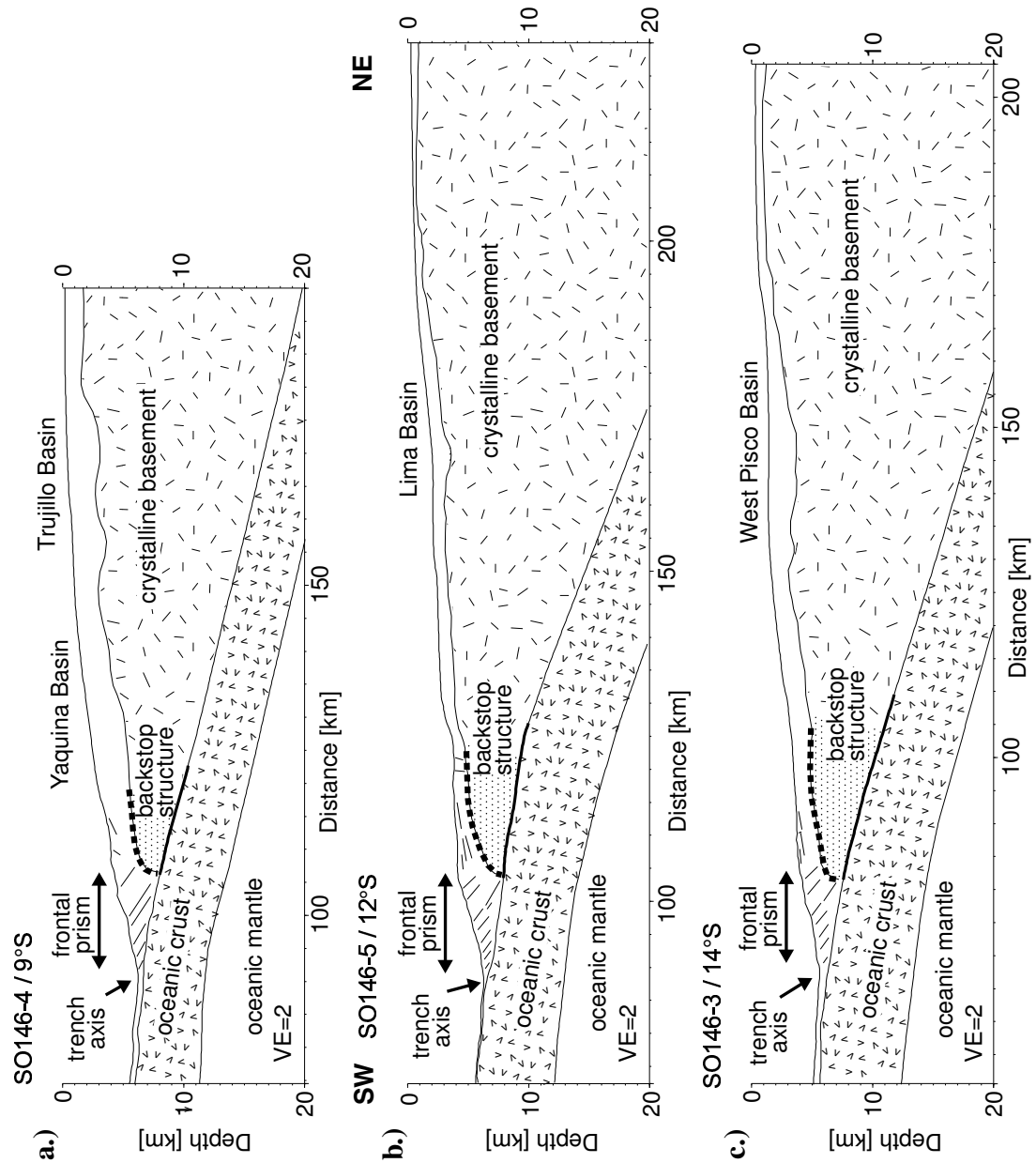


Figure 4.20: Structural models from north to south. Line drawings at the toe of the margin are incorporated from earlier reflection seismic studies [e.g. Kulm et al., 1981; von Huene and Suess, 1988]. The structure of the backstop has been inferred from P-wave velocities derived from the refraction seismic data. The dotted area is characterized by lower seismic velocities than the landward part of the continental crust. The bold line at the continental/oceanic plate boundary marks the zone where we assume that basal erosion is most effective.



---

## Amplitude modeling

Two-dimensional P-wave velocity-depth models are obtained by traveltime forward modeling and tomographic inversion. Along all refraction profiles of this study, high amplitudes are observed beneath the forearc region, originating from the top of the oceanic crust (see Fig. 3.6). These amplitude patterns cannot be analyzed by traveltime modeling, but with one-dimensional wavefield modeling. Here, the Reflectivity Method [Fuchs and Müller, 1971] is used as an additional interpretational tool for the GEOPECO refraction seismic dataset, to explain the observed strong amplitudes at the top of the subducting oceanic crust. This amplitude modeling method is based on the computation of the total solution of the wavefield, by means of integrating over horizontal wavenumber or slowness. Early works on elastic waves in layered media are published by, e.g., Ewing *et al.* [1957] and Brekovskikh [1960]. Equations for the calculation of the time-source signal and the far-field (seismogram) with the Reflectivity Method are given in the Appendix B. The use of the method is limited in that way, because the Earth is always assumed to be horizontally layered [e.g., Sandmeier and Wenzel, 1986]. Consequently, the velocity-depth model, which serves as input for the wavefield computation, is one-dimensional.

Due to the complexity of the two-dimensional structure of the convergent margin setting (trenchward dipping seafloor and landward dipping subducting plate), the previous analysis has been restricted to traveltime modeling. Profile SO146-6/12°S across Lima Basin, revealing small structural change in physical properties and structural styles, compared to the perpendicular crosslines (e.g., Fig. 4.19), is suitable for **one-dimensional** amplitude modeling with the Reflectivity Method [Fuchs and Müller, 1971]. The flowchart in Figure 5.1 illustrates the scheme of the Reflectivity Method.

A full waveform seismogram is calculated. The P-wavefield is computed as well as P-S converted waves for the hydrophone component. To generate the seismic signal an explosive source is chosen, which simulates the airgun source and the shape of the seismic signal is the Fuchs-Müller signal [Müller, 1968]. The computation of the Fuchs-Müller signal is given in Appendix B. The frequency content of the Fuchs-Müller signal used here has corner frequencies of 3/5–20/40 Hz, to simulate the dominant frequencies of the airgun signal, recorded in the seismic sections. An antialias filter is applied to the synthetic seismogram, but some modeling artefacts in the synthetic section could not be eliminated (e.g., the phase, that originates at 0 s and –8 km offset, and ends in the direct wave at zero-offset and 1.5 s, Figs. 5.3b, 5.4b and 5.5a,b). The method is based on the viscoelastic wave equations. This means, that the seismic velocities ( $v_p$ ,  $v_s$ ), the density ( $\rho$ ), as well as the seismic attenuation ( $Q_p$ ,  $Q_s$ ) are modeled [e.g., Christeson *et al.*, 2000].

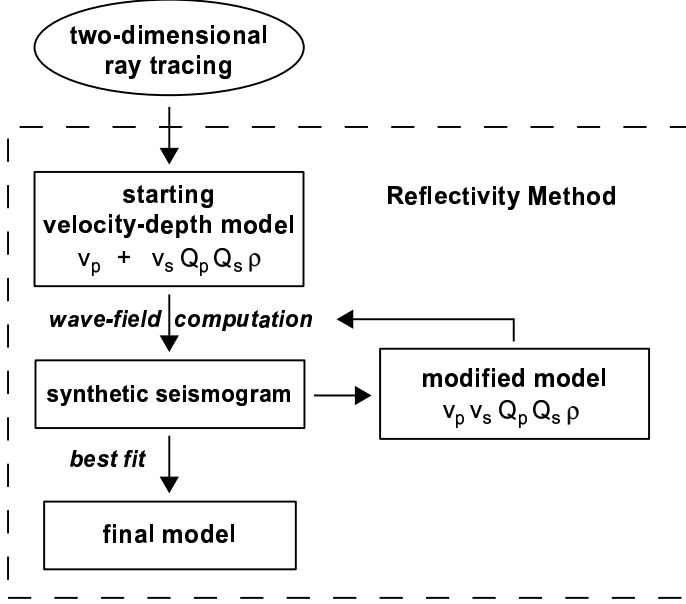


Figure 5.1: Scheme of the Reflectivity Method. The one-dimensional velocity-depth distribution for the starting model is derived from the result of a traveltime forward modeling technique. The steps involved in computing the wavefield with the Reflectivity Method are within the dashed box.

The physical parameters are partly taken from other modeling techniques (e.g., the P-wave velocity), partly calculated (e.g., the S-wave velocity), and partly tested (e.g.,  $Q$ ). The P-wave velocity,  $v_p$ , is taken from the forward model, as mentioned above. The S-wave velocity,  $v_s$ , is calculated from the P-wave velocity, using the relationship  $v_s = v_p/\sqrt{3}$ . The values for  $Q_p$  are literature values [Sheriff and Geldart, 1995], and  $Q_s$  is obtained by the relationship  $Q_s = Q_p/2$ . The values for the densities  $\rho$  are taken from Heinbockel et al. [2003]. They were derived from gravity modeling. The values are listed in Table 5.1.

Depth [km]	Vp [km/s]	Vs [km/s]	Qp	Qs	$\rho$ [g/cm <sup>3</sup> ]
0–2.24	1.5	0	1000	0	1.0
2.24–3.3	1.65–2.3	0.9–1.3	50–100	25–50	1.8–1.9
3.3–14.2	3.4–5.9	1.95–3.4	400–500	200–250	2.3–2.8
14.2–14.4 (LVZ)	4.5	3.0	400	200	2.5
14.4–30	6.2–7.95	3.5–4.59	500–600	250–300	2.8–3.3

Table 5.1: Values for  $V_p$ ,  $V_s$ ,  $Q_p$ ,  $Q_s$ , and  $\rho$  with depth, used for amplitude modeling.

The hydrophone component of OBS station 70, located in Lima Basin at the crossing point of Profile SO146-6 with SO146-5 at 12°S serves as a representative example. The seismogram is displayed in Figure 5.2. The one-dimensional velocity-depth distribution obtained by forward modeling underneath the OBS station 70 serves as starting model. It is displayed in Figure 5.3, as well as the synthetic seismogram, the result from amplitude modeling, and the observed refraction data. White noise is added to the synthetic seismogram for a better comparison with the recorded refraction seismogram.

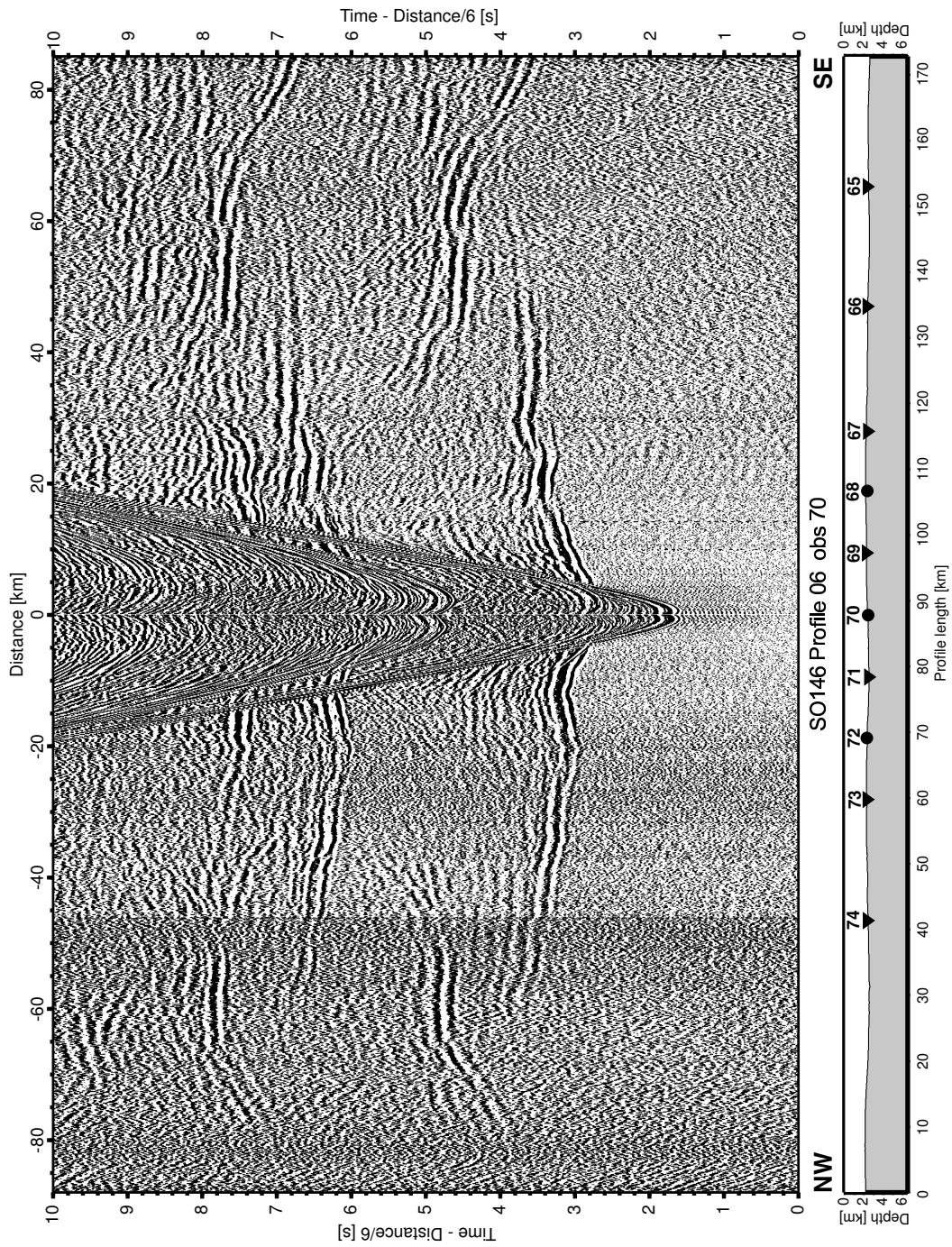


Figure 5.2: *Representative example of a wide-angle seismic section (hydrophone component) recorded by OBS 70, located in Lima Basin at the crossing point of profile SO146-6 with SO146-5 at 12°S. The data are displayed with a reduction velocity of 6 km/s. The topography along the profile is shown underneath the seismic section, note the small changes in water depth across the line. Triangles/circles mark the locations of the OBH/OBS stations.*

The velocity-depth model is then modified to satisfy the high amplitudes in the recorded refraction seismic data. The resulting synthetic seismogram, with white noise added, is shown in Figure 5.4. The large computation time results from the task to model the phases of interest at large offsets with a high sampling rate and large recording time. Here, the wavefield is calculated for the distance of 80 km from the OBS station, with a distance increment of 150 m. The water depth is  $\sim 2240$  m. At a sample interval of 0.0125 s, the recording time is set to 25 s, to calculate all phases of interest and display the synthetic seismogram with a reduced velocity of 6 km/s.

### 5.1 Is there evidence for a subduction channel?

The forward modeling techniques provide depth-velocity models, which give information about the crustal structure of the research area. While interpreting the two-dimensional velocity-depth models, some questions arise due to the limitation of the method (which is reduced to traveltimes modeling). These tasks are associated with the continental-oceanic crustal boundary, e.g., how thick is the sediment layer subducting underneath the continental plate (subduction channel). The computation of the wavefield and comparison of the synthetic with the recorded seismogram gives additional information about the physical parameters of the crust.

#### **Considerations of the limitation of the forward modeling technique to approximate the subduction-channel thickness**

The maximum thickness of sediment on the incoming oceanic crust is  $\sim 200$  m, but mostly thinner along Profile SO146-5/12°S (Fig. 4.4). Additional sediment, which might be subducted, is the eroded material from the overriding plate. The long-term rates of subduction erosion, calculated for the Peruvian margin by *Clift et al.* [2003] reach from 1.5–3.1 mm/a trench retreat. These values are in the range of the values derived from an earlier investigation of *von Huene and Lallemand* [1990].

After the Eocene the average erosion rate was 3.1 mm/a, which is used here to calculate the amount of eroded material. *Clift and Vannucchi* [2004] estimated a volume of 150 km<sup>3</sup>/my (= 150000 m<sup>3</sup>/y) for the tectonic erosion rate of the forearc basement along the entire Peruvian margin at its length of 2200 km. The volume divided by the trench length and the trench retreat rate yields the values of 20 m thickness and 0.0031 m width of subducted material per year and trench kilometer. It is assumed that subduction erosion is a continuous process, which is associated with material being offscraped from the upper plate. Therefore, the values of subducted material can be imagined as a 20 m long segment at the base of the upper plate with 0.0031 m thickness, which is eroded per year and trench kilometer. The amount of incoming sediment is more than three magnitudes larger than the portion of eroded material. Hence, the offscraped upper plate material is not accounted for in further considerations of the subduction channel thickness, although subduction erosion is present at the Peruvian margin.

The vertical resolution of seismic data is dependent on the wavelength of the seismic signal,  $\lambda$ , which is in relation with the dominant frequency,  $f$ , of the data and the sound velocity,  $v$ , of the material [e.g., *Sheriff and Geldart, 1995*]:

$$\lambda = \frac{v}{f} \quad (5.1)$$

A layer of thickness  $\lambda/4$  or larger is resolvable [e.g., *Sheriff and Geldart, 1995*]. When the layer thickness is less than  $\lambda/4$ , the two reflections (upper and lower interface) are not resolvable in the time domain, and thickness information is encoded in the amplitude and shape of the wavelet [*Kallweit and Wood, 1982*]. The Earth acts as a filter and consequently lowers the frequency of the seismic signal with depth. For the GEOPECO dataset, a mean value of  $f = 6$  Hz is reasonable for the resolution calculation. The depth of the oceanic-continental boundary underneath Profile SO146-6/12°S is  $\sim 14$  km ( $\sim 12$  km below the seafloor, e.g., Fig. 4.19). The overload of the margin and the resulting compaction of the material in the subduction channel is considered. Therefore a material velocity of  $v \sim 4000\text{--}5000$  m/s is used for the vertical resolution calculation of the subduction channel. The above values result in a  $\sim 150\text{--}200$ -m-thick subduction channel, which theoretically can be resolved with the traveltime interpretation. In the recorded seismograms such a subduction channel is not identified by traveltime observations. Therefore the maximum thickness of the subduction channel, if present at the Peruvian margin is presumably smaller than  $\sim 150\text{--}200$  m. The seismic velocities of the subduction channel increase as a result of the material overload, while in contrast the layer thickness of the incoming Layer 1 decreases.

### 5.1.1 Thickness of the subduction channel

While modeling the synthetic seismogram of a section along this profile with the Reflectivity Method, the interest is focused on the phases with strong amplitudes originating from the top of the subducting oceanic crust (indicated by the arrow in Figures 5.3–5.5). The origin of the strong amplitudes may result from the increased impedance contrast, caused by the lower seismic velocities within the subduction channel at the continental crust/subduction channel interface, as well as the subduction channel/oceanic crust interface [e.g., *Sheriff and Geldart, 1995*]. The impedance contrast is defined by:

$$\frac{\rho_1 v_1}{\rho_2 v_2} \quad (5.2)$$

with:  $\rho_1 v_1$  = the product of the velocity and density of layer 1,  
and  $\rho_2 v_2$  = the product of the velocity and density of layer 2.

A variety of one-dimensional velocity-depth models are tested: without low velocity zone (LVZ) above the oceanic crust (Fig. 5.3), and a low velocity layer (LVL) on top of the oceanic crust with varying thickness, simulating the subduction channel (Figs. 5.4, 5.5). There are differences between the recorded and the 'best fitting' synthetic seismograms.

## 5.1. IS THERE EVIDENCE FOR A SUBDUCTION CHANNEL?

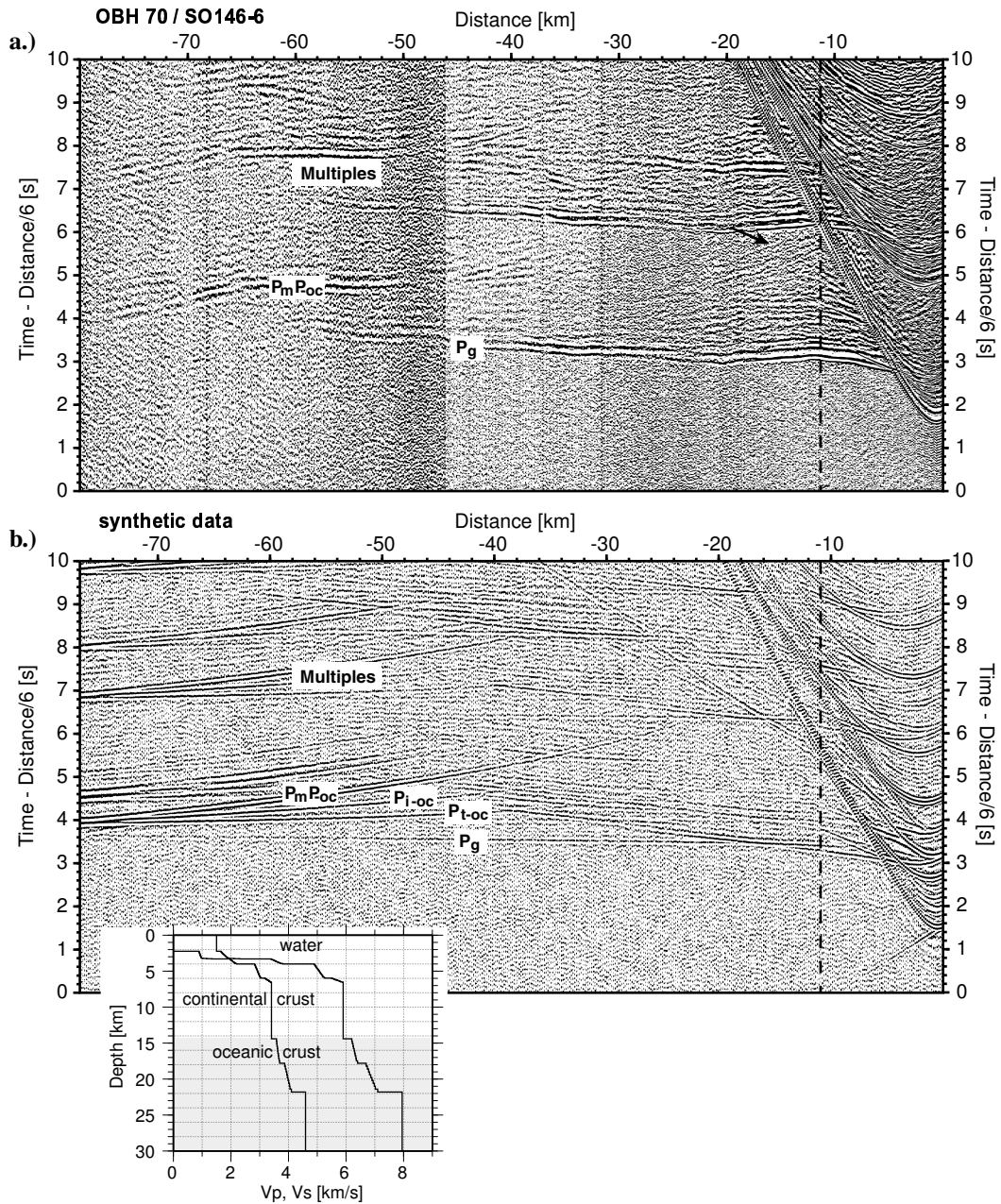


Figure 5.3: *One-dimensional amplitude modeling of OBS 70, Profile SO146-6/12°S. (a) shows an enlargement of the recorded refraction data. (b) shows the modeled section overlain with white noise. The velocity-depth distribution used for modeling is displayed, the gray zone marks the velocities of the subducting oceanic plate. No low velocity layer is implemented on top of the oceanic crust. The arrow in the seismic data points at the high amplitudes (a). The dashed line marks the offset, where the top of the oceanic crust reflection crosses the direct wave.  $P_g$ : continental basement refraction;  $P_m P_{oc}$ : oceanic mantle reflection;  $P_t-oc$ : top of the oceanic crust reflection;  $P_i-oc$  intracrustal oceanic reflection.*

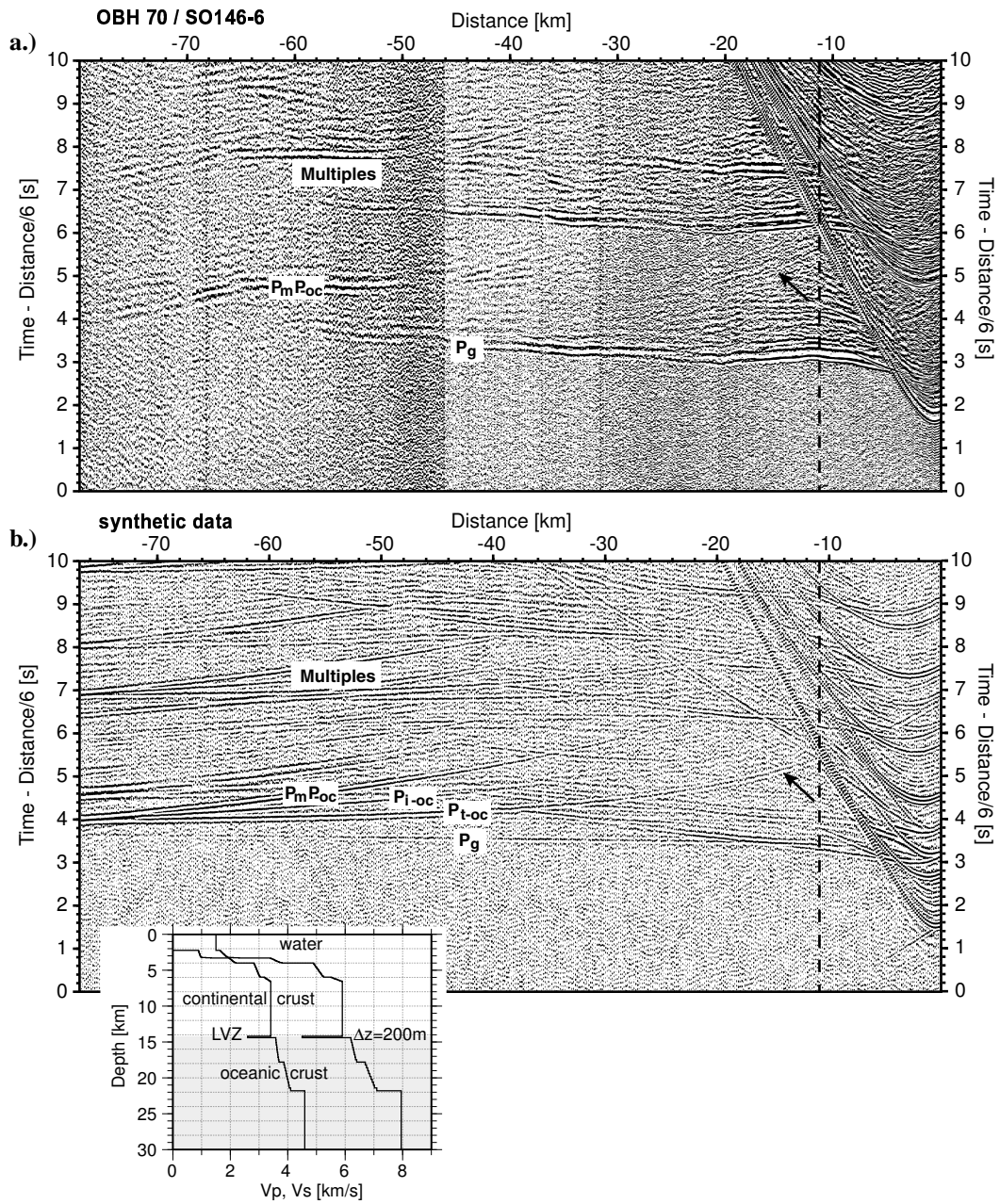


Figure 5.4: *One-dimensional amplitude modeling of OBS 70, Profile SO146-6/12°S. (a) shows an enlargement of the recorded refraction data. (b) shows the modeled refraction data overlain with white noise. The velocity-depth distribution used for modeling is displayed, the gray zone marks the velocities of the subducting oceanic plate. A low velocity layer (LVZ,  $v_p = 4.5$  km/s, 200 m thick) is implemented on top of the oceanic crust. The arrow in the seismic data points at the high amplitudes (a and b). See Figure 5.3 for abbreviations.*

## 5.1. IS THERE EVIDENCE FOR A SUBDUCTION CHANNEL?

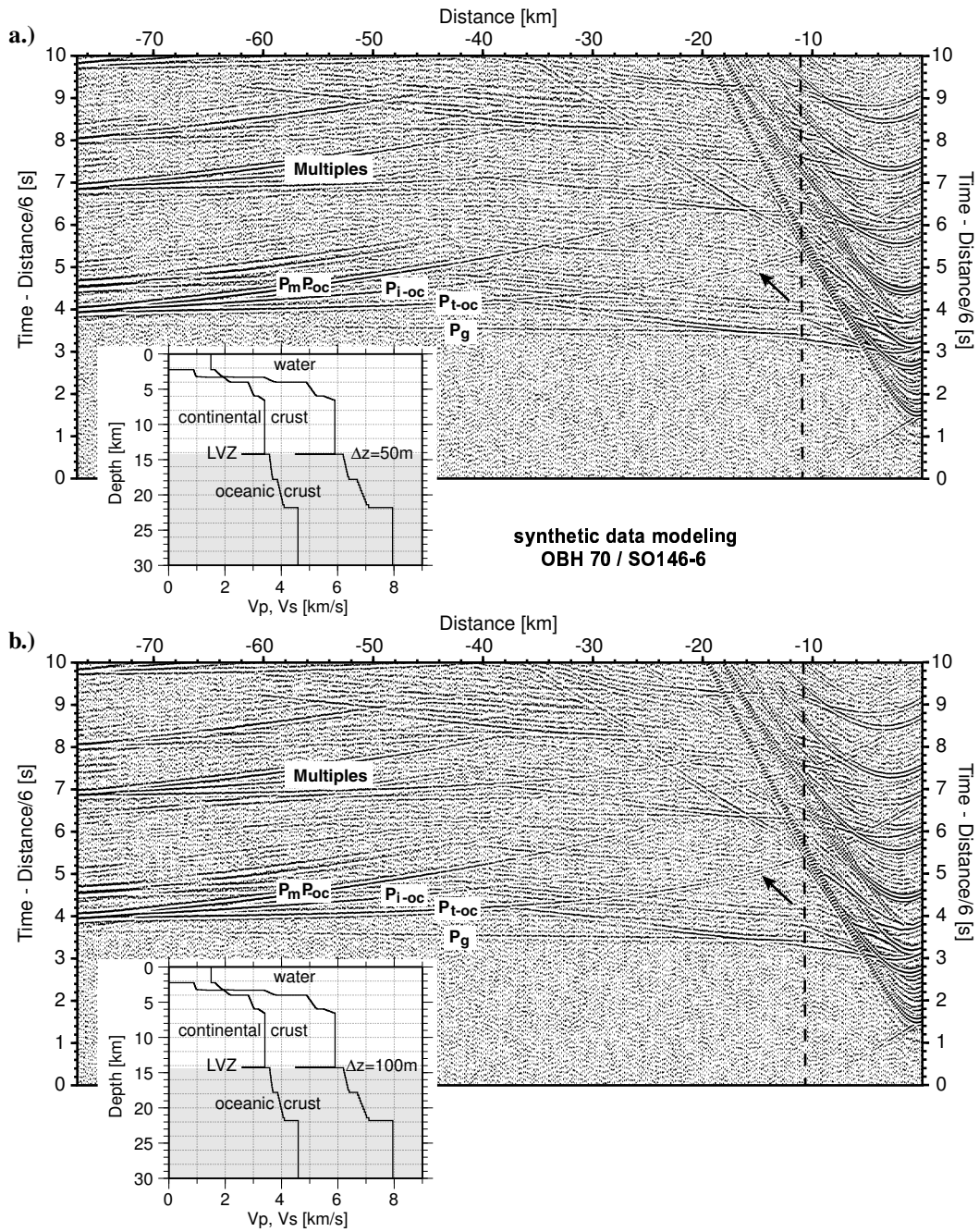


Figure 5.5: One-dimensional amplitude modeling of OBS 70, Profile SO146-6/12°S. The modeled refraction data overlain with white noise. The velocity-depth distribution used for modeling is displayed. A low velocity layer (LVZ,  $v_p = 4.5$  km/s) is implemented on top of the oceanic crust with a thickness of (a) 50 m and (b) 100 m. The arrow in the seismic data points at the high amplitudes (a and b). See Figure 5.3 for abbreviations.



Some of the reasons for the occurrence of these differences are, e.g., that the modeling technique is one-dimensional and the recorded wavefield is three-dimensional and the modeling parameters might have to be optimized (values for the quality factor  $Q$ , etc.). The strong amplitudes in the synthetic seismogram can only be modeled with the low velocity zone in the velocity model (compare  $P_{t-oc}$ , top of the oceanic crust reflection, and  $P_{i-oc}$ , intracrustal oceanic reflection, in Figures 5.3 and 5.4). In all synthetic seismograms, the  $P_{t-oc}$ ,  $P_{i-oc}$ , and  $P_mP_{-oc}$  have strong amplitudes at large offsets, here,  $> |40|$  km (Figs. 5.3–5.5). The recorded refraction data across profile SO146-6/12°S consistently show strong amplitudes of the  $P_{t-oc}$ ,  $P_{i-oc}$ , and  $P_mP_{-oc}$  phases also at smaller offsets ( $< |40|$  km), OBS 70 is the representative example (Figs. 5.2–5.4). The amplitudes in the synthetic seismograms can be easier identified compared to the recorded data, especially in the small offset region, where the strong amplitudes of the direct wave and its multiple reflection interfere with low angle reflections. The traveltimes at zero-offset for the subducting oceanic plate reflections are at 6.7 s for the top of the oceanic plate ( $P_{t-oc}$ ), 7.7 s for the intracrustal reflection ( $P_{i-oc}$ ), and 8.9 s for the Moho reflection ( $P_mP_{-oc}$ ). The phases with the strong amplitudes at small offset ranges can be modeled with the low velocity zone, the amplitude of the intracrustal reflection,  $P_{i-oc}$ , is decreasing with decreasing thickness of the low velocity zone (compare Figures 5.3–5.5).

### A quantitative approach

A quantitative evaluation of the amplitudes originating from the reflection above the subducting oceanic crust is conducted with a LVZ of constant P-wave velocity (4.5 km/s) and varying LVZ-thickness of 50, 100, and 200 m. The amplitudes from the top of the subducting oceanic crust were picked. The amplitudes of the synthetic seismogram without low velocity zone, picked from the top of the subducting oceanic crust are shown for comparison (Fig. 5.6). They could be well-identified in the dataset, without noise added (not shown here). The phase reversal due to the negative velocity contrast of the low velocity zone is accounted for. To compare the amplitudes of the recorded with the synthetic data, a normalization is carried out. Generally, the amplitudes are calibrated to the amplitudes of the direct wave. Unfortunately the amplitudes of the direct arrival of OBS 70, Profile SO146-6/12°S were clipped, therefore the amplitudes of the first arrival in the offset range from  $|6 - 10|$  km served as reference. The absolute amplitude values plotted against the offset are shown in Figure 5.6. There is a big uncertainty, which results from the strongly varying reference values of the recorded seismogram (left grey curve, Fig. 5.6). These large amplitude variations may result from the three-dimensionality of the recorded wavefield. Fitting the maximum/minimum amplitude reference values of the recorded to the synthetic curve results in an uncertainty of  $\pm 100$  m for the LVL-thickness. Here, the normalization with mean amplitude values of the reference curve are taken for comparison of amplitudes picked from the low velocity zone above the subducting oceanic crust.

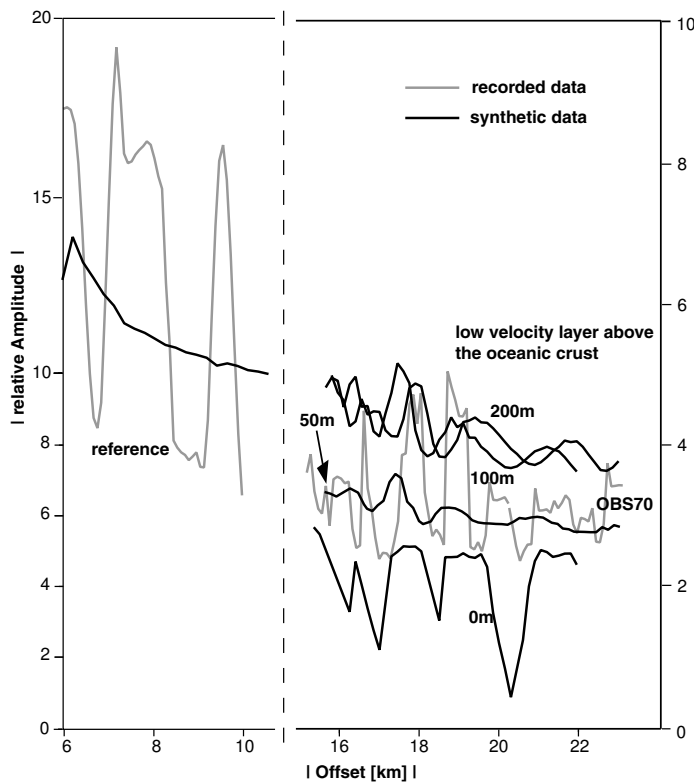


Figure 5.6: Amplitude values of the synthetic seismograms (black), with a LVL with  $v=4.5\text{km/s}$ . Amplitudes increase with varying LVL-thickness from no low velocity zone (0 m) to a low velocity layer of 200 m thickness above the subducting oceanic crust (right). The normalized corresponding amplitudes of OBS 70, Profile SO146-6/12°S is plotted in grey. The amplitudes of the reference reflector plot in the upper left corner (grey-synthetic/black-recorded).

The trend of decreasing amplitudes with offset is observed in both, the recorded and the synthetic amplitudes (Fig. 5.6). The amplitudes of the synthetic data from the low velocity zone/top of the oceanic crust increase with increasing LVZ-thickness and a constant velocity of the LVZ ( $v_p=4.5\text{ km/s}$ ) (Fig. 5.5). The average of the values from OBS 70, Profile SO146-6/12°S plot in the range of amplitudes obtained by modeling a 50-m-thick subduction channel.

To test the sensitivity of the LVZ-velocity, the amplitudes reflected at the LVZ are modeled with a constant LVZ-thickness of 50 m and varying P-wave velocities of 3, 3.5, 4, 4.5, and 5 km/s. The amplitudes are calibrated as described above with varying thickness of the subduction channel. As expected, amplitudes increase with decreasing velocity of the LVZ, see Figure 5.7, right. The amplitude curves modeled with 4–5 km/s show the same trend as the amplitudes of the recorded seismogram, whereas the amplitudes modeled with a LVZ-velocity of 3/3.5 km/s show decreasing amplitudes with increasing offsets. A subduction channel velocity of 4.5 km/s is reasonable for the LVZ at a depth of  $\sim 15\text{ km}$  [Christeson et al., 2000], while slightly higher LVZ-velocities (5 km/s) imply a slightly thicker LVZ (up to 100 m) to satisfy the recorded amplitudes (grey curve, Fig. 5.7, right).

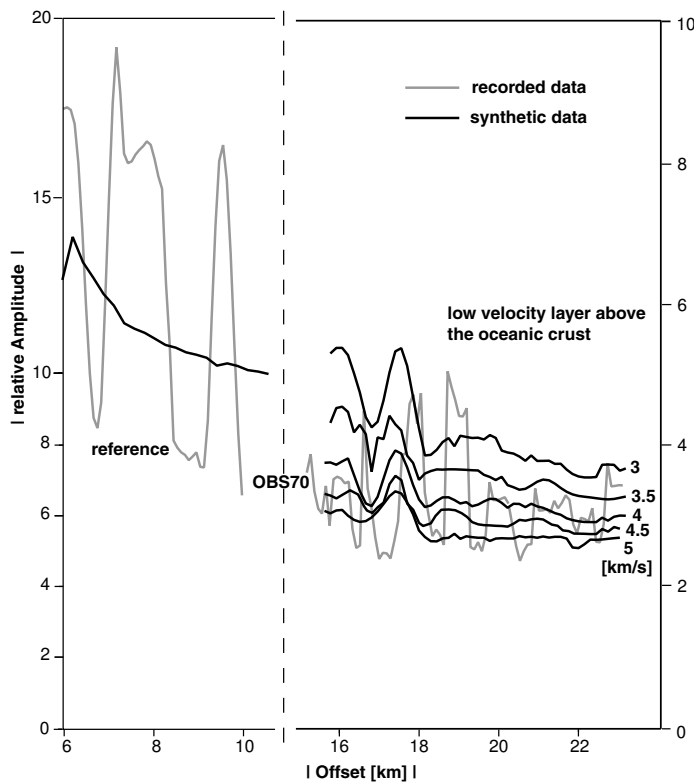


Figure 5.7: *Amplitude values of the synthetic seismograms (black), with a LVL-thickness of 50 m. Amplitudes increase with varying LVL-velocity from 5 km/s to 3 km/s (velocities are annotated) above the subducting oceanic crust (right). The normalized corresponding amplitudes of OBS 70, Profile SO146-6/12°S is plotted in grey. The amplitudes of the reference reflector plot in the upper left corner (grey-synthetic/black-recorded).*

The qualitative approach of amplitude modeling suggests the presence of a subduction channel by the strong amplitudes from the top of the oceanic crust in the synthetic seismograms modeled with a LVZ, in contrast to very weak amplitudes originating from the top of the oceanic crust modeled without LVZ (compare Figures 5.3–5.5). A subduction channel thicker than  $\sim 200$  m is not reasonable, because the average sediment income into the subduction zone across this portion of the Peruvian margin is smaller ( $< 200$  m, Fig. 4.4) and the sediment package is compacted with depth. Additionally, a thicker subduction channel would be resolvable with the traveltime analysis, which again, does not satisfy the refraction seismic data. The quantitative examination of the amplitudes indicate values of  $\sim 50$  m subduction channel thickness and a seismic velocity of  $v_p=4.5$  km/s from the one-dimensional wavefield model of OBS 70 on profile SO146-6/12°S (Fig. 5.5a).



# 6

## Seismicity in subduction zones

Seismicity is an important tool to derive the tectonics of a region [e.g. *Scholz, 1990*]. The major global seismic moment release occurs at subduction zones. Different seismicity patterns occur at subduction zone settings [e.g. *Scholz, 1990*; *Pacheco and Sykes, 1992*; *Ruff, 1996*]. Their characteristic seismicity features are illustrated in Figure 6.1. Most of the largest earthquakes in subduction zones occur by thrusting along the plate interface, e.g., the interplate events with a moment magnitude  $M_w \geq 8.0$  across Peru in 1940, 1942, 1966, 1974, and 2001 from the global catalog of *Ruff [1996]* and *Kikuchi and Yamanaka [2001]* for the 2001 thrust earthquake. Their size is mostly related to the along-strike than the down-dip rupture width [*Ruff, 1996*]. Intraplate earthquakes that are generally characterized by minor seismicity occur in both, the overriding and the subducting plates [*Scholz, 1990*]. In general, earthquakes are absent in the accretionary wedge [e.g. *Byrne et al., 1993*], the toe of the overlying plate.

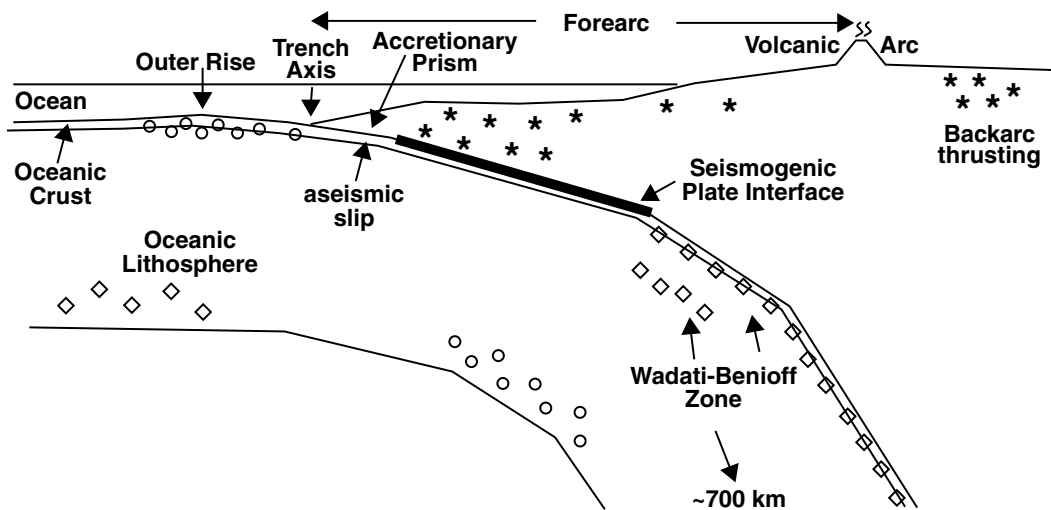


Figure 6.1: *Schematic diagram, illustrating the zones of inter- and intraplate earthquake occurrence and the characteristic features across subduction zones, modified after *Byrne et al. [1988]*. Interplate earthquakes: bold line: thrust events, region where most great earthquakes occur. Intraplate earthquakes: asterisks: shallow upper-plate earthquakes; circles: bending-related normal events; squares: bending-related thrust events.*

Seismicity in the upper plate occurs in the forearc as well as the backarc region. The upper plate earthquakes typically indicate compression normal to the arc. The volcanic arc itself is characterized by small earthquakes commonly associated with volcanism [Ruff, 1996]. A variety of earthquakes occur in the subducting plate: Normal faulting earthquakes, resulting from bending, occur close to the axis of maximum bending within the subducting plate [Scholz, 1990]. These typically occur at the outer rise with most epicenters in the vicinity of the trench axis. A global survey shows, that the tension axis of most of these normal faulting events is trench-perpendicular. Their focal depths are quite shallow [Ruff, 1996]. These outer-rise earthquakes may persist farther landwards beneath the arc, and at greater depths merge into the Wadati-Benioff zone, where deep thrust events occur in the subducting slab beneath the upper and lower plate interface. Earthquakes across subduction zones may extend to depths of nearly 700 km (Fig. 6.1). The intermediate and deep focus earthquakes reflect internal stress of the downgoing slab. The deeper earthquakes are attributed to phase transformations. In general, earthquakes occur in the brittle crust and lithosphere and terminate beneath the brittle-ductile boundary.

Several methods can be applied to obtain the tectonics from earthquake activity, such as the analysis of focal mechanisms in order to estimate stress directions [Scholz, 1990]. Here, only the focal depth of earthquakes is considered and related to the structure obtained from the refraction seismic profiles across the Peruvian margin.

## 6.1 Earthquake distribution across the Peruvian continental margin from a regional network

The geometry of the subducting slab obtained from the refraction seismic profiles is correlated with the focal depths of earthquakes that occurred in the region of each refraction profile within one degree Latitude. The earthquakes are projected on the refraction profiles SO146-3 – SO146-5 ( $9^{\circ} - 14^{\circ}\text{S}$ ) and plotted across the Longitude (Figs. 6.2–6.3). These earthquakes are taken from the regional network catalog of the Instituto Geofísico del Perú [Huaco, 1986, 1999] and [E. Norabuena pers. communication] during the period of 1982 to 2001. The focal depths of the earthquakes are biased due to the sparse network. The range of magnitudes for these events is  $M_b = 1.7 - 5.7$ , with the majority of earthquakes ranging from  $M_b = 4.5 - 5.0$ . No great thrust events occurred during this period.

Several earthquakes are distributed in the upper plate across the forearc, further landward from the frontal prism (Figs. 6.2–6.3). Aseismic slip occurs at the oceanic-continental interface beneath the accretionary prism, where no earthquakes are registered across all three profiles. Some interplate events are distributed at greater depths beneath the forearc, reflecting the sudden stress release across the plate boundary. The earthquakes in the subducting oceanic crust and upper mantle are likely to be related with the bending of the lithosphere. However, this small-scale observation does not

reveal any focusing of earthquakes across the plate boundary to be correlated with the subducting slab obtained in the GEOPECO refraction profiles (Figs. 6.2–6.3). Therefore, the structure of the refraction profiles is correlated with the earthquakes from the Seismic Catalog of Peru (at <http://cns.igp.gob.pe>) [e.g. *Huaco, 1986; Norabuena et al., 1994; Tavera and Buforn, 1998; Huaco, 1999*] for a wider geometrical examination.

The Seismic Catalog of Peru comprises a compilation of data not only from the Instituto Geofísico del Perú [*Huaco, 1986, 1999*] used in the smaller scale investigation (Figs. 6.2–6.3), but also from the Centro Nacional de Datos Geofísicos-Sismología of Peru. Figure 6.4 shows the distribution of earthquakes during the period between 1960 and 1995 with shallow epicenters ( $h \leq 60$  km) (a), and intermediate ( $60 < h \leq 350$  km) and deep epicenters ( $h < 350$  km) (b) from the Nazca plate eastward to the Amazon plain. At their seaward end, lines A-A' and B-B' are almost coincident with the GEOPECO refraction lines SO146-4/9°S and SO146-3/14°S (Fig. 6.4b), and therefore allow a correlation (Fig. 6.5). Shallow subduction occurs across transects A-A' and B-B', and normal (deep) subduction across transect C-C' (Figs. 6.4, 6.5).

At this larger scale, the geometry of the subducting slab is revealed by the distribution of the earthquake epicenters. The dip of the modeled subducting slab fits well with the location of the earthquakes and complements the cross sections at their seawardmost part. The distribution of the shallow subduction in north and middle Peru, and deep subduction south of Peru, correlates with the location of the Nazca Ridge between these zones of differing subduction mechanisms. As described in the introduction, the buoyancy of the thickened oceanic crust of the Nazca Ridge is related to the flat subduction beneath Peru. The southward aseismic ridge migration might be the reason for the Peruvian margin to be the largest region with flat subduction worldwide and possibly the related lacking of active volcanism [e.g. *Barazangi and Isacks, 1976; Hasegawa and Sacks, 1981; Norabuena et al., 1994*].

## 6.1. EARTHQUAKE DISTRIBUTION ACROSS THE PERUVIAN CONTINENTAL MARGIN FROM A REGIONAL NETWORK

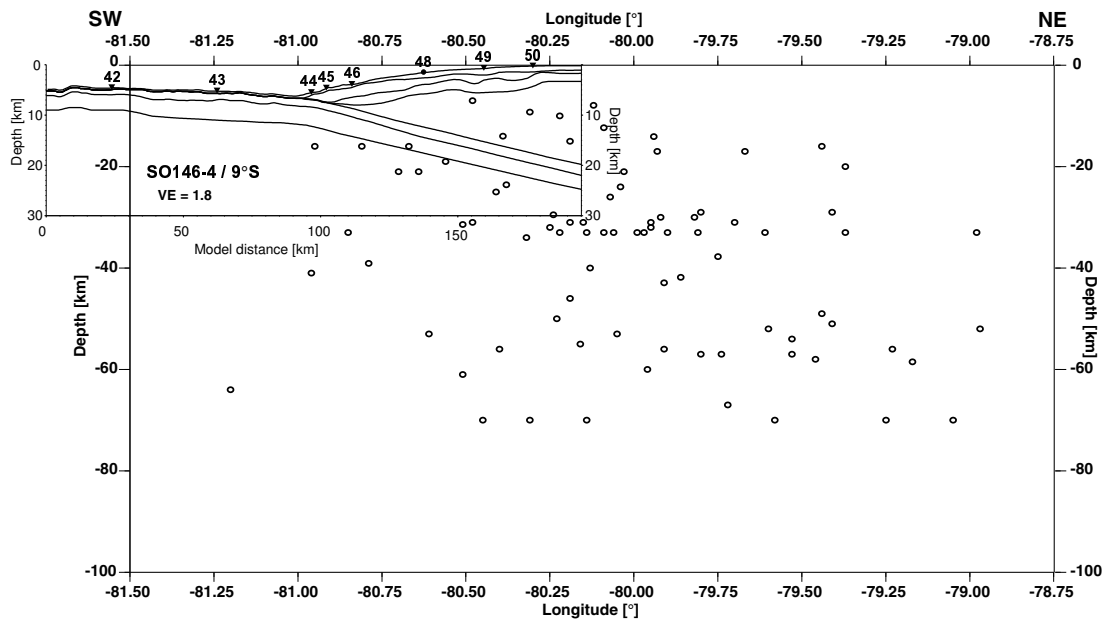


Figure 6.2: The structure of the refraction profile SO146-4/9°S in the upper left corner is displayed along with earthquake locations from the Peruvian local network (Seismic Catalog of Peru at <http://cns.igg.gob.pe>). The earthquakes from 8°S to 9°S were projected on the refraction profile and then plotted across the Longitude. Positions of OBH/S stations across the profile are annotated.



6. SEISMICITY IN SUBDUCTION ZONES

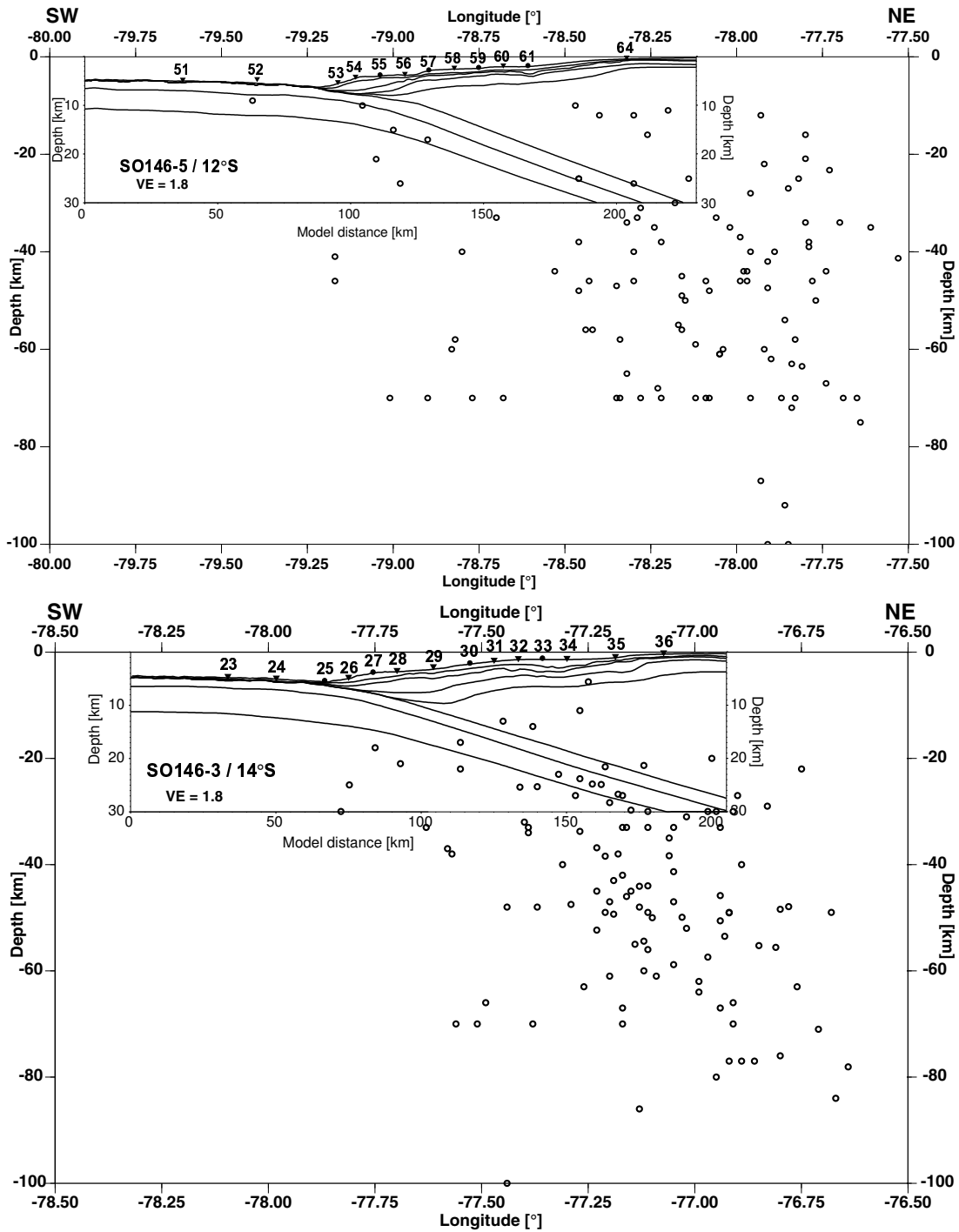


Figure 6.3: The structure of the refraction profiles SO146-5/12°S (top) / SO146-3/14°S (bottom) in the upper left corner is displayed along with earthquake locations from the Peruvian local network (Seismic Catalog of Peru at <http://cns.igp.gob.pe>). The earthquakes from 11°S to 12°S (top) / 13°S to 14°S (bottom) were projected on the refraction profiles and then plotted across the Longitude. Positions of OBH/S stations across the profile are marked.

6.1. EARTHQUAKE DISTRIBUTION ACROSS THE PERUVIAN CONTINENTAL MARGIN FROM A REGIONAL NETWORK

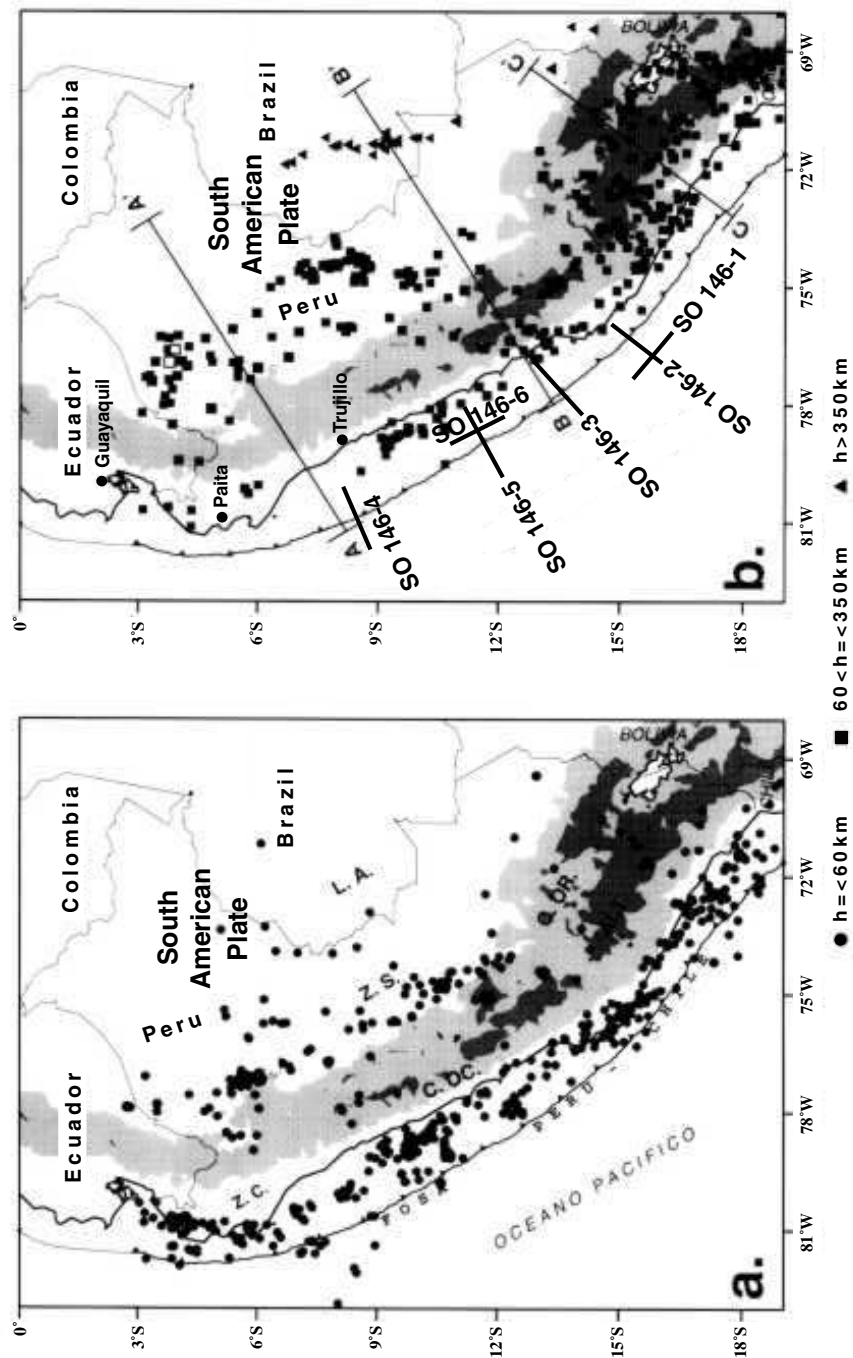


Figure 6.4: Location map of the earthquakes across the Peruvian margin, (a) showing earthquakes shallower than 60 km (circles), and (b) earthquakes deeper than 60 km (squares, triangles). SO146-1 to SO146-6 mark the locations of the GEOPECO refraction profiles. The data are from the Seismic Catalog of Peru for the period of 1960-1995 ( $m_b > 5.0$ ) (<http://cns.igp.gob.pe>). The maps were modified after Tavera and Buforn [1998]. Z.C.: Coastal Zone; C.O.C.: Cordillera Occidental; ALT: Altiplano; C.O.R.: Cordillera Oriental; Z.S.: Subandean Zone; L.A.: Amazon Plain.

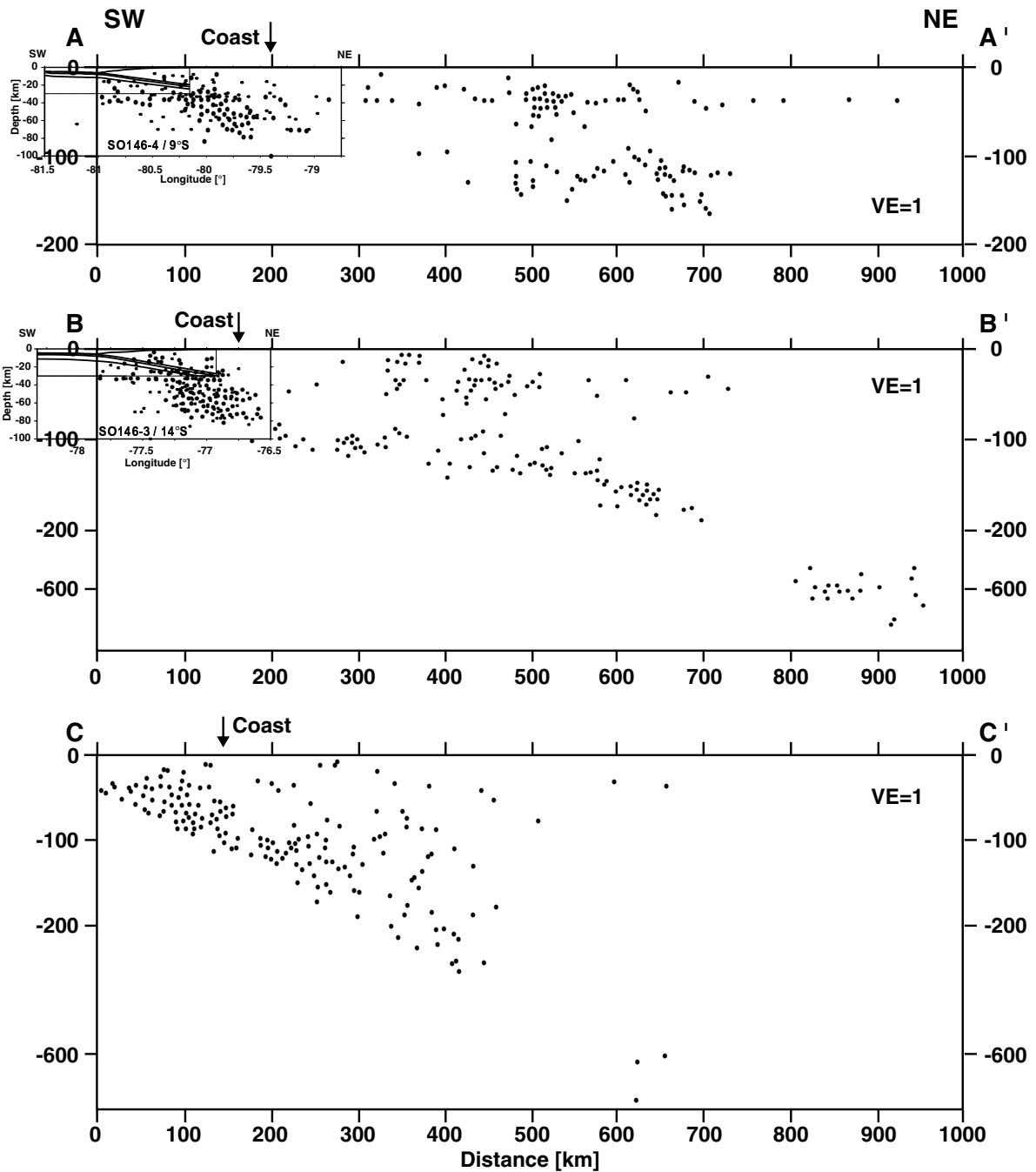


Figure 6.5: The cross sections A-A' in the north, B-B' in the middle of Peru, and C-C' across the southern Peruvian margin, modified after *Tavera and Bufo* [1998]. Their seaward portion starts at the Peru-Trench and the position of the coastline is marked by an arrow. Figures 6.2, with the dip of the subducting plate across refraction profile SO146-4/9°S, and 6.3 (bottom), with the dip of the subducting plate across refraction profile SO146-3/14°S, are included at the southwestern parts of transects A-A' and B-B'. See Figure 6.4 for locations. The vertical exaggeration is VE=1 at the upper 200 km, note the non-linear scale below 200 km across transects B-B' and C-C'.



---

## Conclusions and Outlook

Subduction processes and the crustal structure across the entire Peruvian margin from 9°S to 15°S are analyzed in this study. Seaward of the margin, Nazca plate oceanic crust with a 'normal' velocity structure and topped by a thin pelagic sedimentary layer, varying from 0–200 m thickness, is approaching the trench. The oceanic crust, with a total thickness of 6.4 km, is divided into an upper and a lower oceanic crustal layer, overlying the mantle with a seismic P-wave velocity of 7.9 km/s averaged across the three transects. In the region of Trujillo Trough at the western part of the northernmost transect, the oceanic crust has a thickness approximately of only 4 km, probably due to off-axis extension. To further quantify the areal extent of oceanic crustal thinning at the northernmost GEOPECO profile (at 9°S) in the region of Trujillo Trough, future investigations with a seaward extension of the seismic refraction profiles are needed.

The plate boundary of the subducting Nazca plate and the overriding South American plate is traced down to a depth of 25 km. However, data resolution is not sufficient to resolve a possible subduction channel by means of travelttime modeling. In some areas, the presence of subducting sediment is indicated by high amplitudes originating from the top of the subducting oceanic plate. These high amplitudes can be satisfied with a subduction channel thickness of ~50 m and a seismic velocity of 4.5 km/s with the one-dimensional Reflectivity Method. Two-dimensional amplitude modeling is likely to reduce the uncertainty of subduction channel thickness obtained within this study. Additional application of the two-dimensional amplitude modeling method, not only at the trench-parallel profile, but also along the trench-perpendicular refraction profiles, would enable the comprehensive identification of the subduction channel. Consequently the erosional mechanisms beneath the continental slope, related to the subduction channel thickness, can be further specified with the two-dimensional wave-field modeling method.

Correlation of the dip angle of the subducting slab from this study with earthquake observations, reveals a steep subduction angle close to the trench, which flattens to the typical flat subduction at about 50 km depth, and ~200 km distance from the trench axis. Here, the extent where flat subduction occurs, is the largest area worldwide in the wake of ridge subduction. The frontal prism and the backstop structure are well-defined by their seismic P-wave velocities. The backstop type, which is similar across the entire Peruvian margin, indicates the same mechanical behavior along the margin wedge. Hence, the different pronounced outer highs (the most distinct at the middle profile SO146-5/12°S) developed at the toe of the backstop suggest varying material properties within the margin wedge.

Subduction processes along the Peruvian margin are dominated by tectonic erosion, as

---

suggested from the thin sediment fill in the trench, the large taper and the small size of the frontal prism. Tectonic erosion is indicated by the low seismic velocities within the frontal prism, the high convergence rate, the irregular surface slope, the presence of extensional forearc basins, the rough topography of the subducting plate, and the retreat of the volcanic front from the Mesozoic to the late Cenozoic magmatic arc [*McKee and Noble, 1990*]. These results comply with the tectonic history of the Peruvian margin. The northern part of the research area at 9°S has subsided more than 1000 m during the last 12–13 Ma. In contrast, the region at 12°S has undergone a phase of uplift and enhanced tectonic erosion during 11–7 Ma with subsequent subsidence of more than several hundred meters since 6 my [*von Huene and Suess, 1988; von Huene and Lallemand, 1990; Clift et al., 2003*]. Erosion rates derived from subsidence reconstruction for the Lima Basin at 12°S show a rate 10 times higher during and shortly after the passage of the Nazca Ridge than before [*Clift et al., 2003*].

However, frontal tectonic erosion is not the only subduction mechanism across the Peruvian forearc. Basal erosion is most effective where the dip of the subducting plate increases. Basal erosion, as observed here, and related extension lead to the steepening of the trench slope causing slope failure. The failed sediments are transported due to gravitational forces and form the small frontal prism at the toe of the margin. The frontal prisms, missing where Nazca Ridge currently subducts [*Hampel et al. [2004]*], and established at the lower slopes 6 my and 11 my after Nazca Ridge passage, display different evolutionary stages following ridge crest subduction, which is marked by increased erosion. The width of the frontal prism increases from 12 km to 15 km, between the profiles from south to north (SO146-3/14°S and SO146-5/12°S). These 'time slices' indicate, that 11 my after collision, the margin has returned to equilibrium.

---

## Bibliography

- Adam, J. and Reuther, C.-D., Crustal dynamics and active fault mechanics during subduction erosion. Application of frictional wedge analysis on to the North Chilean Forearc, *Tectonophysics*, 321, 297-325, 2000.
- Ballance, P.F., Scholl, D.W., Vallier, T.L., Stevenson, A.J., Ryan, H.F., and Herzer, R.H., Subduction of a Late Cretaceous seamount of the Louisville Ridge at the Tonga Trench: A model of normal and accelerated tectonic erosion, *Tectonics*, 8, 5, 953-962, 1989.
- Barazangi, M. and Isacks, B., Spatial distribution of earthquakes and subduction of the Nazca Plate beneath South America, *Geology*, 4, 686-692, 1976.
- Barckhausen, U., Ranero, C.R., von Huene, R., Cande, S.C., and Roeser, H.A., Revised tectonic boundaries in the Cocos Plate off Costa Rica: Implications for the segmentation of the convergent margin and for the plate tectonic models, *Journal of Geophysical Research*, 106, B9, 207-220, 2001.
- Barth, M.G., McDonough, W.F., and Rudnick, R.L., Tracking the budget of Nb and Ta in the continental crust, *Chemical Geology*, 165, 3-4, 197-213, 2000.
- Bebout, G.E., Scholl, D.W., Kirby, S.H., and Platt, P., (eds.) Subduction: Top to Bottom, *Geophysical Monograph Ser.*, 96, AGU, 1996.
- Behrmann, J.H. and Kopf, A., Balance of tectonically accreted and subducted sediment at the Chile Triple Junction, *Geologische Rundschau*, 90 753-768, 2001.
- Byerlee, J.D., Friction of rocks, *Pure Applied Geophysics*, 92, 3681-3682, 1978.
- Byrne, D.E., Wang, W.-H., and Davis, D.M., Mechanical role of backstops in the growth of forearcs, *Tectonics*, 12, 1, 123-144, 1993.
- Bialas, J. and Flueh, E.R., Ocean Bottom Seismometers, *Sea Technology*, 40, 4, 41-46, 1999.
- Bialas, J. and Kukowski, N. (eds.) with contributions of cruise participants, FS Sonne Cruise Report SO146 1&2 GEOPECO: Geophysical experiments at the Peruvian Continental Margin, investigations of tectonics, mechanics, gashydrates and fluid transport *Cruise Report*, GEOMAR, Kiel, 2000.

## BIBLIOGRAPHY

---

- Brekovskikh, L.M., Waves in layered media, *New York*, 1960.
- Brown, K., and Westbrook, G.K., Mud diapirism and subcretion in the Barbados Ridge accretionary complex: The role of fluids in accretionary processes, *Tectonics*, *7*, *3*, 613-640, 1988.
- Byrne, D.E., Davis, D.M., and Sykes, L.R., Loci and maximum size of thrust earthquakes and the mechanics of the shallow region of subduction zones, *Tectonics*, *7*, 833-857, 1988.
- Byrne, D.E., Wang, W-H., and Davis, D.M., Mechanical role of backstops in the growth of forearcs, *Tectonics*, *12*, *1*, 123-144, 1993.
- Cande, S.C. and Leslie, R.B., Late Cenozoic tectonics of the southern Chile Trench, *Journal of Geophysical Research*, *91*, *1*, 471-496, 1986.
- Cande, S.C. LaBreque, J.L., Larson, R.L., and Pitman, W.C., Magnetic lineations of the world's ocean basins, *Map with text*, AAPG, *Tulsa, Okl.*, 1989.
- Carlson, R.L., Seismic velocities in the uppermost oceanic crust: Age dependence and the fate of layer 2A, *Journal of Geophysical Research*, *103*, *4*, 7069-7077, 1998.
- Chapple, W.M., Mechanics of thin-skinned fold-and-thrust belts, *Geological Society American Bulletin*, *89*, 1189-1198, 1978.
- Christensen, N.I. and Salisbury, M.H., Structure and composition of the lower oceanic crust, *Review of Geophysics*, *13*, 57-86, 1975.
- Christeson, G.L., McIntosh, K.D., and Shipley, T.H., Seismic attenuation in the Costa Rica margin wedge: Amplitude modeling of ocean bottom hydrophone data, *Earth and Planetary Science Letters*, *179*, 391-405, 2000.
- Clift, P.D., Pecher, I., Kukowski, N., and Hampel, A., Tectonic erosion of the Peruvian forearc, Lima Basin, by subduction and Nazca Ridge collision, *Tectonics*, *22*, *3*, 1023, doi:10.1029/2002TC001386, 2003.
- Clift, P.D. and Vannucchi, P., Controls on tectonic accretion versus erosion in subduction zones: Implications for the origin and recycling of the continental crust, *Review of Geophysics*, *42*, RG2001, doi:10.1029/2003RG000127, 2004.
- Cohen, J.K. and Stockwell, J.J.W., CWP/SU: Seismic Unix Release 35: a free package for seismic research and processing, *Center for Wave Phenomena, Colorado School of Mines*, 2001.
- Collot, J.Y. and Davy, B., Forearc structures and tectonic regimes at the oblique subduction zone between the Hikurangi Plateau and the southern Kermadec margin, *Journal of Geophysical Research*, *103*, *1*, 623-650, 1998.



- Collot, J.Y., Charvis, P., Gutscher, M.-A., and Operto, S., Exploring the Ecuador-Colombia Active Margin and Interplate Seismogenic Zone, *EOS Transactions, AGU*, 83, 17, 185-190, 2002.
- Dahlen, F.A., Suppe, J., and Davis, D., Mechanics of Fold-and-Thrust Belts and Accretionary Wedges: Cohesive Coulomb Theory, *Journal of Geophysical Research*, 89, B12, 10125-10133, 1984.
- Dahlen, F.A., Critical taper model of fold-and-thrust belts and accretionary wedges, *Earth and Planetary Science Letters, Annual Review*, 18, 55-99, 1990.
- Davis, D., Suppe, J., and Dahlen, F.A., Mechanics of Fold-and-Thrust Belts and Accretionary Wedges, *Journal of Geophysical Research*, 88, B2, 1153-1172, 1983.
- Davis, D.M. and von Huene, R., Inferences on sediment strength and fault friction from structures at the Aleutian Trench, *Geology*, 15, 517-522, 1987.
- Davis, D.M., Accretionary Mechanics with Properties that Vary in Space and Time, *in*, Bebout, G.E., Scholl, D.W., Kirby, S.H., and Platt, J.P., (eds.), *Subduction: Top to Bottom, Geophysical Monograph Ser.*, 96, 39-48, 1996.
- Dewey, J.F. and Windley, B.F., Growth and differentiation of the continental crust, *Philos. Trans. R. Soc. London, Ser. A*, 301, 189-206, 1981.
- Dupont, J. and Herzer, R.H., Effect of subduction of the Louisville Ridge on the structure and morphology of the Tonga Arc, *in* Scholl, D.W. and Vallier, T.L., (eds.), *Geology and Offshore Resources of Pacific Island Arcs - Tonga Region, Earth Sci. Ser.*, 2, 323-332, 1985.
- Elliott, D., The motion of thrust sheets, *Journal of Geophysical Research*, 81, 949-963, 1976.
- Ewing, w.M., Jardetsky, W.S., and Press, F., Elastic waves in layered media, *Mc-Graw-Hill*, 1957.
- Flueh, E.R. and Bialas, J., A digital, high data capacity ocean bottom recorder for seismic investigations, *Int. Underwater Systems Design*, 18, 3, 18-20, 1996.
- Fruehn, J., von Huene, R., and Fisher, M.A., Accretion in the wake of terrane collision: The Neogene accretionary wedge off Kenai Peninsula, Alaska, *Tectonics*, 18, 2, 263-277, 1999.
- Fuchs, K. and Müller, G., Computation of synthetic seismograms with the reflectivity method and comparison with observations, *Geophys. J. R. Astron. Soc.*, 23, 417-433, 1971.
- Goslin, J., Bauzart, P., Francheteau, J., and Le Pichon, X., Thickening of the oceanic layer in the Pacific Ocean, *Marine Geophysical Research*, 1, 418-427, 1972.

## BIBLIOGRAPHY

---

- Grevenmeyer, I., Kaul, N., and Villinger, H., Hydrothermal activity and the evolution of the seismic properties of upper oceanic crust, *Journal of Geophysical Research*, *104*, B3, 5069-5079, 1999.
- Gudmundsson, O. and Sambridge, M., A regionalized upper mantle (RUM) seismic model, *Journal of Geophysical Research*, *103*, B4, 7121-7136, 1998.
- Gutscher, M.-A., Spakman, W., Bijwaard, H., and Engdahl, E.R., Geodynamics of flat subduction: Seismicity and tomographic constraints from the Andean margin, *Tectonics*, *19*, 5, 814-833, 2000.
- Hamilton, W.B., Subduction systems and magmatism, in Smellie, J.L., (edt.), *Volcanism Associated with Extension at Consuming Plate Margins*, *Geological Society Special Publication*, *81*, 3-28, 1995.
- Hampel, A., The migration history of the Nazca Ridge along the Peruvian active margin: a re-evaluation, *Earth and Planetary Science Letters*, *203*, 665-679, 2002.
- Hampel, A., Kukowski, N., Bialas, J., Huebscher, C., and Heinbockel, R., Ridge subduction at an erosive margin: The collision zone of the Nazca Ridge in southern Peru, *Journal of Geophysical Research*, *109*, 2, doi:10.1029/2003JB002593, 2004.
- Hasegawa, A. and Sacks, I.S., Subduction of the Nazca Plate beneath Peru as determined from seismic observations, *Journal of Geophysical Research*, *86*, 4971-4980, 1981.
- Hayward, N., Westbrook, G.K., and Peacock, S., Seismic velocity, anisotropy, and fluid pressure in the Barbados accretionary wedge from an offset vertical seismic profile with seabed sources, *Journal of Geophysical Research*, *108*, 11, 2515, doi:10.1029/2001JB001638, 2003.
- Hearn, T.M. and Ni, J.F., Pn velocities beneath continental collision zones: The Turkish-Iranian Plateau, *Geophysical Journal International*, *117*, 273-283, 1994.
- Heinbockel, R., Dehghani, G.A., and Huebscher, Ch., Gravity and Magnetic Investigations Along the Peruvian Continental Margin, *Geophysical Research Abstracts*, *5*, 05857, 2003.
- Helwig, J. and Hall, G., Steady-state trenches?, *Geology*, *2*, 309-316, 1974.
- Hey, R.N., Johnson, P.D., Martinez, F., Korenaga, J., Somers, M.L., Huggett, Q.J., LeBas, T.P., Rusby, R.I., and Naar, D.F., Plate boundary reorganization at a large-offset, rapidly propagating rift, *Nature*, *378*, 9, 167-170, 1995.
- Hilde, T.W.C. and Warsi, W.E.K., Subduction induced Rifting of the Nazca Plate along Mendaña Fracture Zone, *EOS Transactions, AGU*, *63*, 444, 1982.

- Hole, J.A. and Zelt, B.C., Three-dimensional finite-difference reflection travel times, *Geophysical Journal International*, 121, 427-434, 1995.
- Hoshino, K., Koide, H., Inami, K., Iwamura, S., and Mitsui, S., Mechanical properties in Japanese Tertiary sedimentary rocks, *Geological Survey Japan, Kawasaki*, 200 pp., 1972.
- Huaco, D., editor, Catálogo Sísmico del Perú, 1500-1982 *Instituto Geofísico del Perú, Lima*, 1986.
- Huaco, D., editor, Catálogo Sísmico del Perú, versión actualizada *Instituto Geofísico del Perú, Lima*, 1999.
- Hübscher, C. and Kukowski, N., Complex BSR Pattern in the Yaquina Basin off Peru: Implications for Impact of Anisotropic Permeability and Tectonic, *Geo-Marine Letters*, 23, 2, 91-101, doi:10.1007/s00367-003-0128-z, 2003.
- Huchon, P. and Bourgois, J., Subduction-Induced Fragmentation of the Nazca Plate off Peru: Mendana Fracture Zone and Trujillo Trough Revisited, *Journal of Geophysical Research*, 95, 6, 8419-8436, 1990.
- von Huene, R. and Suess, E., Ocean Drilling Program Leg 112, Peru continental margin: Part 1, Tectonic history, *Geology*, 16, 934-938, 1988.
- von Huene, R. and Lallemand, S., Tectonic erosion along the Japan and Peru convergent margins, *Geological Society of America Bulletin*, 102, 704-720, 1990.
- von Huene, R. and Scholl, D.W., Observations at convergent margins concerning sediment subduction, subduction erosion, and the growth of continental crust, *Reviews of Geophysics*, 29, 3, 279-316, 1991.
- von Huene, R. and Scholl, D.W., The return of sialic material to the mantle indicated by terrigenous material subducted at convergent margins, *Tectonophysics*, 219, 163-175, 1993.
- von Huene, R., Pecher, I.A., and Gutscher, M.-A., Development of the accretionary prism along Peru and material flux after subduction of Nazca Ridge, *Tectonics*, 15, 1, 19-33, 1996.
- von Huene, R. and Ranero, C.R., Subduction erosion and basal friction along the sediment-starved convergent margin off Antofagasta, Chile, *Journal of Geophysical Research*, 108, doi:10.1029/2001JB001569, 2003.
- Hussong, D.M., Dang, S.P., Kulm, L.D., and Couch, R.W., in Hilde, T.W.C. et al., (eds.), Jean Charcot Sea Beam survey along ODP leg 112 northern transect, in, *Reg. Atlas Ser, Atlas 9, 19 sheets, Ocean Margin Drilling Program, Marine Science International, Woods Hole, Mass.*, 1984.

## BIBLIOGRAPHY

---

- Hyndman, R.D., Yorath, C.D., Clowes, R.M., and Davis, E.E., The northern Cascadia subduction zone at Vancouver Island, Seismic structure and tectonic history, *Canadian Journal of Earth Sciences*, *27*, 3, 313-329, 1990.
- Ito, G., McNutt, M., and Gibson, R., Crustal structure of the Tuamotu Plateau, 15°S, and implications for its origin, *Journal of Geophysical Research*, *100*, 5, 8097-8114, 1995.
- Kallweit, R.S. and Wood, L.C., The limits of resolution of zero-phase wavelets *Geophysics*, *47*, 1035-1046, 1982.
- Kikuchi, M. and Yamanaka, Y., Earthquake Information Center Seismological note no. 105, *Earthquake Information Center, Earthquake Research Institute, University of Tokyo*, 2001.
- Kind, R., The reflectivity method for a buried source, *Journal of Geophysics*, *44*, 603-612, 1978.
- Kopp, C., Fruehn, J., Flueh, E.R., Reichert, C., Kukowski, N., Bialas, J., and Klaeschen, D., Structure of the Makran subduction zone from wide-angle and reflection seismic data, *Tectonophysics*, *329*, 171-191, 2000.
- Kopp, H., Flueh, E.R., Klaeschen, D., Bialas, J., and Reichert, C., Crustal structure of the central Sunda margin at the onset of oblique subduction, *Geophysical Journal International*, *147*, 449-474, 2001.
- Kopp, H. and Kukowski, N., Backstop geometry and accretionary mechanics of the Sunda margin, *Tectonics*, *22*, 6, doi:10.1029/2002TC001420, 2003.
- Kopp, H., Flueh, E.R., C. Papenberg, and Klaeschen, D., Seismic investigations of the O'Higgins Seamount Group and Juan Fernández Ridge: Aseismic ridge emplacement and lithosphere hydration, *Tectonics*, *23*, doi:10.1029/2003TC001590, 2004.
- Krabbenhöft, A., Bialas, J., Kopp, H., Kukowski, N., and Hübscher, C., Crustal structure of the Peruvian continental margin from wide-angle seismic studies, *Geophysical Journal International*, *159*, 749-764, doi:10.1111/j.1365-246X.2004.02425.x, 2004.
- Kukowski, N., von Huene, R., Malavieille, J., and Lallemand, S.E., Sediment accretion against a buttress beneath the Peruvian continental margin at 12°S as simulated with sandbox modeling, *Geologische Rundschau*, *83*, 822-831, 1994.
- Kukowski, N., Hampel, A., Bialas, J., Broser, A., Huebscher, C., Barckhausen, U., and Bourgois, J., Long-term and short-term tectonic erosion at the Peruvian active margin between 9°S and 15°S: evidence from bathymetry data and 3D sandbox analogue modeling, *5th International Symposium of the Andean Geodynamics, Toulouse, France*, 2002.

- Kulm, L.D., Prince, R.A., French, W., Johnson, S., and Masias, A., Crustal structure and tectonics of the central Peru continental margin and trench, *Geological Society of America, Memoir 154*, 445-468, 1981.
- Lallemand, S.E., Schnürle, P., and Malavieille, J., Coulomb theory applied to accretionary and nonaccretionary wedges: Possible causes for tectonic erosion and/or frontal accretion, *Journal of Geophysical Research*, *99*, 6, 12033-12055, 1994.
- Lallemand, S.E., High rates of arc consumption by subduction processes: Some consequences, *Geology*, *23*, 551-554, 1995.
- Lallemand, S.E., Possible interaction between mantle dynamics and high rates of arc consumption by subduction processes in Circum-Pacific area, in Flower, M.F.J. et al., (edts.), *Mantle Dynamics and Plate Interactions in East Asia, Geodynamic Series, AGU, Washington, D.C.*, *27*, 1-9, 1994.
- Laursen, J., Scholl, D.W., and von Huene, R., Neotectonic deformation of the central Chile margin: Deepwater forearc basin formation in response to hot spot ridge and seamount subduction, *Tectonics*, *21*, 5, 1038, doi:10.1029/2001TC901023, 2002.
- Lehner, F.K., Comments on 'Non-cohesive critical Coulomb wedges: an exact solution' by F.A. Dahlen, *Journal of Geophysical Research*, *91*, 783-796, 1986.
- Le Pichon, X., Houtz, R.E., Drake, C.L., and Nafe, E., Crustal structure of the mid-ocean ridges, 1, Seismic refraction measurements, *Journal of Geophysical Research*, *70*, 319-340, 1965.
- Lonsdale, P. and Klitgord, K.D., Structure and tectonic history of the eastern Panama Basin, *Geol. Soc. Am. Bull.*, *89*, 981-999, 1978.
- Luetgert, J., MacRay-Interactive two-dimensional seismic raytracing for the Macintosh, *U.S. Geological Survey Open File Report*, 92-356, 1992.
- McKee, E.H. and Noble, D.C., Cenozoic tectonic events, magmatic pulses, and base-and precious metal mineralization in the central Andes, in Ericksen, G.E., Pinochet, M.-T.C, and Reinemund, J.A., (edts.), *Geology of the Andes and Its Relation to Hydrocarbon and Mineral Resources, Earth Sci. Ser.*, *11*, 189-194, 1990.
- Moore, G.F., Curray, J.R., and Emmel, F.J., Sedimentation in the Sunda Trench and forearc region, in, Leggett, J.K., (edt.), *Geological Society Special Publication*, *10*, London, 245-258, 1982.
- Moore, G.F. and Taylor, B., Structure of the Peru forearc from multichannel seismic reflection data, in, Suess, E., von Huene, R., et al., (edts.), *Proc. ODP, Init. Repts.*, *112*, College Station, TX, 71-76, 1988.

## BIBLIOGRAPHY

---

- Müller, G., Theoretical Seismograms for some Types of Point-sources in Layered Media, Part I: Theory, *Zeitschrift für Geophysik*, 15-35, 1968.
- Müller, G., The reflectivity method: A tutorial, *Journal of Geophysics*, 58, 153-173, 1985.
- Müller, R.D., Roest, W.R., Royer, J.-Y., Gahagan, L.M., and Sclater, J.G., Digital Isochrons of the world's Ocean Floor, *Journal of Geophysical Research*, 102, 3211-3214, 1997.
- Norabuena, E.O., Snoke, J.A., and James, D.E., Structure of the subducting Nazca Plate beneath Peru, *Journal of Geophysical Research*, 99, 5, 9215-9226, 1994.
- Norabuena, E.O., Dixon, T.H., Stein, S., and Harrison, C.G.A., Decelerating Nazca-South America and Nazca-Pacific Plate Motions, *Geophysical Research Letters*, 26, 22, 3405-3408, 1999.
- Nur, A. and Ben-Avraham, Z., Volcanic gaps and the consumption of aseismic ridges in South America, *Geological Society of America, Memoir 154*, 445-468, 1981.
- Pacheco, J.F. and Sykes, L.R., Seismic moment catalog of large shallow earthquakes, 1900 to 1989, *Bull. Seismological Society of America*, 82, 1306-1349, 1992.
- Parsons, B. and Sclater, J.G., An analysis of the variation of ocean floor bathymetry and heat flow with age, *Journal of Geophysical Research*, 82, 5, 803-827, 1977.
- Paterson, M.S., Experimental Rock Deformation: The Brittle Field, *Springer Verlag, New York*, 16-50, 1978.
- Pecher, I.A., Minshull, T.A., Singh, S.C., and von Huene, R., Velocity structure of a bottom simulating reflector offshore Peru: Results from full waveform inversion, *Earth and Planetary Science Letters*, 139, 459-469, 1996.
- Pecher, I.A., Kukowski, N., Hübscher, C., Greinert, J., and Bialas, J., The link between bottom-simulating reflections and methane flux into the gas hydrate stability zone; new evidence from Lima Basin, Peru margin, *Earth and Planetary Science Letters*, 185, 343-354, 2001.
- Pilger, R.H., Jr. and Handschumacher, D.W., The fixed-hotspot hypothesis and origin of the Easter-Sala y Gomez-Nazca trace, *Geological Society of America Bulletin, Part I*, 92, 437-446, 1981.
- Pilger, R.H., Jr., Plate reconstructions, aseismic ridges, and low-angle subduction beneath the Andes, *Geological Society of America Bulletin, Part I*, 92, 448-456, 1981.
- Platt, J.P., Dynamics of orogenic wedges and the uplift of high-pressure metamorphic rocks, *Geological Society of America Bulletin*, 97, 1037-1053, 1986.

- Press, F., and Siever, R., Einführung in das System Erde, aus dem Amerikan. übersetzt und hrsg. von Volker Schweizer, *Spektrum, Akadem. Verlag, Heidelberg*, 2003.
- Protti, M., Güendel, F., and McNally, K., Correlation between the age of the subducting Cocos Plate and the geometry of the Wadati-Benioff zone under Nicaragua and Costa Rica, in Mann, P., (edt.), *Geologic and tectonic development of the Caribbean Plate boundary in southern Central America, GSA Special Paper, 295*, 309-326, 1995.
- Pubellier, M., Bader, A.G., Rangin, C., Deffontaines, B., and Quebral, R., Upper plate deformation induced by subduction of a volcanic arc: The Snellius Plateau (Molucca Sea, Indonesia and Mindanao, Phillipines), *Tectonophysics, 304*, 345-368, 1999.
- Purdy, G.M., Kong, L.S.L., Christeson, G.L., and Solomon, S.C., Relationship between spreading rate and seismic structure of mid-ocean ridges, *Nature, 355*, 815-817, 1992.
- Ranero, C.R. and von Huene, R., Subduction erosion along the Middle America convergent margin, *Nature, 404*, 748-752, 2000.
- Rudnick, R.L. and Fountain, D., Nature and composition of the continental crust: A lower crustal perspective, *Review of Geophysics, 33*, 267-310, 1995.
- Rüpke, L.H., Phipps Morgan, J., Hort, M., and Connolly, J.A.D., Serpentine and the subduction zone water cycle, *Earth and Planetary Science Letters, 223*, 17-34, doi:10.1016/j.epsl.2004.04.018, 2004.
- Ruff, L.J., Large Earthquakes in Subduction Zones: Segment Interaction and Recurrence Times, in, Bebout, G.E., Scholl, D.W., Kirby, S.H., and Platt, J.P., (edts.), *Subduction: Top to Bottom, Geophysical Monograph Ser., 96*, 91-104, 1996.
- Sandmeier, K.-J. and Wenzel, F., Synthetic seismograms for a complex crustal model, *Geophysical Research Letters, 13, 1*, 22-25, 1986.
- Sandwell, D.T. and Smith, W.H.F., Marine gravity anomaly from Geosat and ERS1 satellite altimetry, *Journal of Geophysical Research, 102*, 10039-10054, 1997.
- Savage, J.C., A dislocation model of strain accumulation and release at a subduction zone, *Journal of Geophysical Research, 88*, 4984, 1983.
- Schlüter, H.U., Gaedicke, C., Roeser, H.A., Schreckenberger, B., Meyer, H., Reichert, C., Djajadihardja, Y., and Prexl, A., Tectonic features of the southern Sumatra - western Java forearc of Indonesia, *Tectonics, 21, 5*, 1047, doi:10.1029/2001TC901048, 2002.
- Scholz, C.H., The mechanics of earthquakes and faulting, *Cambridge University Press*, 1990.
- Sheriff, R.E. and Geldart, L.P., Exploration Seismology, *Cambridge University Press, 2nd ed.*, 1995.

## BIBLIOGRAPHY

---

- Steinmann, G., Geologie von Peru, *Carl Winters Universitätsbuchhandlung, Heidelberg*, pp312, 1985.
- Tavera, H. and Buforn, E., Sismicidad y Sismotectónica de Perú, in Udias, A. and Buforn, E, eds., *Sismicidad y Sismotectónica de Centro y Sur América, Revista Física de la Tierra, Universidad Complutense de Madrid*, 10 187-219, 1998.
- Taylor, S.R. and McLennan, S.M., The continental Crust: Its Composition and Evolution: An Examination of the Geochemical Record preserved in Sedimentary Rocks, *Blackwell Sci., Malden, Mass.*, pp312, 1985.
- Vannucchi, P., Scholl, D.W., Meschede, M., and McDougall, K., Tectonic erosion and consequent collapse of the Pacific margin of Costa Rica: Combined implications from ODP Leg 170, seismic offshore data, and regional geology of the Nicoya Peninsula, *Tectonics*, 20, 5, 649-668, 2001.
- Vannucchi, P., Ranero, C.R., Galeotti, S., Straub, S.M., Scholl, D.W., and McDougall-Ried, K., Fast rates of subduction erosion along the Costa Rica Pacific margin: Implications for nonsteady rates of crustal recycling at subduction zones, *Journal of Geophysical Research*, 108, 2511, doi:10.1029/2002JB002207, 2003.
- Vidale, J.E., Finite-difference calculation of travel times, *Bulletin of the Seismological Society of America*, 78, 2062-2076, 1988.
- Vidale, J.E., Finite-difference calculation of travel times in three dimensions, *Geophysics*, 55, 521-526, 1990.
- Vogt, P.R., Lowrie, A., Bracey, D.R., and Hey, R.N., Subduction of aseismic oceanic ridges: Effects on shape, seismicity and other characteristics of consuming plate boundaries, *Geological Society of America Special Paper*, 172, 59, 1976.
- Walther, C.H.E., The crustal structure of the Cocos ridge off Costa Rica, *Journal of Geophysical Research*, 101, 5, 2136, doi:10.1029/2001JB000888, 2003.
- Wang, W-H. and Davis, D.M., Sandbox model simulation of forearc evolution and noncritical wedges, *Journal of Geophysical Research*, 108, B3, 11329-11339, 1996.
- Wessel, P. and Smith, W.H.F., Free software helps map and display data, *EOS Transactions, AGU*, 72, 441, 445-446, 1991.
- White, R.S., Mc Kenzie, D., and O’Nions, K.R., Oceanic crustal thickness from seismic measurements and rare earth element inversions, *Journal of Geophysical Research*, 97, 13, 683-715, 1992.
- Whitmarsh, R.B., Seismic refraction studies of the upper igneous crust in the North Atlantic and porosity estimates for Layer 2, *Earth and Planetary Science Letters*, 37, 451-464, 1978.



- Woodhouse, J.H., Efficient and stable methods for performing seismic calculations in stratified media, *in* Dziewonski, A. and Boschi, E., (eds.) *Proceedings of Enrico Fermi International School of Physics, Amsterdam*, 127-151, 1980.
- Zelt, C.A. and Barton, P.J., Three dimensional seismic refraction tomography: A comparison of two methods applied to data from the Faeroe Basin, *Journal of Geophysical Research*, 103, 4, 7187-7210, 1998.
- Zelt, C.A., Modelling strategies and model assessment for wide-angle seismic travelttime data, *Geophysical Journal International*, 139, 183-204, 1999.



# A

---

## The Coulomb Theory

The stability of a convergent margin wedge can be calculated, using the Coulomb theory. Several sandbox modeling experiments and numerical modeling studies have been accomplished to obtain additional insight on the critical taper [e.g., *Davis et al., 1983*; *Kukowski et al., 1994*; *Byrne et al., 1993*]. The following equations show the relationship of the parameters illustrated in Figures 4.11 and A.1, which are sufficient to determine the exact critical taper and the slip lines orientation in every part of the stability field diagram as a function of the surface slope  $\alpha$  and the dip angle of the subducting plate  $\beta$  [*Dahlen et al., 1984*].

$$\alpha + \beta = \Psi_b - \Psi_0 \quad (\text{A.1})$$

with

$$\Psi_0 = \frac{1}{2} \arcsin\left(\frac{\sin\alpha^*}{\sin\phi}\right) - \frac{1}{2}\alpha^* \quad (\text{A.2})$$

and

$$\Psi_b = \frac{1}{2} \arcsin\left(\frac{\sin\phi_b^*}{\sin\phi}\right) - \frac{1}{2}\phi_b^* \quad (\text{A.3})$$

with the effective angle of basal friction

$$\phi_b^* = \arctan\left\{\mu_b\left(\frac{1-\lambda_b}{1-\lambda}\right)\right\} \quad (\text{A.4})$$

and the 'modified' slope angle

$$\alpha^* = \arctan\left\{\left(\frac{1-\rho_w/\rho}{1-\lambda}\right)\tan\alpha\right\} \quad (\text{A.5})$$

In a homogeneous non-cohesive wedge, the failure surfaces are orientated at  $\pm\frac{1}{2}(90^\circ - \phi)$ . They have the same dip everywhere within the wedge with respect to the maximum-compressive-stress ( $\sigma_1$ ) axis. The angle between a forward verging thrust and the subducting plate is given by:

$$\delta_b = \frac{1}{2}(90^\circ - \phi) - \Psi_b \quad (\text{A.6})$$

The steeper angle of the conjugate backthrust is given by:

$$\delta'_b = \frac{1}{2}(90^\circ - \phi) + \Psi_b \quad (\text{A.7})$$

The failure stress  $|\tau|$  on both forward and conjugate backthrust at the point where they step up into the wedge is given by:

$$|\tau| = (\rho - \rho_w)gz \sin\alpha \left(\frac{\cos\phi}{\sin 2\Psi_0}\right) \quad (\text{A.8})$$

The frictional resistance on the basal décollement at the same point is given by:

$$\tau_b = (\rho - \rho_w)gz \sin\alpha \left( \frac{\cos 2\Psi_b}{\sin 2\Psi_0} \right) \quad (\text{A.9})$$

*Lehner* [1986] has shown, how the various multiple solutions can be obtained by a graphical construction method in the Mohr diagram, which is illustrated in Figure A.1. The angles of the internal and basal friction  $\phi$  and  $\phi_b$  are related to the internal wedge strength and the basal friction (décollement strength). The angles  $\Psi$  and  $\Psi_b$  are the angles between the greatest compressive stress  $\sigma_1$  and the top, and the base of the wedge, respectively. The basal shear traction  $\tau_b$  is given by the intersection of the frictional failure law  $|\tau| = \mu_b \sigma_n^*$  with the Mohr stress circle corresponding to the basal depth H.

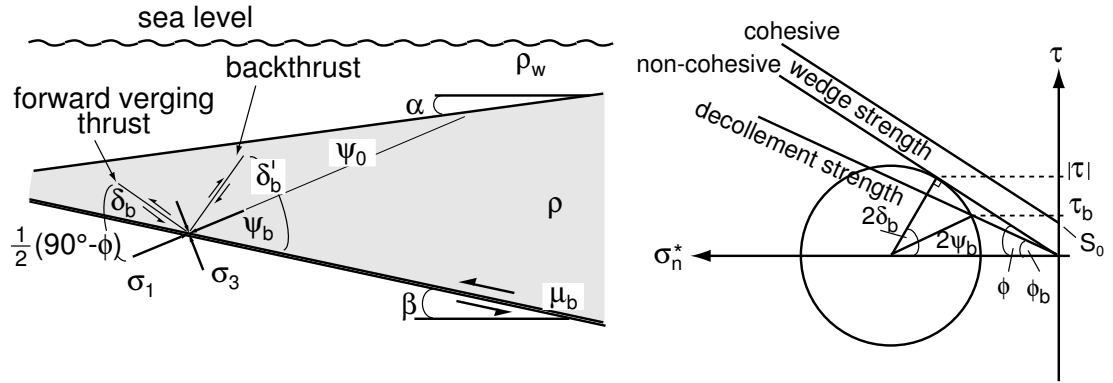


Figure A.1: *Geometry of conjugate thrust fault orientation within a non-cohesive Coulomb wedge (left). The forward verging thrusts form at low angles, in contrast to the steeper backthrusts. Mohr diagram (modified after Davis et al. [1983]) illustrating the state of stress at some point within the wedge (right: wedge strength with and without cohesion  $S$ ) and at the base of the wedge.*

# B

---

## The Reflectivity Method

Theoretical seismograms can be numerically calculated with the Reflectivity Method [Fuchs and Müller, 1971]. The derivation and description of the method in terms of equations, e.g., the calculation of reflection and transmission coefficients at an interface, is described in detail in the tutorial by Müller [1985].

The synthetic seismogram is calculated for a layered medium consisting of homogeneous layers. Strong vertical gradients should be divided into several homogeneous layers since the wavefield is computed for 1st order discontinuities. The wavefield is computed using the Fuchs-Müller-signal [Müller, 1968]. The source-time signal  $J(t)$  is given by the following equation:

$$J(t) = \frac{1}{\delta} \left\{ 1 - \cos(\delta t) + \frac{1}{m^2} (\cos(m\delta t) - 1) \right\} \quad \text{for } 0 \leq t \leq T \quad (\text{B.1})$$

with:  $t = \text{time}$ ,  $N = 1, 2, 3, \dots$ ,  $m = \frac{N+2}{N}$ ,  $\delta = \frac{N\pi}{T}$ .

The far-field signal for an explosion source, is given by the derivation of the the time-source signal,  $J(t)$ , of equation B.1:

$$\frac{dJ}{dt} = \sin(\delta t) - \frac{\delta}{m} (\sin(m\delta t)) \quad (\text{B.2})$$

Variables  $t$ ,  $\delta$ , and  $m$  are explained in equation B.1.

The complete medium response is obtained by this method. Also partial medium responses can be calculated, such as multiples and conversions at interfaces, transmission losses at interfaces, energy loss due to attenuation within the layers. The option of the Reflectivity Method to compute the partial medium response makes it more flexible compared to other methods, which give the complete response of the medium [e.g., Kind, 1978; Woodhouse, 1980].



## Acknowledgements

I am very grateful to Prof. Dr. Ernst Flueh for his continuous support and advice during the last few years.

Many thanks to the participants of RV 'Sonne' Cruise 146-1 & 2, scientists and crew, for the acquisition and pre-processing of the data.

The continuous support and advice of Dr. Jörg Bialas is warmly acknowledged.

I thank Prof. Dr. Wolfgang Rabbel for spontaneously agreeing to act as co-referee.

Many thanks to Heidrun Kopp and Cord Papenberg for their advice during modeling and helpful discussions.

I would like to thank my entire family for their support during the last few years, especially my husband, Meiko, for his patience with me during the last weeks.

Special thanks to all members of the Geodynamics Department for their friendly assistance and the kind atmosphere within the department.





## **Erklärung**

Hiermit erkläre ich, daß die von mir für das Promotionsverfahren vorgelegte Abhandlung 'Crustal Structure of the Peruvian Continental Margin: Results from Wide-Angle Seismic Studies', abgesehen von der Beratung der Betreuer nach Inhalt und Form, meine eigene Arbeit ist. Bisher ist die Arbeit noch nicht an anderer Stelle im Rahmen eines Prüfungsverfahrens vorgelegt worden.

Anne Krabbenhöft.



# Curriculum Vitae

## Personal details:

Name: Anne Krabbenhöft  
Date of Birth: 13.02.1973  
Place of Birth: Hermannstadt  
Citizenship: German  
Family Status: Married

Address: Spitzenkamp 22  
24149 Kiel

Email: akrabbenhoeft@ifm-geomar.de

## Doctorate:

Since January 2001      PhD student at IFM-GEOMAR, Kiel

## Education:

October 2000: German Diplom (equivalent MSc) in Geophysics  
1997 – 2000: Studies in Geophysics at the University of Kiel  
1993 – 1997: Studies in Physical Oceanography at the University of Kiel  
1992 – 1993: Au Pair in New York, U.S.A.  
1992: Abitur  
1983 – 1992: Albertus-Magnus-Schule (Gymnasium), Viernheim